Top quark search with the D0 1992–1993 data sample

S. Abachi,[12] B. Abbott,[33] M. Abolins,[23] B.S. Acharya,[40] I. Adam,[10] D.L. Adams,[34] M. Adams,[15] S. Ahn,[12] H. Aihara,[20] J. Alitti,[36] G. Álvarez,[16] G.A. Alves,[8] E. Amidi,[27] N. Amos,[22] E.W. Anderson,[17] S.H. Aronson,[3] R. Astur,[38] R.E. Avery,[29] A. Baden,[21] V. Balamurali,[30] J. Balderston,[14] B. Baldin,[12] J. Bantly,[4] J.F. Bartlett,[12] K. Bazizi,[7] J. Bendich,[20] S.B. Beri,[31] I. Bertram,[34] V.A. Bezzubov,[32] P.C. Bhat,[12] V. Bhatnagar,[31] M. Bhattacharjee,[11] A. Bischoff,[7] N. Biswas,[30] G. Blazey,[12] S. Blessing,[13] P. Bloom,[5] A. Boehnlein,[12] N.I. Bojko,[32] F. Borcherding,[12] J. Borders,[35] C. Boswell,[7] A. Brandt,[12] R. Brock,[23] A. Bross,[12] D. Buchholz,[29] V.S. Burtovoi,[32] J.M. Butler,[12] D. Casey,[35] H. Castilla-Valdez,[9] D. Chakraborty,[38] S.-M. Chang,[27] S.V. Chekulaev,[32] L.-P. Chen,[20] W. Chen,[38] L. Chevalier,[36] S. Chopra,[31] B.C. Choudhary,[7] J.H. Christenson,[12] M. Chung,[15] D. Claes,[38] A.R. Clark,[20] W.G. Cobau,[21] J. Cochran,[7] W.E. Cooper,[12] C. Cretsinger,[35] D. Cullen-Vidal,[4] M.A.C. Cummings,[14] D. Cutts,[4] O.I. Dahl,[20] K. De,[41] M. Demarteau,[12] R. Demina,[27] K. Denisenko,[12] N. Denisenko,[12] D. Denisov,[12] S.P. Denisov,[32] W. Dharmaratna,[13] H.T. Diehl,[12] M. Diesburg,[12] G. Di Loreto,[23] R. Dixon,[12] P. Draper,[41] J. Drinkard,[6] Y. Ducros,[36] S.R. Dugad,[40] S. Durston-Johnson,[35] D. Edmunds,[23] J. Ellison,[7] V.D. Elvira,[12,*] R. Engelmann,[38] S. Eno,[21] G. Eppley,[34] P. Ermolov,[24] O.V. Eroshin,[32] V.N. Evdokimov,[32] S. Fahey,[23] T. Fahland,[4] M. Fatyga,[3] M.K. Fatyga,[35] J. Featherly,[3] S. Feher,[38] D. Fein,[2] T. Ferbel,[35] G. Finocchiaro,[38] H.E. Fisk,[12] Yu. Fisyak,[24] E. Flattum,[23] G.E. Forden,[2] M. Fortner,[28] K.C. Frame,[23] P. Franzini,[10] S. Fuess,[12] A.N. Galjaev,[32] E. Gallas,[41] C.S. Gao,[12,†] S. Gao,[12,†] T.L. Geld,[23] R.J. Genik II,[23] K. Genser,[12] C.E. Gerber,[12,‡] B. Gibbard,[3] M. Glaubman,[27] V. Glebov,[35] S. Glenn,[5] B. Gobbi,[29] M. Goforth,[13] A. Goldschmidt,[20] B. Gómez,[1] P.I. Goncharov,[32] H. Gordon,[3] L.T. Goss,[42] N. Graf,[3] P.D. Grannis,[38] D.R. Green,[12] J. Green,[28] H. Greenlee,[12] G. Griffin,[6] N. Grossman,[12] P. Grudberg,[20] S. Grünendahl,[35] W. Gu,[12,†] J.A. Guida,[38] J.M. Guida,[3] W. Guryn,[3] S.N. Gurzhiev,[32] Y.E. Gutnikov,[32] N.J. Hadley,[21] H. Haggerty,[12] S. Hagopian,[13] V. Hagopian,[13] K.S. Hahn,[35] R.E. Hall,[6] S. Hansen,[12] R. Hatcher,[23] J.M. Hauptman,[17] D. Hedin,[28] A.P. Heinson,[7] U. Heintz,[12] R. Hernández-Montoya,[9] T. Heuring,[13] R. Hirosky,[13] J.D. Hobbs,[12] B. Hoeneisen,[1,§] J.S. Hoftun,[4] F. Hsieh,[22] Ting Hu,[38] Tong Hu,[16] T. Huehn,[7] S. Igarashi,[12] A.S. Ito,[12] E. James,[2] J. Jaques,[30] S.A. Jerger,[23] J.Z.-Y. Jiang,[38] T. Joffe-Minor,[29] H. Johari,[27] K. Johns,[2] M. Johnson,[12] H. Johnstad,[39] A. Jonckheere,[12] M. Jones,[14] H. Jöstlein,[12] S.Y. Jun,[29] C.K. Jung,[38] S. Kahn,[3] J.S. Kang,[18] R. Kehoe,[30] M.L. Kelly,[30] A. Kernan,[7] L. Kerth,[20] C.L. Kim,[18] S.K. Kim,[37] A. Klatchko,[13] B. Klima,[12] B.I. Klochkov,[32] C. Klopfenstein,[38] V.I. Klyukhin,[32] V.I. Kochetkov,[32] J.M. Kohli,[31] D. Koltick,[33] A.V. Kostritskiy,[32] J. Kotcher,[3] J. Kourlas,[26] A.V. Kozelov,[32] E.A. Kozlovski,[32] M.R. Krishnaswamy,[40] S. Krzywdzinski,[12] S. Kunori,[21] S. Lami,[38] G. Landsberg,[12] R.E. Lanou,[4] J-F. Lebrat,[36] A. Leflat,[24] H. Li,[38] J. Li,[41] Y.K. Li,[29] Q.Z. Li-Demarteau,[12] J.G.R. Lima,[8] D. Lincoln,[22] S.L. Linn,[13] J. Linnemann,[23] R. Lipton,[12] Y.C. Liu,[29] F. Lobkowicz,[35] S.C. Loken,[20] S. Lökös,[38] L. Lueking,[12] A.L. Lyon,[21] A.K.A. Maciel,[8] R.J. Madaras,[20] R. Madden,[13] I.V. Mandrichenko,[32] Ph. Mangeot,[36] S. Mani,[5] B. Mansoulié,[36] H.S. Mao,[12,†] S. Margulies,[15] R. Markeloff,[28] L. Markosky,[2] T. Marshall,[16] M.I. Martin,[12] M. Marx,[38] B. May,[29] A.A. Mayorov,[32] R. McCarthy,[38] T. McKibben,[15] J. McKinley,[23] H.L. Melanson,[12] J.R.T. de Mello Neto,[8] K.W. Merritt,[12] H. Miettinen,[34] A. Milder,[2] A. Mincer,[26] J.M. de Miranda,[8] C.S. Mishra,[12] M. Mohammadi-Baarmand,[38] N. Mokhov,[12] N.K. Mondal,[40] H.E. Montgomery,[12] P. Mooney,[1] M. Mudan,[26] C. Murphy,[16] C.T. Murphy,[12] F. Nang,[4] M. Narain,[12] V.S. Narasimham,[40] A. Narayanan,[2] H.A. Neal,[22] J.P. Negret,[1] E. Neis,[22] P. Nemethy,[26] D. Nešić,[4] D. Norman,[42] L. Oesch,[22] V. Oguri,[8] E. Oltman,[20] N. Oshima,[12] D. Owen,[23] P. Padley,[34] M. Pang,[17] A. Para,[12] C.H. Park,[12] Y.M. Park,[19] R. Partridge,[4] N. Parua,[40] M. Paterno,[35] J. Perkins,[41] A. Peryshkin,[12] M. Peters,[14] H. Piekarz,[13] Y. Pischalnikov,[33] A. Pluquet,[36] V.M. Podstavkov,[32] B.G. Pope,[23] H.B. Prosper,[13] S. Protopopescu,[3] D. Pušeljić,[20] J. Qian,[22] P.Z. Quintas,[12] R. Raja,[12] S. Rajagopalan,[38] O. Ramirez,[15] M.V.S. Rao,[40] P.A. Rapidis,[12] L. Rasmussen,[38] A.L. Read,[12] S. Reucroft,[27] M. Rijssenbeek,[38] T. Rockwell,[23] N.A. Roe,[20] P. Rubinov,[38] R. Ruchti,[30] S. Rusin,[24] J. Rutherfoord,[2] A. Santoro,[8] L. Sawyer,[41] R.D. Schamberger,[38] H. Schellman,[29] J. Sculli,[26] E. Shabalina,[24] C. Shaffer,[13] H.C. Shankar,[40] R.K. Shivpuri,[11] M. Shupe,[2] J.B. Singh,[31] V. Sirotenko,[28] W. Smart,[12] A. Smith,[2] R.P. Smith,[12] R. Snihur,[29] G.R. Snow,[25] S. Snyder,[38] J. Solomon,[15] P.M. Sood,[31] M. Sosebee,[41] M. Souza,[8] A.L. Spadafora,[20] R.W. Stephens,[41] M.L. Stevenson,[20] D. Stewart,[22] D.A. Stoianova,[32] D. Stoker,[6] K. Streets,[26] M. Strovink,[20] A. Taketani,[12] P. Tamburello,[21] J. Tarazi,[6] M. Tartaglia,[12] T.L. Taylor,[29] J. Teiger,[36] J. Thompson,[21] T.G. Trippe,[20] P.M. Tuts,[10] N. Varelas,[23] E.W. Varnes,[20] P.R.G. Virador,[20] D. Vititoe,[2] A.A. Volkov,[32] A.P. Vorobiev,[32] H.D. Wahl,[13] J. Wang,[12,†] L.Z. Wang,[12,†] J. Warchol,[30] M. Wayne,[30] H. Weerts,[23] W.A. Wenzel,[20] A. White,[41] J.T. White,[42] J.A. Wightman,[17] J. Wilcox,[27] S. Willis,[28] S.J. Wimpenny,[7] J.V.D. Wirjawan,[42] J. Womersley,[12] E. Won,[35] D.R. Wood,[12] H. Xu,[4] R. Yamada,[12] P. Yamin,[3] C. Yanagisawa,[38] J. Yang,[26]

*Also at CONICET, Argentina.
†Also at IHEP, Beijing, China.
‡Also at Universidad de Buenos Aires, Argentina.
§Also at Univ. San Francisco de Quito, Ecuador.

0556-2821/95/52(9)/4877(43)/$06.00

©1995 The American Physical Society

T. Yasuda,[27] C. Yoshikawa,[14] S. Youssef,[13] J. Yu,[35] Y. Yu,[37] Y. Zhang,[12,†] Y.H. Zhou,[12,†] Q. Zhu,[26] Y.S. Zhu,[12,†] Z.H. Zhu,[35] D. Zieminska,[16] A. Zieminski,[16] and A. Zylberstejn[36]

(D0 Collaboration)

[1] *Universidad de los Andes, Bogotá, Colombia*
[2] *University of Arizona, Tucson, Arizona 85721*
[3] *Brookhaven National Laboratory, Upton, New York 11973*
[4] *Brown University, Providence, Rhode Island 02912*
[5] *University of California, Davis, California 95616*
[6] *University of California, Irvine, California 92717*
[7] *University of California, Riverside, California 92521*
[8] *Laboratorio de Fisica Experimental de Altas Energias e Cosmologia, Centro Brasileiro de Pesquisas Físicas, Rio de Janeiro, Brazil*
[9] *Centro de Investigación y de Estudios Avanzados del Instituto Politécnico Nacional, Mexico City, Mexico*
[10] *Columbia University, New York, New York 10027*
[11] *Delhi University, Delhi, India 110007*
[12] *Fermi National Accelerator Laboratory, Batavia, Illinois 60510*
[13] *Florida State University, Tallahassee, Florida 32306*
[14] *University of Hawaii, Honolulu, Hawaii 96822*
[15] *University of Illinois at Chicago, Chicago, Illinois 60607*
[16] *Indiana University, Bloomington, Indiana 47405*
[17] *Iowa State University, Ames, Iowa 50011*
[18] *Korea University, Seoul, Korea*
[19] *Kyungsung University, Pusan, Korea*
[20] *Lawrence Berkeley Laboratory and University of California, Berkeley, California 94720*
[21] *University of Maryland, College Park, Maryland 20742*
[22] *University of Michigan, Ann Arbor, Michigan 48109*
[23] *Michigan State University, East Lansing, Michigan 48824*
[24] *Moscow State University, Moscow, Russia*
[25] *University of Nebraska, Lincoln, Nebraska 68588*
[26] *New York University, New York, New York 10003*
[27] *Northeastern University, Boston, Massachusetts 02115*
[28] *Northern Illinois University, DeKalb, Illinois 60115*
[29] *Northwestern University, Evanston, Illinois 60208*
[30] *University of Notre Dame, Notre Dame, Indiana 46556*
[31] *University of Panjab, Chandigarh 16-00-14, India*
[32] *Institute for High Energy Physics, 142-284 Protvino, Russia*
[33] *Purdue University, West Lafayette, Indiana 47907*
[34] *Rice University, Houston, Texas 77251*
[35] *University of Rochester, Rochester, New York 14627*
[36] *Commissanat à l' Energie Atomique, Departement d' Astro-Physique, de Physique des Particules, de Physique Nucléair et Instrumentation Associée/Service de Physique des Particules, Centre d' Etudes de Saclay, France*
[37] *Seoul National University, Seoul, Korea*
[38] *State University of New York, Stony Brook, New York 11794*
[39] *Superconducting Super Collider Laboratory, Dallas, Texas 75237*
[40] *Tata Institute of Fundamental Research, Colaba, Bombay 400005, India*
[41] *University of Texas, Arlington, Texas 76019*
[42] *Texas A&M University, College Station, Texas 77843*

(Received 23 May 1995)

We present results on the search for the top quark in $p\bar{p}$ collisions at $\sqrt{s} = 1.8$ TeV with an integrated luminosity of 13.5 ± 1.6 pb^{-1}. We have considered $t\bar{t}$ production in the standard model using electron and muon dilepton decay channels ($t\bar{t} \to e\mu +$ jets, $ee +$ jets, and $\mu\mu +$ jets) and single-lepton decay channels ($t\bar{t} \to e +$ jets and $\mu +$ jets) with and without tagging of b quark jets. An analysis of these data optimized for top quark masses below 140 GeV/c^2 gives a lower top quark mass limit of 128 GeV/c^2. An analysis optimized for higher top quark masses yields 9 events with an expected background of 3.8 ± 0.9. If we assume that the excess is due to $t\bar{t}$ production, and assuming a top mass of 180 GeV/c^2, we obtain a cross section of 8.2 ± 5.1 pb.

PACS number(s): 14.65.Ha, 13.85.Qk, 13.85.Rm

I. INTRODUCTION

Since the discovery of the τ lepton [1] and the b quark [2], the standard model of electroweak interactions [3,4] that incorporates three generations of quarks and leptons has come to be widely accepted. The b quark has been shown to possess a weak isospin component $I_3 = -1/2$ [5], which demands the existence of the isospin partner of the b quark, namely, the top quark. Searches for the top quark at hadron machines were begun in earnest with

the advent of the Super Proton Synchrotron ($Sp\bar{p}S$) at CERN [6] and continued at the Fermilab Tevatron [7], each search resulting in a higher mass limit for the top quark. The highest limit so far of 131 GeV/c^2 at 95% C.L. for the top quark mass was published by the D0 Collaboration [8] in 1994. Because of a recalibration of the luminosity [9] we are revising that limit downward to 128 GeV/c^2. In 1994, the Collider Detector at Fermilab (CDF) Collaboration [10] reported seeing evidence for a signal in a mass range of $174\pm10^{+13}_{-12}$ GeV/c^2 with a cross section of $13.9^{+6.1}_{-4.8}$ pb, based on 19.3 pb^{-1} of data, though they stopped short of claiming discovery. In 1995, both the D0 and the CDF Collaborations simultaneously announced [11,12] the observation of the top quark at masses 199^{+19}_{-21}(stat)$\pm$22(syst) GeV/c^2 and 176 ± 8(stat)±10(syst) GeV/c^2, respectively. The discovery was based on the 1992–1993 and the 1994–1995 data samples. We describe here the analysis based on the 1992–1993 data sample only.

The origins of the masses of fundamental particles are unknown and the relative heaviness of the top quark compared to its isospin partner remains a mystery. The fact that the top quark mass is so close to the electroweak symmetry-breaking scale has stimulated models [13] in which the top quark is intimately connected to the electroweak symmetry-breaking mechanism. These models, as well as supersymmetric grand unification models [14], demand a heavy top in the neighborhood of 200 GeV/c^2. Information on the top quark mass can also be indirectly obtained from measurements of electroweak radiative corrections that manifest themselves in the W/Z mass difference [15,16], forward-backward asymmetry measurements in Z boson decay [17,18], and ν scattering [19] that involves the exchange of W and Z bosons. Recent results from the CERN e^+e^- collider LEP [17] yield a value of 173^{+12+18}_{-13-20} GeV/c^2 for the top quark mass. When averaged with information available from neutrino experiments [19] and the collider W/Z mass difference data [15,16], the value of the top quark mass obtained [17] is 171^{+11+18}_{-12-19} GeV/c^2. The SLAC Large Detector (SLD) [18] measurements when included yield [17] a slightly higher value of the top quark mass of 178^{+11+18}_{-11-19} GeV/c^2. These indirect measurements however assume the completeness of the standard model.

Top production at the Tevatron collider is expected to proceed via the quark-antiquark annihilation diagram of the type shown in Fig. 1. The relative importance of the gluon fusion mechanism decreases with increasing top quark mass and is small at the masses of interest. The top quark production cross section has been calculated to the next to leading order (NLO) in QCD [20]. Recently, these calculations have been extended to higher order by taking into account the consequences of soft gluon emission [21] and we will be using these latter calculations in what follows to predict expected yields. The top cross section is a strong function of top mass, falling from a central value of 25.4 pb for m_t=130 GeV/c^2 to 2.26 pb for m_t=200 GeV/c^2. We ignore the electroweak production of single top quarks [22], which is expected to be relatively small at Tevatron energies. The top quark is expected

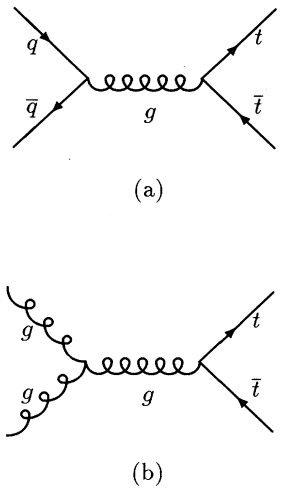

FIG. 1. Feynman diagrams typifying the production of $t\bar{t}$ pairs at the Tevatron. (a) involving $q\bar{q}$ fusion is dominant over the one involving gluon-gluon fusion (b) at top masses in excess of 100 GeV/c^2 at Tevatron energies.

to decay predominantly into a W and a b quark in the standard model. We do not consider here decay mechanisms whereby the top quark decays predominantly into a charged Higgs boson [23]. The channels in which we search for the top quark are thus determined by the decay modes of the two W bosons in the $t\bar{t}$ event. The W boson can decay leptonically into an electron, muon, or a τ lepton (and associated neutrino), and hadronically into $u\bar{d}$ or $c\bar{s}$ pairs. Table I contains the decay branching fractions of the $t\bar{t}$ pair, assuming quark lepton universality and three color degrees of freedom for the quarks. The channel where both the W bosons decay hadronically is the most copious. However, this has formidable background contributions from QCD multijet production and will not be reported here. D0 currently does not have a τ lepton identification capability, so top decays contain-

TABLE I. $t\bar{t}$ branching fractions can be read off from the table which displays the W^+W^- decay branching fractions, and the resulting $t\bar{t}$ final state combinations. Measurements of the channels marked with an asterisk are described in this paper. It can be seen that the total branching fraction for top to e or μ + jets is 24/81. Also the dilepton decay modes ee and $\mu\mu$ each have a branching fraction 1/81 whereas $e\mu$ has a branching fraction 2/81.

W^+/W^-decay modes	$W^+ \to c\bar{s}, u\bar{d}$ (6/9)	$W^+ \to e^+\nu_e$ (1/9)	$W^+ \to \mu^+\nu_\mu$ (1/9)	$W^+ \to \tau^+\nu_\tau$ (1/9)
$W^- \to \bar{c}s, \bar{u}d$ (6/9)	36/81	6/81*	6/81*	6/81
$W^- \to e^-\bar{\nu_e}$ (1/9)	6/81*	1/81*	1/81*	1/81
$W^- \to \mu^-\bar{\nu_\mu}$ (1/9)	6/81*	1/81*	1/81*	1/81
$W^- \to \tau^-\bar{\nu_\tau}$ (1/9)	6/81	1/81	1/81	1/81

ing a τ will only enter indirectly as small contributions to other channels when the τ decays into other leptons. The remaining channels can be classified as follows: the dilepton channel where both W bosons decay leptonically into an electron or a muon and the lepton + jets channel where one of the W bosons decays leptonically and the other hadronically. All these channels are characterized by high transverse momentum leptons and jets as well as missing transverse momentum carried off by neutrinos. The dilepton channels ee and $\mu\mu$ have a large background contribution from Z decays. All of the dilepton channels have background contributions from $b\bar{b}$ decays and WW pair production and decays, but these backgrounds tend to decrease with increasing jet multiplicity.

The lepton + jets channel is more copious than the dilepton channels by a factor of 6. However, Drell-Yan production of W bosons accompanied by jets is a serious background to this channel. We make topological and kinematical requirements on these events in order to enhance our signal-background ratios. Since this channel is more copious, we can also control the background by demanding a muon tag in the event from one of the two b quarks in the decay. Conventionally decaying $t\bar{t}$ events each contain a $b\bar{b}$ pair, which through sequential decay ensure that ~44% of the top events will have a tagging muon. Given our muon detection efficiency, we expect to tag ~20% of the top events with a muon. The background W+jets events are expected to be much less rich in b quarks, giving us a more favorable signal-background ratio with the μ tag. We thus present two orthogonal analyses of lepton + jets, the first of which considers events with no detected tagging muon and the other where a tagging muon is detected.

The paper is structured as follows. In Secs. II and III we briefly describe the detector and the triggers employed in the top quark search in D0 . In Sec. IV, we describe the reconstruction program and the algorithms employed in recognizing jets, electrons, muons, and missing transverse momentum. In Sec. V, we describe the programs used to simulate the $t\bar{t}$ and W + jets Monte Carlo samples. In Sec. VI, we describe the analysis of dilepton candidates and in Sec. VII, we describe the analysis of lepton + jets candidates. In Sec. VIII, we describe the analysis of lepton + jets events that contain a tagging muon. We have conducted a search for "low mass top," resulting in the limit of 128 GeV/c^2 and another one optimized for masses higher than that, where we have adjusted the cuts to increase the ratio of "expected signal"/$\sqrt{\text{background}}$ from 1.5 to 2.5 for a top mass of 160 GeV/c^2. The "low mass" analysis will be referred to in this paper as analysis I and the "high mass" search will be referred to as analysis II. The resulting $t\bar{t}$ cross sections and errors are presented in Sec. IX and the conclusions to be drawn from the combined analyses are presented in Sec. X.

II. THE D0 DETECTOR

D0 is a multipurpose detector designed to study $p\bar{p}$ collisions at the Fermilab Tevatron Collider. The detector was commissioned during the summer of 1992. The work presented here is based on 13.5 pb^{-1} of collider data recorded between August 1992 and May 1993. A full description of the detector may be found in Ref. [24]. Here we describe briefly the properties of the detector that are relevant for the top quark search.

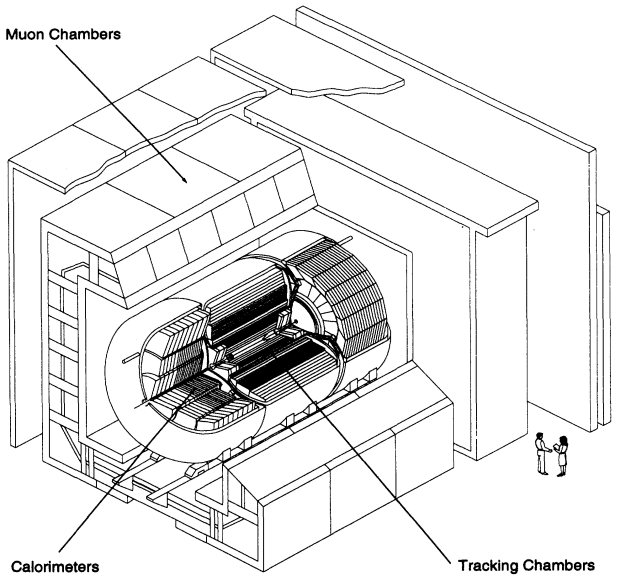

FIG. 2. Cutaway isometric view of the D0 detector.

The detector was designed to have good electron and muon identification capabilities and to measure jets and missing transverse energy $\not\!\!E_T$ with good resolution. The detector consists of three primary systems: a nonmagnetic central tracking system, a hermetic uranium-liquid argon calorimeter, and a muon spectrometer. A cutaway view of the detector is shown in Fig. 2.

A. Central tracking system

The central tracking system consists of four detector subsystems: a vertex drift chamber (VTX), a transition radiation detector (TRD), a central drift chamber (CDC), and two forward drift chambers (FDC's). The system provides charged particle tracking over the region $|\eta| < 3.2$ in pseudorapidity, where $\eta = \text{arctanh}^{-1}(\cos\theta)$; θ, ϕ = polar, azimuthal angle. It measures the trajectories of charged particles with a resolution of 2.5 mrad in ϕ and 28 mrad in θ. From these measurements the position of the interaction vertex along the beam direction (z) can be determined with a resolution of 8 mm. The central tracking system also measures the ionization of tracks to distinguish single charged particles and e^+e^- pairs from photon conversions.

B. Calorimeter

The calorimeter is divided into three parts, a central calorimeter (CC) and two end calorimeters (EC's). They

each consist of an inner electromagnetic (EM) section, a fine hadronic (FH) section, and a coarse hadronic (CH) section, housed in a steel cryostat. The intercryostat detector (ICD) consists of scintillator tiles inserted in the space between the EC and CC cryostats. The ICD improves the energy resolution for jets that straddle two cryostats. The calorimeter covers the pseudorapidity range $|\eta| < 4.2$.

Each EM section is 21 radiation lengths deep and is divided into four longitudinal segments (layers). The hadronic sections are 7–9 nuclear interaction lengths deep and are divided into four (CC) or five (EC) layers. The calorimeter is transversely segmented into pseudoprojective towers with $\Delta\eta \times \Delta\phi = 0.1 \times 0.1$. The third layer of the EM calorimeter, in which the maximum of EM showers is expected, is segmented twice as finely into cells with $\Delta\eta \times \Delta\phi = 0.05 \times 0.05$. With this fine segmentation the azimuthal position resolution for electrons above 50 GeV energy is about 2.5 mm. The energy resolution is $\sigma(E)/E = 15\%/\sqrt{E(\mathrm{GeV})} \oplus 0.4\%$ for electrons. For charged pions the resolution is about $50\%/\sqrt{E(\mathrm{GeV})}$ and for jets about $80\%/\sqrt{E(\mathrm{GeV})}$ [24]. For minimum bias data the resolution for each component of $\not\!\!E_T$, $\not\!\!E_x$, and $\not\!\!E_y$ has been measured to be $1.08\ \mathrm{GeV} + 0.019(\Sigma E_T)$, where ΣE_T is the scalar sum of the transverse energies in all calorimeter cells.

C. Muon spectrometer

The D0 detector has muon detection systems covering $|\eta| \leq 3.3$. Since muons from top quark decays populate predominantly the central region, this work uses only the wide angle muon spectrometer (WAMUS) which consists of four planes of proportional drift tubes (PDT's) in front of magnetized iron toroids with a magnetic field of 1.9 T and two groups of three planes each of proportional drift tubes behind the toroids. The magnetic field lines and the wires in the drift tubes are oriented transversely to the beam direction. The WAMUS covers the region $|\eta| < 1.7$ over the entire azimuth, with the exception of the central region below the calorimeter ($|\eta| < 1$, $225° < \phi < 315°$), where the inner layer is missing to make room for the calorimeter support structure.

The material in the calorimeter and iron toroids combined varies between 13 and 19 interaction lengths, making background from hadronic punchthrough negligible. The D0 detector is significantly more compact than previous magnetic $p\bar{p}$ collider detectors [25,26] and the small tracking volume reduces backgrounds to prompt muons from in-flight decays of π and K mesons.

The muon momentum p is measured from its deflection angle in the magnetic field of the toroid. The momentum resolution is limited by multiple scattering in the material traversed, knowledge of the magnetic field integral, and resolution of the deflection angle measurement. The resolution for $1/p$ is approximately Gaussian and given by $\sigma(1/p) = 0.18(p-2)/p^2 \oplus 0.008$ (with p in GeV/c) for the algorithm that was used to select the data presented here.

III. TRIGGERS

D0 has a multilevel trigger system to reduce the event rate from the beam crossing frequency (286 kHz) to the rate at which events can be written to tape ($\approx$ 2 Hz). For every trigger we require a coincidence between hits in scintillation counters located in front of each EC (level 0). A logic network implemented in hardware takes a trigger decision based on fast, analogue sums of transverse energy in calorimeter trigger towers with $\Delta\eta \times \Delta\phi = 0.2 \times 0.2$ which are segmented longitudinally in EM and FH sections, and hit patterns in the muon spectrometer (level 1). This decision is completed between beam crossings so that no dead time is incurred at this level. A farm of 48 Vax station 4000/60 computers filters the events based on the complete information read out from the front-end electronics (level 2).

The main ring synchrotron beam pipe passes through the coarse hadronic section of the calorimeter. This synchrotron accelerates protons used to create and accumulate antiprotons while beams are colliding in the Tevatron. Losses from the main ring beam may cause background in the calorimeter. In the analyses presented in this paper, we do not use any triggers taken when a main ring bunch passed through the calorimeter.

The triggers used for the $t\bar{t}$ searches described here are defined in terms of combinations of specific objects (electron, muon, jet, $\not\!\!E_T$) required in the level 1 and level 2 triggers. The thresholds on p_T, E_T, and $\not\!\!E_T$ have been chosen to give the optimal acceptance for $t\bar{t}$ events while maintaining a substantial rejection against background. The basic elements of the triggers used are summarized below.

A. Electron trigger

To trigger on electrons, level 1 requires the transverse energy in the EM section of a trigger tower to be above programmed thresholds.

The level 2 electron algorithm uses the full segmentation of the EM calorimeter to identify electron showers. Using the trigger towers that were above threshold at level 1 as seeds, the algorithm forms clusters which include all cells in the four EM layers and the first FH layer in a region of $\Delta\eta \times \Delta\phi = 0.3 \times 0.3$, centered around the tower with the highest E_T. The longitudinal and transverse energy profile of the cluster must satisfy the following requirements.

The fraction of the cluster energy in the EM section must be above a given threshold which is dependent on the energy and the position of the cluster in the detector.

The transverse shape classification is based on the energy deposition pattern in the third EM layer. The difference of the energy depositions in two regions, covering $\Delta\eta \times \Delta\phi = 0.25 \times 0.25$ and 0.15×0.15 and centered on the cell with the highest E_T, must be within a window, which depends on the total cluster energy.

The efficiency of the level 2 electron algorithm as measured with collider data is $(95 \pm 3)\%$.

B. Jet trigger

Level 1 jet triggers require the sum of the transverse energy in the EM and FH sections of a trigger tower to be above programmed thresholds.

The level 2 jet algorithm begins with an E_T ordered list of towers that were above threshold at level 1. At level 2 a jet is formed by placing a cone of given radius R, where $R = \sqrt{\Delta\eta^2 + \Delta\phi^2}$, around the seed tower from level 1. If another seed tower lies within the jet cone then it is passed over and not allowed to seed a new jet. The summed E_T in all of the towers included in the jet cone defines the jet E_T. If any two jet cones overlap, then the towers in the overlap region are added into the jet candidate which was formed first. For triggers used in top quark searches we use jet cones with radius $R = 0.3$. To filter events, cuts on several quantities can be imposed. These are the minimum transverse energy of a jet, the minimum transverse size of a jet, the minimum number of jets, and the fiducial cuts on the pseudorapidity of the jets.

C. Missing transverse energy trigger

At level 2 $\not\!\!E_T$ is computed using the vector sum of E_T of all calorimeter and ICD cells with respect to the z position of the interaction vertex, which is determined from the timing of the hits in the level 0 counters. At level 2, we can require that the $\not\!\!E_T$ in the event be above a threshold.

D. Muon trigger

The muon level 1 trigger system provides the number of muon candidates in different regions of the muon spectrometer. The algorithm combines PDT cells into 60-cm-wide hodoscopic elements, and searches for hit patterns consistent with a muon originating at the vertex. In the central region, three PDT chambers, each with two hit planes, are required except in regions where detector services and support limit the coverage; in those regions, two chambers with two hit planes are required. In the forward region with $1.0 < |\eta| < 1.7$, three chambers are required with three hit planes in the chamber between the calorimeter and iron, and two planes each in the two chambers outside the iron. The trigger requires a minimum p_T of 3 GeV/c and becomes fully efficient at about 6 GeV/c.

At level 2, the full digitized data are available, and the first stage of the off-line reconstruction is performed. To minimize processing time, the search for muon candidates is restricted in the forward region to those sectors which had a level 1 trigger. Valid level 2 triggers required a three-dimensional track consisting of hits in at least two planes in two PDT chambers. The residuals in the PDT drift view and along the PDT wire, and the projections of the track to the primary vertex in both views were used to define a track quality. Those with at least three out of four of these variables consistent with a beam produced muon were considered as valid muons. In the forward region, a variable related to the number of hits on the track was added to the track quality definition in order to reduce the number of combinations. In the central region, cosmic ray muons are suppressed if there is evidence of a single muon penetrating the entire detector. Muon candidates with a track in the opposite muon chambers within 20° in ϕ and 10° in θ are rejected, as are those candidates with PDT chamber hits on the opposite side within 60 cm (roughly 5°) of the projected candidate trajectory.

The muon momentum determined in level 2 uses the muon PDT hits plus the vertex formed using the level 0 trigger. The momentum resolution for high momentum muons at level 2 is degraded to about $\sigma(1/p) = 0.012$ $(\text{GeV}/c)^{-1}$ as a result of less precise vertex information than that available in the off-line reconstruction, but for

TABLE II. Triggers used in $t\bar{t}$ analysis.

Trigger name	Level 1	Level 2	Used in channels
MU-ELE (Express)	1 EM tower, $E_T > 7$ GeV 1 μ, $\|\eta\| < 1.7$	1 e, $E_T > 7$ GeV 1 μ, $p_T > 5$ GeV/c	$e\mu$
ELE-JET	1 EM tower, $E_T > 10$ GeV 2 EM+FH tower, $E_T > 5$ GeV	1 e, $E_T > 15$ GeV 2 jets, $E_T > 10$ GeV $\not\!\!E_T > 10$ GeV	ee, e + jets
ELE-JET-MAX (Express)	1 EM tower, $E_T > 10$ GeV 2 EM+FH towers, $E_T > 5$ GeV	1 e, $E_T > 12$ GeV 2 jets, $E_T > 16$ GeV $\not\!\!E_T > 10$ GeV	$e\mu$, e + jets
ELE-HIGH	1 EM tower, $E_T > 10$ GeV	1 $e > 20$ GeV	ee, e + jets
ELE-MAX (Express)	1 EM tower, $E_T > 10$ GeV	1 $e > 20$ GeV $\not\!\!E_T > 20$ GeV	ee, e + jets
ELE-2-HIGH	2 EM towers, $E_T > 7$ GeV	2 $e > 10$ GeV	ee
MU-JET-MAX (Express)	1 μ, $\|\eta\| < 1.7$ 1 EM+FH tower, $E_T > 5$ GeV	1 μ, $p_T > 14$ GeV/c 1 jet, $E_T > 15$ GeV	$e\mu$, $\mu\mu$, μ + jets
MU-JET-HIGH	1 μ, $\|\eta\| < 1.7$ 1 EM+FH tower, $E_T > 5$ GeV	1 μ, $p_T > 8$ GeV/c 1 jet, $E_T > 15$ GeV	μ + jets

the top triggers, muon p_T thresholds are at 5 and 8 GeV/c, and so this has a negligible effect on the trigger efficiency. The muon level 2 trigger efficiency was determined to be $(95 \pm 3)\%$ excluding effects of chamber efficiencies and acceptance.

The level 1 muon trigger efficiency is determined using events selected by the presence of reconstructed muons in non-muon triggers. The resulting efficiencies are $(67 \pm 3)\%$ for $|\eta| < 1.0$ and $(15 \pm 3)\%$ in the range $1.0 < |\eta| < 1.7$. The trigger efficiency is the product of two terms. The three-chamber requirement gives geometric factors of about 0.79 and 0.48 in the central and end regions, while chamber cell efficiencies contribute factors of 0.85 and 0.31 to the two regions.

E. Specific triggers used for $t\bar{t}$ searches

For the $t\bar{t}$ decay modes considered in this paper, we use trigger conditions listed in Table II. The first column gives the name of the trigger condition. Triggers marked "Express" were written to the Express data stream which contained a subset of all triggers for fast reconstruction. The second column lists the requirements imposed at level 1 and the third column the requirements imposed at level 2 in terms of the objects defined above. The last column indicates the channels for which the triggers were used. Most channels used the logical OR of several triggers. The integrated luminosity for triggers used in top quark searches for $e\mu$, ee, and e+jets final states is 13.5 ± 1.6 pb^{-1}. The triggers used for $\mu\mu$ and μ+jets analyses correspond to a lower integrated luminosity of 9.8 ± 1.2 pb^{-1}.

IV. EVENT RECONSTRUCTION

A. Electron identification

Electrons are identified by the detection of an electromagnetic shower in the calorimeter with an associated track in the central tracking system. Electromagnetic showers are characterized by making a comparison of the longitudinal and transverse profiles in the electromagnetic (EM) calorimeter to simulated electron showers. The first step in electron identification is the formation of clusters of adjacent EM calorimeter towers with significant energy depositions using a nearest neighbor clustering algorithm. Following cluster formation there are two steps which lead to the selection of electron candidates: EM shower identification using calorimeter shape analysis and requiring a matching track to discriminate against π^0 and γ backgrounds. The variables used in this analysis are described below.

1. *Minimum electromagnetic energy fraction*

For electrons at least 90% of the cluster energy must be contained within the EM calorimeter. Charged hadrons on average deposit less than 10% of their energy in the electromagnetic section of the calorimeter. Therefore this cut provides powerful discrimination against charged hadrons and is more than 99% efficient for electrons with energies between 10 and 150 GeV as determined in test beam measurements.

2. *Covariance matrix χ^2*

The shower shape may be characterized by the fraction of the cluster energy deposited in each layer of the calorimeter. These fractions are also dependent on the incident electron energy. However, these fractions are correlated, i.e., a shower which fluctuates and deposits a large fraction of its energy in the first layer will then deposit a smaller fraction in the subsequent layers and vice versa.

To take into account simultaneously both the energy observed in a given layer and its correlations with the energy deposited in the other layers, we use a covariance matrix (M) of 41 observables x_i to characterize the *electron-ness* of the shower [27]. The matrix elements are computed from a reference sample of N Monte Carlo electrons with energies ranging between 10 and 150 GeV. They are defined as

$$M_{ij} = \frac{1}{N}\sum_{n=1}^{N}(x_i{}^n - \bar{x}_i)(x_j{}^n - \bar{x}_j), \tag{1}$$

where $x_i{}^n$ is the value of the ith observable for the nth electron and $\bar{x}_i$ is the mean of the ith observable. The observables are the fractional energies in layers 1, 2, 4 of the EM calorimeter, and the fractional energy in each cell of a 6×6 array of cells in layer 3 centered on the most energetic tower in the EM cluster. The logarithm of the cluster energy is included as an observable to take into account the dependence of the fractional energy deposits on the cluster energy. Finally, the position of the event vertex along the beam direction is included, to take into account the dependence of the electron shower shape on the point from which the electron originated. There are a total of 37 matrices, one for each of the 37 towers into which half the calorimeter is subdivided in pseudorapidity. The other half of the calorimeter with negative z coordinate is handled using reflection symmetry. For a shower, characterized by the observables x_i', the covariance parameter

$$\chi^2 = \sum_{i,j=1}^{41}(x_i' - \bar{x}_i)H_{ij}(x_j' - \bar{x}_j), \tag{2}$$

where $H = M^{-1}$, measures how consistent its shape is with that expected from an electromagnetic shower. In general, the values of the observables x_i are not normally distributed and therefore the covariance parameter χ^2 does not follow a χ^2 distribution. Since H is a symmetric matrix, it can be diagonalized using an appropriate unitary matrix U. Then χ^2 is given by

$$\chi^2 = yH'y^T \tag{3}$$

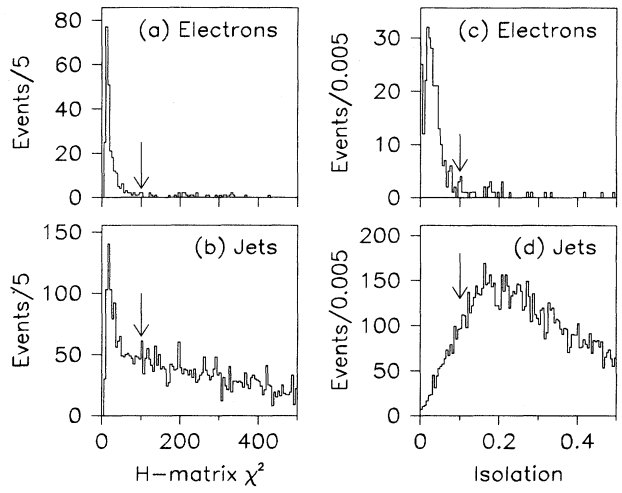

FIG. 3. Comparison of the covariance parameter χ^2 for electrons from (a) $Z \to ee$ decays and (b) EM clusters in inclusive jet data. (c) and (d) show the distribution of isolation variables for electrons from $Z \to ee$ decays and EM clusters in inclusive jet data, respectively. Arrows describe the selection cuts used (see text).

so that the transformed matrix $H' = U^T H U$ is diagonal and the components of the vector y are uncorrelated variables. The matrices, as mentioned, are calculated using Monte Carlo events. Slight differences in shower shapes between Monte Carlo events and data can cause large contributions to χ^2, if the eigenvalues of the matrices are unusually large. To prevent any component from dominating the value of the covariance variable χ^2, we limit the magnitude of the diagonal elements of H' to a maximum value, which optimizes the electron finding efficiency and rejection power.

Figures 3(a) and 3(b) show the distribution of χ^2 for electron candidates from $Z \to ee$ decays compared to that for EM clusters in inclusive jet data which are mainly due to backgrounds primarily from charged and neutral particle overlaps and π^0 decays. We require that the χ^2 for 41 degrees of freedom is less than 100 for electron candidates in the central calorimeter (CC) and less than 200 for those in the forward calorimeters (EC). This requirement is about 94% efficient for electrons with a rejection factor of about 4 against EM clusters that are not due to electrons.

3. *Cluster isolation*

We require EM clusters to be isolated from other particles in the event. Let $E(0.4)$ be the energy deposited in all calorimeter cells in the cone $R < 0.4$ around the electron direction and $EM(0.2)$ the energy deposited in the EM calorimeter in the cone $R < 0.2$. The isolation variable is then defined as the ratio

$$\mathrm{f_{iso}} = \frac{E(0.4) - EM(0.2)}{EM(0.2)}. \tag{4}$$

In Fig. 3(c), we plot $\mathrm{f_{iso}}$ for electron candidates from $Z \to ee$ decays. Figure 3(d) is the histogram of the distribution of $\mathrm{f_{iso}}$ for EM clusters in an inclusive jet sample. A requirement of $\mathrm{f_{iso}} < 0.1$ is 98% efficient in selecting electron candidates from W and Z decays.

4. *Cluster–track match*

An important source of background for electrons is photons from the decay of π^0 or η mesons which are copiously produced in $p\bar{p}$ collisions. This background can be reduced by requiring a track consistent with the passage of a charged particle in the central detector which points to the cluster. By demanding a good spatial match between cluster and track, backgrounds due to accidental overlaps of charged particles with photons are also reduced. To determine the shower centroid $\vec{x}_c$ in the calorimeter, we form the weighted mean of the coordinates $\vec{x}_i$ of all cells containing the shower,

$$\vec{x}_c = \frac{\sum_i w_i \vec{x}_i}{\sum_i w_i}. \tag{5}$$

The weights w_i are defined as

$$w_i = \max\left(0, w_0 + \ln\left(\frac{E_i}{E}\right)\right), \tag{6}$$

where E_i is the energy in the ith cell, E the energy of the cluster, and w_0 a parameter, chosen to optimize the position resolution. This logarithmic weighting is motivated by the exponential lateral profile of an electromagnetic shower. Using electrons from collider data, we measure the azimuthal position resolution in the CC and EC to be ≈ 2.5 mm.

In order to match the shower centroid to a reconstructed track, we point the track into the calorimeter and cut on the significance S of the mismatch between them. For the CC this quantity is

$$S_{\mathrm{CC}} = \sqrt{\left(\frac{\Delta\phi}{\delta_{\Delta\phi}}\right)^2 + \left(\frac{\Delta z}{\delta_{\Delta z}}\right)^2}, \tag{7}$$

where $\Delta\phi$ is the azimuthal mismatch, Δz the mismatch along the beam direction, and δ_x is the resolution for observable x. For the EC,

$$S_{\mathrm{EC}} = \sqrt{\left(\frac{\Delta\phi}{\delta_{\Delta\phi}}\right)^2 + \left(\frac{\Delta r}{\delta_{\Delta r}}\right)^2}, \tag{8}$$

where Δr is the mismatch transverse to the beam. The distribution of the track match significance variable S for electron candidates from $Z \to ee$ decays is shown in Fig. 4(a). Requiring $S < 5$ is 94 (74)% efficient for CC (EC) electron candidates. The corresponding distribu-

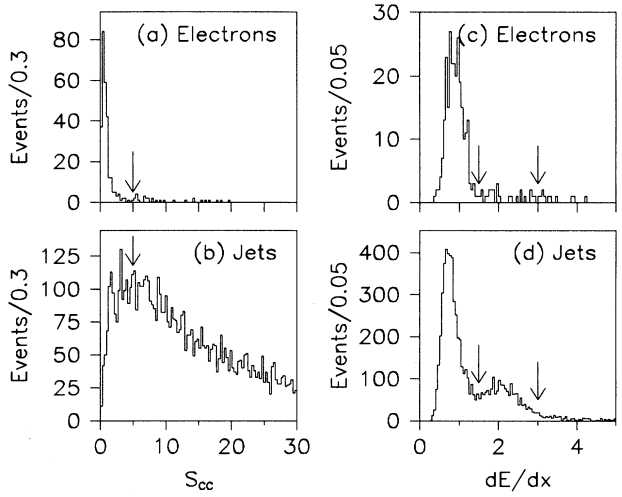

FIG. 4. Distribution of track match significance, S, for the electrons from (a) $Z \to e^+e^-$ events and (b) EM clusters in inclusive jet data. (c) and (d) show the distribution of the dE/dx variable for electrons from $Z \to ee$ decays and EM clusters in inclusive jet data, respectively. Arrows indicate the placement of selection cuts (see text).

tion for tracks associated with EM clusters in an inclusive jet sample is given in Fig. 4(b).

5. *Track ionization*

Since there is no central magnetic field, e^+e^- pairs from photon conversions in the material in front of the tracking chambers are not bent apart and often are reconstructed as a single track. For an e^+e^- pair the ionization in the tracking chambers is expected to be twice that of a single charged particle. The distribution of ionization per unit length (dE/dx) for tracks associated with EM clusters in the inclusive jet data sample shows a two-peak structure [Fig. 4(d)]. The lower peak is due to single charged particles and the higher peak arises from unresolved e^+e^- pairs. In Fig. 4(c), the dE/dx distribution of electrons from $Z \to e^+e^-$ decays is shown. Most electrons have $dE/dx \sim 1$ but there is a long tail to higher values due to electrons which start to shower earlier in the tracking chambers before the CDC and FDC. Backgrounds due to conversions can be reduced by rejecting tracks in a window of dE/dx around 2, which is the region populated by conversions. This cut is 92 (86)% efficient for CC (EC) electron candidates.

For the analyses described in this paper, we combine these quantities to define two different sets of *tight* and *loose* electron identification criteria. The cuts used and the corresponding identification efficiencies are listed in Table III for both the central (CC) and end calorimeters (EC). These vary between 43% and 80% depending on the choice of *tight* or *loose* criteria and whether the electron is measured in the CC or EC. Also, we use only electrons with $|\eta| \leq 2.5$, as the electrons from $t\bar{t}$ decays are very central.

TABLE III. Definition of *loose* and *tight* electron identification criteria for the low mass analysis (I) and high mass analysis (II).

Type	Definition	Efficiency (%) in CC (EC)
Loose I	$f_{iso} < 0.1$ $\chi^2 < 100$ (CC), 200 (EC)	79±3 (80±8)
Tight I	$f_{iso} < 0.1$ $\chi^2 < 100$ (CC), 200 (EC) $S < 5.0$	77±3 (60±6)
Loose II	$f_{iso} < 0.1$ $\chi^2 < 100$ (CC), 100 (EC) $S < 5.0$	77±3 (57±6)
Tight II	$f_{iso} < 0.1$ $\chi^2 < 100$ (CC), 100 (EC) $S < 5.0$ $\lvert\eta\rvert < 1.2 : dE/dx < 1.5$ or > 3.0 $\lvert\eta\rvert > 1.2 : dE/dx < 1.3$ or > 2.5	72±3 (43±5)

B. Muon identification

Muons are reconstructed as tracks in the muon PDT's. To identify muons from W boson and b quark decays in $t\bar{t}$ events and to reject combinatoric and cosmic ray backgrounds, we impose additional cuts on the properties of the reconstructed track. Finally, we classify the muons based on their p_T and isolation from other activity in the event.

The transverse momentum of the muon is computed from the deflection in the magnetized toroid. The momentum calculation uses a least-squares method which considers seven parameters: four describing the position and angle of the track before the calorimeter (in both the bend and nonbend views); two describing the effects due to multiple scattering; and the inverse of the muon momentum $1/p$. This seven-parameter fit is applied to 16 data points: vertex position measurements along the x and y directions, the angles and positions of track segments before and after the calorimeter and outside of the iron, and two angles representing the multiple scattering of the muon in the calorimeter. Energy loss corrections are then applied using the restricted energy loss formula as parametrized in GEANT [28].

The muon momentum resolution depends upon the amount of material traversed, the magnetic field integral, and the precision of the measurement of the muon bend angle using the muon and central tracking chambers. The momentum resolution was estimated by studying $Z \to \mu^+\mu^-$ events. A momentum resolution function of $\sigma(1/p) = 0.18(p-2)/p^2 \oplus 0.008$ (with p in GeV/c) best matches the data. The first of the two components in the above resolution function arises due to multiple Coulomb scattering in the iron toroids and is the dominant effect

for low momentum muons. The second component is due to the resolution of the muon position measurements.

A cut on $|\eta| < 1.7$ is imposed to restrict the muon tracks to those totally contained within the WAMUS spectrometer. Since the decay products from the top quark are central, this cut does not significantly affect the acceptance.

In the following we describe the quantities used to characterize muon tracks in detail. The muon definitions differ slightly among the $e\mu$, $\mu\mu$, $e+$jets, and $\mu+$jets analyses, because the magnitude and nature of backgrounds vary from channel to channel.

1. *Cosmic ray rejection*

We define the impact parameter (IP) as the distance of closest approach in the bend view plane of the muon track to the reconstructed vertex. We require this to be ≤ 22 cm to aid in cosmic ray rejection. For tight muons we define two additional impact-parameter-like quantities: (1) in the CF region, the distance between the z intersection of the track in the bend view plane and the z position of the reconstructed vertex. The definition is similar for the EF region. Although this quantity is not truly an impact parameter, it is referred to as the "bend view impact parameter," IP(bend). Note that IP = IP(bend)sinθ. And (2) in the CF region, the distance between the muon track projected to 0 in the interchamber view (the y intersection for top and bottom tracks and the x intersection for side tracks) and the origin.

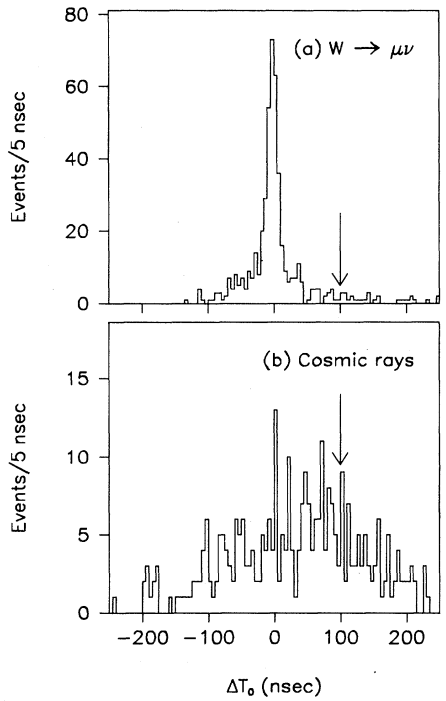

FIG. 5. ΔT_0 for muons from $W \rightarrow \mu\nu$ decays and cosmic ray muons. The arrow represents the selection cut (see text).

An analogous definition is used in the EF region. Similarly, this quantity is also not a true impact parameter, but is referred to as the "nonbend impact parameter," IP(nonbend). Both of these quantities are required to be ≤ 20 cm. Also events in which there are hits or a track in the muon chambers on the opposite side in η and ϕ of a reconstructed muon with $|\eta| < 1.0$ are rejected.

2. *Track timing*

Another method used to discriminate against cosmic rays in the $\mu +$ jets analysis is to require the track to be coincident with the beam crossing time. One way of determining this is to allow the "time zero" of the hits (as a group) to vary and define the time for which the track χ^2 is minimized as the actual track time (ΔT_0). Since cosmic rays are random with respect to beam crossings, it is expected that a different overall ΔT_0 would give a better χ^2. Figure 5 shows the time difference ΔT_0 for muons from $W \rightarrow \mu\nu$ decays and cosmic rays. To select muons from the $p\bar{p}$ interaction we require $\Delta T_0 < 100$ ns.

3. *Minimum hit multiplicity*

Typically a muon track has hits on 7–10 PDT planes, depending on the region of the detector. We require at least five planes to have hits along the track. This cut reduces the backgrounds from random hits, especially for $|\eta| \geq 1.0$.

4. *Muon quality*

The muon reconstruction algorithm defines a muon track "quality," similar to that used in the level 2 trigger, which contains information about the number of muon modules with recorded hits, the impact parameters, and the hit residuals. If a track does not satisfy cuts on more than one of the above quantities, then it is determined to have insufficient "quality" and is rejected.

5. *Calorimeter confirmation*

A muon typically deposits 1–3 GeV energy as it passes through the calorimeter depending on its specific path length. We require a logical OR of two conditions. For events in which a CD track match has been found within $\Delta\eta \leq 0.45$ and $\Delta\phi \leq 0.45$ of the muon track, an energy deposit of at least 0.5 GeV is required in the calorimeter towers along the track plus its two nearest neighbor towers. For muons without a CD track match, at least 1.5 GeV is required. The latter cut allows for tracking inefficiencies in the region around $|\eta| \sim 1$ where the CD coverage is incomplete.

6. *Minimum magnetic path length*

Muons which pass through the thinner part of the iron toroid near $|\eta| \approx 0.9$ (and thus through a smaller amount

of magnetic field) have poorer momentum measurement and may be contaminated by a small background from punchthrough. To reject such muons, the minimum magnetic field integral traversed, $\int Bdl$, is required to be 1.83 Tm.

7. *Isolation*

For the analyses described in this paper, two different isolation algorithms are used.

(a) Isolation algorithm I: $e\mu$ and μ+jets channels. For the search in the $e\mu$ and μ+jets channels a muon is called isolated if it is well separated from any reconstructed jet and other calorimeter activity. For isolated muons we require a separation of $R(\mu-\text{jet}) > 0.5$ between the muon direction and the nearest jet axis for jets of $E_T > 8$ GeV. To check for diffuse jets which do not satisfy this energy threshold, we require in addition less than 4 (5) GeV of energy in an annular cone of $0.2 < \Delta R < 0.4$ around the muon direction for tracks in the CC (EC) calorimeter. The inner cone with $R < 0.2$ is excluded to allow for energy deposition from bremsstrahlung. Figure 6 shows the isolation variables for muons from $t\bar{t} \to \mu$+jets decays and the inclusive jet data.

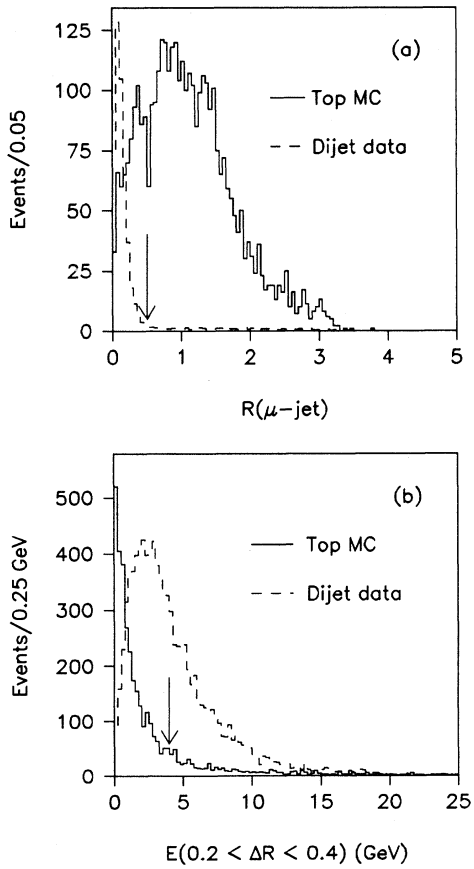

FIG. 6. Calorimeter isolation of muons in $t\bar{t} \to \mu\nu + X$ decays and inclusive jet data.

Isolation algorithm II: $\mu\mu$ channel. For the search in the $\mu\mu$ channel an alternative muon isolation definition was used to improve the $\mu\mu$ acceptance for $|\eta^\mu| < 1.0$. It is based on the transverse momentum of the muon with respect to the axis of the nearest reconstructed jet, p_T^{rel}:

$$p_T^{\text{rel}} = p^\mu \sin\vartheta \tag{9}$$

with

$$\cos\vartheta = \frac{(\vec{p}^\mu + \vec{E}^{\text{jet}}) \cdot \vec{p}^\mu}{|\vec{p}^\mu + \vec{E}^{\text{jet}}||\vec{p}^\mu|}\ , \tag{10}$$

where $\vec{E}^{\text{jet}}$ is defined along the axis of the jet. Figure 7 shows the p_T^{rel} distribution for a sample of μ + jet events ($p_T > 10$ GeV/c) which are dominated by $b\bar{b}$ and $c\bar{c}$ semileptonic decays [29]. For comparison we also show the distribution for muons in $t\bar{t} \to \mu\mu$ events in the same figure. A minimum p_T^{rel} cut of 5 GeV/c together with the requirement that a jet be reconstructed in the vicinity of the muon gives a rejection of $(92 \pm 1)\%$ for above backgrounds, while retaining about 75% efficiency for the muons from the W bosons in $t\bar{t}$ events, for a top quark mass of 160 GeV/c^2.

Muons from W decays in a $t\bar{t}$ event typically have high p_T and are isolated from any hadronic activity because of the large mass of the top quark. Muons produced in the decay of the lighter b and c quarks are softer and are close to hadronic activity from the quark fragmentation. The latter will be used to tag the presence of b jets in top quark candidate events. We therefore define two categories of muons.

Isolated high p_T muons. We require muons from W decays to be isolated and have $p_T > 15$ GeV/c. For analysis in the $e\mu$ channel this threshold is dropped to 12 GeV/c.

Tagging muons. The condition for a tagging muon is

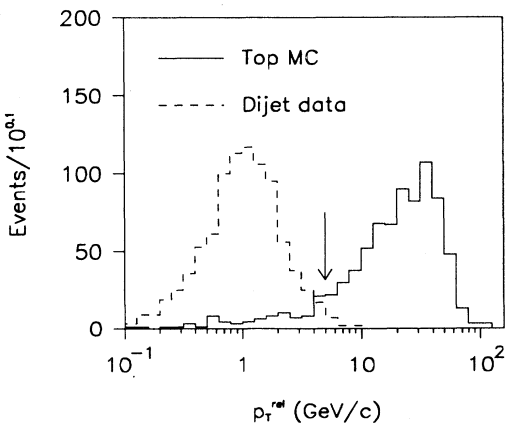

FIG. 7. p_T^{rel} for $t\bar{t} \to \mu\mu$ ($m_t = 160$ GeV/c^2) and μ + jet data ($p_T^\mu > 10$ GeV/c). The arrow indicates the value of the minimum p_T^{rel} cut made in the $t\bar{t} \to \mu\mu$ analysis.

TABLE IV. Definition of high -p_T and Tagging muon identification criteria.

Selection cut	High-p_T muon		tagging muon
	Loose	Tight	
IP (cm)	< 22	< 22	—
IP(bend) (cm)	—	< 20	—
IP(nonbend) (cm)	—	< 20	—
Hits/track opposite	Yes	Yes	No
CD/cal conf	Yes	Yes	Yes
$\int Bdl$ (Tm)	> 1.83	> 1.83	—
ΔT_0 (ns)	—	< 100	—

the complement of that for isolated high p_T muons. A muon is a tagging muon if it is not isolated and has $p_T > 4$ GeV/c. We also call an isolated muon a tagging muon if its p_T is below 15 GeV/c for μ + jets + μ tag or below 12 GeV/c for e + jets + μ-tag analysis.

Table IV lists the further cuts used in the two classifications of muons.

C. Jets

The D0 jet finding algorithm defines a jet by summing the E_T in a cone of radius $R = \sqrt{\Delta\eta^2 + \Delta\phi^2}$. The algorithm is similar to that used by the UA1 and CDF Collaborations [30,31]. The jet cone size was chosen to be $R = 0.5$. The choice of jet cone size was determined by maximizing the efficiency for $t\bar{t}$ events with 140 GeV/c^2 top quark mass in $e, \mu + \geq 4$ jets final states.

Beginning with the highest E_T tower, preclusters are formed of contiguous cells out to a radius of about $R = 0.3$. The preclusters are used to reduce the number of towers considered as possible starting points for jet formation, and to reduce the processing time. Only towers with $E_T > 1$ GeV are included in preclusters. These preclusters become the starting point for jet finding and the precluster center is used as the initial cone center. A new E_T weighted center is then formed using E_T of all towers within a radius $R \leq 0.5$ of the center, and the process is repeated until the jet is stable. A jet must have $E_T > 8$ GeV. If two jets share energy, they are combined or split, based on the fraction of energy shared relative to the E_T of the lower E_T jet. If the shared fraction exceeds 50%, the jets are combined.

The jet energy resolution is extracted from the asymmetry variable A computed for dijet events:

$$A = \frac{E_{T_1} - E_{T_2}}{E_{T_1} + E_{T_2}}, \tag{11}$$

where $E_{T_{1,2}}$ denotes the E_T of the two jets in the event. The asymmetry variable has a rms width that may be written as

$$(\sigma_A)^2 = \left(\left|\frac{\partial A}{\partial E_{T_1}}\right| \sigma_{E_{T_1}}\right)^2 + \left(\left|\frac{\partial A}{\partial E_{T_2}}\right| \sigma_{E_{T_2}}\right)^2. \tag{12}$$

If we assume $E_{T_1} = E_{T_2} \equiv E_T$ and $\sigma_{E_{T_1}} = \sigma_{E_{T_2}} \equiv \sigma_{E_T}$, the jet resolution can be written as

$$\left(\frac{\sigma_{E_T}}{E_T}\right) = \sqrt{2}\,\sigma_A. \tag{13}$$

We use corrected jet energies (see Sec. IV D) to compute the asymmetry, from which the resolution is determined as a function of the average corrected energy of the two jets. A series of standard cuts are introduced as a means of selecting a clean dijet sample for this study. However, jet resolution can also be extracted from direct photon + jet events by balancing the transverse energy in the event. This method gives reliable values at low transverse energies and hence is a good test of the resolutions obtained from dijet data.

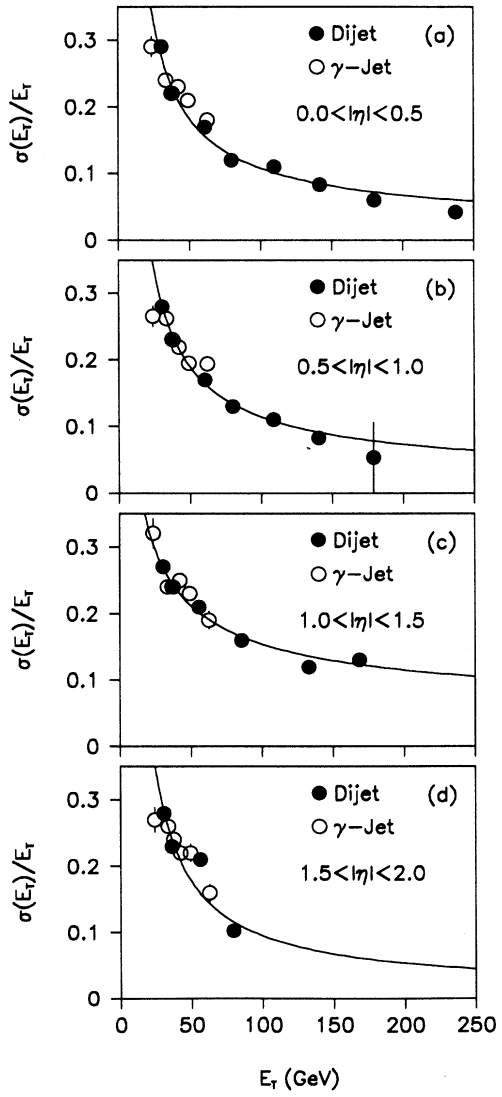

FIG. 8. Jet energy resolution as a function of the average corrected jet E_T as computed from dijet events and photon jet events in four pseudorapidity regions. Fits to the resolution function in these η regions are also shown.

TABLE V. Jet energy resolution fit parameters for each of the calorimeter regions.

η region	Noise term (N)	Sampling term (S)	Constant term (C)
$\lvert\eta\rvert < 0.5$	7.07 ± 0.09	0.81 ± 0.016	0.0 ± 0.005
$0.5 < \lvert\eta\rvert < 1.0$	6.92 ± 0.12	0.91 ± 0.019	0.0 ± 0.01
$1.0 < \lvert\eta\rvert < 1.5$	0.0 ± 1.4	1.45 ± 0.016	0.052 ± 0.006
$1.5 < \lvert\eta\rvert < 2.0$	8.15 ± 0.21	0.48 ± 0.07	0.0 ± 0.014
$2.0 < \lvert\eta\rvert < 3.0$	3.15 ± 2.5	1.64 ± 0.13	0.012 ± 0.58

We obtain a global fit to the energy resolutions determined from both dijet balance and photon jet balance in all the different η regions to the functional form

$$\left(\frac{\sigma_E}{E}\right)^2 = \left(\frac{N}{E}\right)^2 + \left(\frac{S}{\sqrt{E}}\right)^2 + C^2, \tag{14}$$

where N, S, and C are the noise, sampling, and constant terms, respectively. The results of the fit are given in Table V while Fig. 8 shows the data, and the fitted resolution function, in each of the calorimeter η regions.

D. Energy scale corrections

In order to put the measured energies of the physics objects of interest in both the data and the Monte Carlo events on an equal footing, we apply a series of energy corrections to electrons and jets.

The electromagnetic (EM) section sets the absolute energy scale for the D0 calorimeter. The EM energy scale is established by setting the invariant mass peak reconstructed from dielectron events in the appropriate mass region equal to the Z mass as measured by the LEP experiments [17]. Requiring both electrons in such events to be in the same cryostat, we obtain an independent absolute scale factor for each cryostat [32], which we apply to isolated electrons and photons (see Sec. IV A). We have used low mass resonances ($\pi^0 \to \gamma\gamma$, $J/\psi \to ee$) to check the calibration at different energies. Details of the EM energy calibration procedure can be found in [32].

There are several effects which contribute to the jet energy response: nonuniformities in the calorimeter, nonlinearities in the calorimeter response to hadrons, noise due to the radioactivity of uranium, and energy from the products of the soft interaction of spectator partons within the proton and antiproton (underlying event). These effects have been estimated using collider data, Monte Carlo simulations, and test beam data.

We use a variant of the method described in [31] to measure the cumulative response of the calorimeter to the fragmentation products associated with a jet. This method uses events with an isolated EM cluster due to a photon or a jet which fragmented mostly into neutral mesons, and at least one more hadronic jet. We attribute any energy imbalance along the direction of the photon in the transverse plane to the mismeasurement of the hadronic jet. In this way we measure the response of the calorimeter to the hadronic jet relative to the known response to the EM cluster.

The fragmentation products from final state partons falling within the jet cone produce wide showers in the calorimeter, causing some of the energy to fall outside of the cone. To measure this out-of-cone fraction, we have substituted single-particle test-beam showers for fragmentation products in the Monte Carlo event generators ISAJET [33] and HERWIG [34]. We correct only for the energy deposited outside of the jet cone due to showering, not for any particles landing out of cone due to fragmentation or radiation.

Having obtained the corrections described above for jets in the central calorimeter, we determine the variation of the jet energy scale with η and with the fraction of energy in the EM calorimeter by using dijet events. We determine these variations by balancing one jet in the forward region or a jet of varying EM fraction with an average jet in the central calorimeter.

Energy from the underlying event within the jet cone is included in the jet energy. The energy flow from the underlying event is assumed to be independent of the hard scatter that gives rise to the jets we observe [35]. We estimate this energy deposition by measuring the energy density in minimum bias events and then subtracting it from the jet energy. This also compensates for the biases in the energy measurement due to radioactive decays of the uranium.

The cumulative correction from all of these effects is shown in Fig. 9 and is typically 25% for central jets above 20 GeV in E_T. The correction generally increases with η as out-of-cone losses increase, while it decreases at the very lowest jet E_T due to the 8 GeV jet reconstruction E_T threshold. The dashed curves in Fig. 9 represent the error band on the jet energy scale corrections.

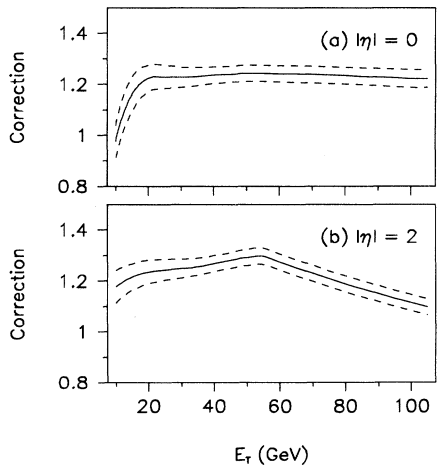

FIG. 9. Energy scale correction for jets as a function of jet energy in the central region ($|\eta| = 0.0$) and in the forward region ($|\eta| = 2.0$). Results are given for $R = 0.5$ cone jets. The dashed curves represent the error band.

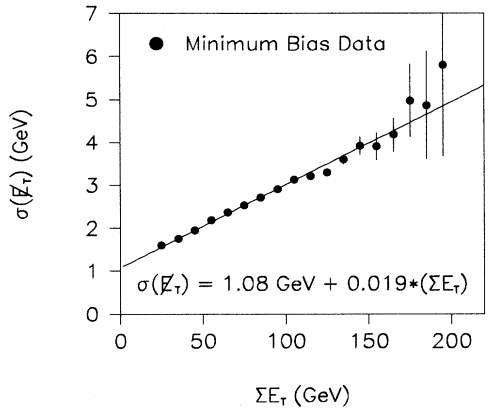

FIG. 10. Uncorrected $\not\!\!E_{Tx}^{\rm cal}$ distribution for minimum bias data. The line represents a fit to the data points.

E. Missing E_T ($\not\!\!E_T$)

We calculate the missing transverse energy deposited in the calorimeter $\not\!\!E_T^{\rm cal}$ to be

$$\not\!\!E_T^{\rm cal} = \sqrt{\not\!\!E_{Tx}^{\rm cal\,2} + \not\!\!E_{Ty}^{\rm cal\,2}} \ , \tag{15}$$

where

$$\not\!\!E_{Tx}^{\rm cal} = -\sum_i E_i \sin(\theta_i)\cos(\phi_i) - \sum_j \Delta E_x^j \ , \tag{16}$$

$$\not\!\!E_{Ty}^{\rm cal} = -\sum_i E_i \sin(\theta_i)\sin(\phi_i) - \sum_j \Delta E_y^j \ . \tag{17}$$

The first sum is over all cells in the calorimeter and ICD and the second sum is over the corrections in E_T applied to all electrons and jets in the event. In order to obtain the best energy resolution, we use the ΔE_T^j for jets obtained by reconstructing the event with $R = 0.7$ cone jets. This quantity can be used to estimate the transverse energy of neutrinos in events without muons because they do not interact in the detector. Given the hermeticity of the detector and its good energy resolution, we obtain very good $\not\!\!E_T^{\rm cal}$ resolution as shown in Fig. 10. The missing transverse energy ($\not\!\!E_T$) resolution of the calorimeter is important for the detection of top quark decays, which may contain several neutrinos. In the presence of muons, we subtract the transverse momentum of the muon from $\not\!\!E_T^{\rm cal}$ in order to estimate the total missing E_T:

$$\not\!\!E_{Tx} = \not\!\!E_{Tx}^{\rm cal} - \sum_i p_x^{\mu_i} \ , \tag{18}$$

$$\not\!\!E_{Ty} = \not\!\!E_{Ty}^{\rm cal} - \sum_i p_y^{\mu_i} \ . \tag{19}$$

V. EVENT SIMULATION

Event simulation plays an important role in the attempt to identify a $t\bar{t}$ signal in the presence of significant backgrounds. A reasonable description of the production and decay of $t\bar{t}$ events is needed to calculate detector acceptances and develop methods to identify the events. Whenever possible the backgrounds are estimated using the observed data but sometimes we need to resort to Monte Carlo simulation guided by theoretical expectations. The primary Monte Carlo program used for acceptances and backgrounds is ISAJET but for the $W+$ jets final state the output from VECBOS [36], a parton level Monte Carlo event, is used as input to ISAJET. The details are given in Secs. V A and V B.

A. Top production and decay

Events were generated for top quark masses between 100 and 200 GeV/c^2 for the reaction $p\bar{p} \to t\bar{t} + X$ using the ISAJET, HERWIG, and PYTHIA [37] Monte Carlo programs. These programs simulate $t\bar{t}$ production starting from leading order processes and simulate higher order corrections via final state and initial state radiation using leading log approximations for QCD evolution. The top quarks then decay to a W boson and a b quark. The W boson and the top quark decays have V-A matrix elements as do the semileptonic decays of the B mesons or baryons. In addition the quarks from W decays or the b quarks may radiate gluons before hadronization occurs. The basic underlying assumptions are the same in all three programs but they differ in the detailed implemen-

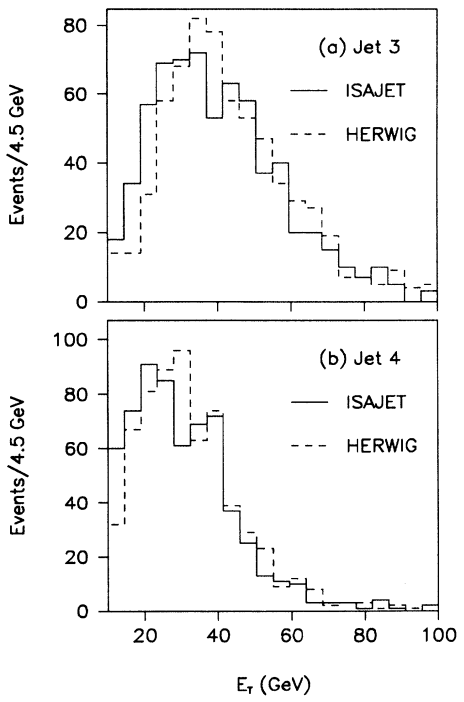

FIG. 11. E_T distributions for the (a) third jet and (b) fourth jet for ISAJET (solid), and for HERWIG (dashed), for 140 GeV/c^2 top mass.

tation. The generated events were run through DOGEANT [38], a trigger simulator and the D0 reconstruction program.

The differences in the acceptances calculated with the various Monte Carlo programs are small (of the order of 10–15%) and are incorporated as systematic errors. As an illustration, we show in Figs. 11 and 12 the E_T distributions of the third and fourth jets (ordered in E_T), aplanarity ($\mathcal{A}$) and scalar transverse energy (H_T) for events with one isolated electron and four or more jets with a top mass of 140 GeV/c^2 generated using the ISAJET and HERWIG Monte Carlo programs. $\mathcal{A}$ and H_T are global quantities used to separate $t\bar{t}$ from W + jets events and are defined in Sec. VII. It is apparent that for these variables the differences between HERWIG and ISAJET are small.

B. W+ jets

The VECBOS Monte Carlo program was used to generate samples of W + jets events up to fourth order in α_s at the parton level. VECBOS offers leading order parton-level calculations using the tree-level exact matrix elements for (W or Z)+n jets processes for $1 \leq n \leq 4$. Events have to be generated specifying a value of n, so each order must be generated separately. The jets refer to QCD partons and the calculations are carried out at the order α_s^n based solely on the formalisms of perturbative QCD (PQCD). Its accuracy is thus determined by the validity of the assumptions of PQCD. Therefore caution has to be exercised in defining and limiting the generation to the part of phase space where those assumptions hold reasonably well. This is done by setting minimum thresholds for the E_T's of the jets away from thresholds used in analysis and picking minimum separations between the jets so as to remain safely away from the regions of soft and small angle radiation where PQCD is known to yield divergent results. For the analyses presented in this paper we required $E_T > 10$ GeV for all the final state partons, $\Delta R > 0.5$ for every pair of jets, the CTEQ1M option for structure functions [39], and $\langle Q^2 \rangle = M_W^2$ for the dynamical scale.

The events generated by the VECBOS Monte Carlo program represent final state partons. In order to simulate the detector response to these events the particle fragmentation of these final states had to be simulated and the effects of the underlying ("spectator") processes included. The results from VECBOS were therefore run through a modified version of ISAJET to hadronize the partons. As VECBOS carries no information about the flavor of the final partons the assumption was made that

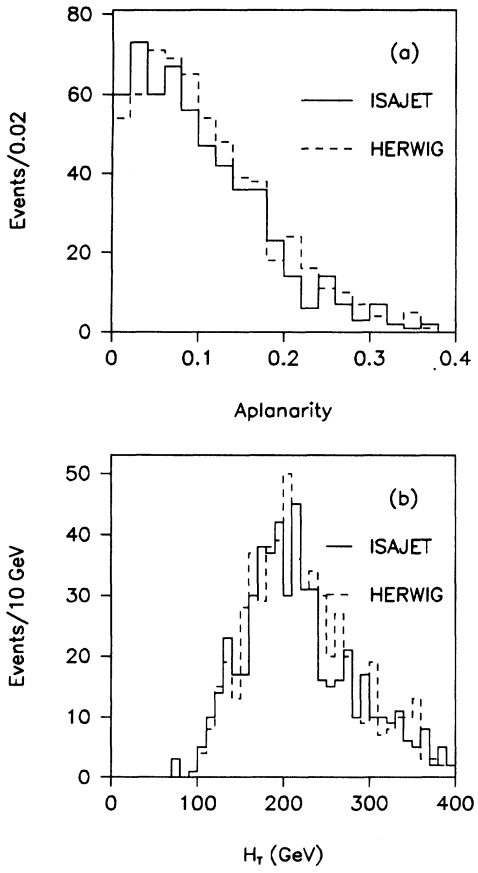

FIG. 12. (a) $\mathcal{A}$ and (b) H_T distributions for $t\bar{t}$ events with four or more jets from ISAJET (solid), and from HERWIG (dashed), for 140 GeV/c^2 top mass.

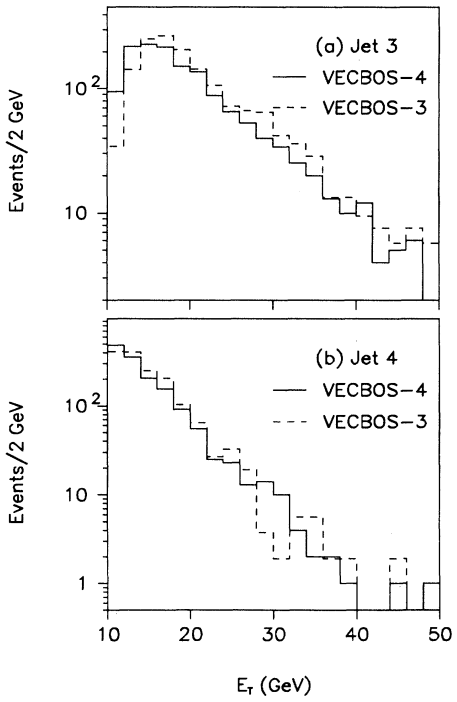

FIG. 13. E_T distributions for (a) third and (b) fourth jet in events with ≥ 4 jets starting from VECBOS with 3 jets (dashed lines) and from VECBOS with 4 jets (solid lines).

they are all gluons. These events were then run through DOGEANT to simulate in detail the detector response and then through the D0 reconstruction program.

Because VECBOS only generates events up to fourth order in α_s, ISAJET was also used to get an approximate representation of higher-order events (i.e., five or more jets) starting from fourth order. To test how well ISAJET simulates higher-order processes, we generated $W+3$ jets and $W+4$ jets events with VECBOS, fragmented both samples with ISAJET and compared the results. In Fig. 13 we show the E_T distributions of the third and fourth jets (ordered in E_T) from VECBOS $W+3$ jets and VECBOS $W+4$ jets events after they have been through ISAJET fragmentation, detector simulation, and reconstruction. We required at least four jets to be reconstructed with $E_T > 10$ GeV. It shows that ISAJET reproduces the next higher-order effect reasonably well.

VECBOS calculations are based only on tree-level diagrams (leading order) which can result in significant errors in the prediction of cross sections as the number of jets increases. We therefore avoid using the cross sections predicted by VECBOS by normalizing with respect to data (see Sec. VII D) which enables us to estimate the cross sections with smaller errors. Note, even though the number of predicted events in Table XXII and Fig. 27 (see Sec. VII D) are not normalized to the number of observed events, the deviations with respect to the data are well within the statistical errors. We do rely on the Monte Carlo program (with the corrections arising from higher-order effects partially implemented by ISAJET) to study the kinematics of the events.

VI. ANALYSIS OF DILEPTON EVENTS

The search for $t\bar{t}$ events in the dilepton decay modes concentrates on the process $t\bar{t} \rightarrow W^+W^-b\bar{b}$ in which the two W bosons decay leptonically into either $e\nu$ or $\mu\nu$ final states. The $\tau\nu$ final states, where τ decays hadronically, are excluded from the dilepton analyses because of the difficulty in reliably reconstructing the hadronic τ decays. This leaves three final states $ee+X$ (ee channel), $e\mu+X$ ($e\mu$ channel), and $\mu\mu+X$ ($\mu\mu$ channel) each of which contains two isolated, high p_T leptons together with large $\not\!\!E_T$ and two or more hadronic jets. This defines the starting point for the analyses described in the following section.

In the case of the ee and $e\mu$ channels, two separate analyses were performed. One, hereafter referred to as analysis I, has been optimized for top quark mass values down to the published limit at that time [8], and the other, analysis II, has been optimized for a low background search for top quark masses above 120 GeV/c^2. For the $\mu\mu$ channel the analysis was restricted to the higher top quark mass region only.

The selection cuts were chosen to maximize the signal-to-background ratio, while simultaneously keeping an appreciable efficiency for observing top quarks in the dilepton channels. Whenever possible we used collider data to estimate the effects of detector resolution and bias and we used Monte Carlo samples only in cases in which suitable data sets were not available.

A. The ee channel

1. Event selection

If both W bosons decay to electron + neutrino, then $t\bar{t}$ decays result in a final state containing two isolated high p_T electrons, two neutrinos which give rise to $\not\!\!E_T$, and jets from the fragmentation of the two b quarks, as well as initial and final state radiation. We shall refer to this decay channel as the ee channel.

We trigger on these events with the logical OR of the following four trigger conditions: ELE-JET, ELE-HIGH, ELE-MAX, and ELE-2-HIGH (see Table II). The combined trigger efficiency, obtained via trigger simulation studies on samples of Monte Carlo $t\bar{t}$ events processed through full detector simulation, varies between 76% and 94% for top quark masses between 80 and 180 GeV/c^2.

There are a number of background processes that can produce final states containing two electrons: $Z,\gamma^* \rightarrow e^+e^-;\tau^+(\rightarrow e^+\nu\nu)\tau^-(\rightarrow e^-\nu\nu)$ decays; $W^+W^- \rightarrow e^+\nu e^-\nu$ and $WZ \rightarrow e^+e^-X$ decays and semileptonic decays of $b\bar{b}$. We shall refer to these as physics backgrounds. Fake backgrounds are due to misidentification of jets and single particles as electrons [40].

We apply a number of selection criteria to separate the signal from these backgrounds.

Electron identification. We use two sets of electron identification criteria, loose and tight. These are defined in Table III which also lists the corresponding selection efficiencies. In both analyses (I and II) we require two electrons of which at least one must satisfy the tight electron identification cuts. The second electron is required to satisfy the looser criteria. For analysis I the emphasis was on high selection efficiency while for analysis II the cuts were chosen to minimize fake backgrounds, resulting in somewhat different definitions of tight and loose cuts for the two analyses. By requiring the electrons to be isolated we strongly suppress backgrounds from semileptonic b and c quark decays.

Transverse energy (E_T). Both electrons must have $E_T > 20$ GeV. By requiring two electrons above this kinematic threshold which also pass the electron identification and the detector acceptance cuts, we accept around $(22 \pm 5)\%$ of all $t\bar{t} \rightarrow ee$ decays for a top quark mass of 180 GeV/c^2. This cut significantly reduces backgrounds from Drell-Yan production of e^+e^- and $\tau^+\tau^-$ pairs, $Z \rightarrow \tau^+\tau^-$ decays, and fake backgrounds. After isolation and E_T cuts, backgrounds from semileptonic b and c quark decays have been reduced by more than a factor of 50 to a negligible level.

Dielectron invariant mass (M_{ee}). Production of e^+e^- pairs is dominated by $Z \rightarrow e^+e^-$ decays. They do not contain any high p_T neutrinos and can very effectively be rejected by excluding events with 79 GeV/$c^2 < M_{ee} <$ 103 GeV/c^2 and $\not\!\!E_T <$ 40 GeV. We retain events with $\not\!\!E_T >$ 40 GeV even if they lie in the Z mass region since we expect less than 2×10^{-4} of all Z decays to pass this

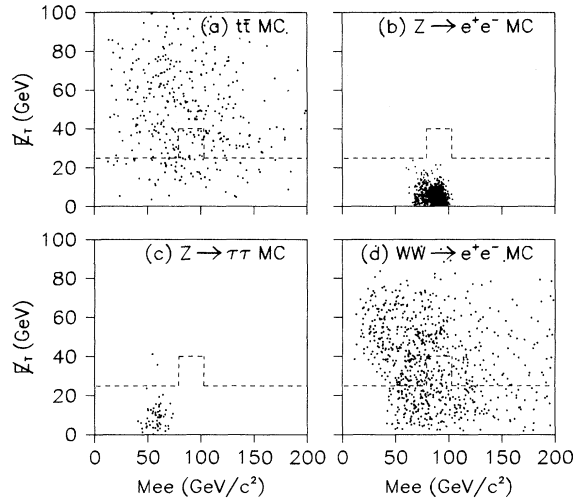

FIG. 14. $\not\!\!E_T$ vs M_{ee} for (a) $t\bar{t} \to ee+X$ ($m_t = 140$ GeV/c^2), (b) $Z \to ee$, (c) $Z \to \tau\tau$, and (d) $WW \to e\nu e\nu$ Monte Carlo samples corresponding to an integrated luminosity of 12.1 pb^{-1}, 47.7 pb^{-1}, 0.53 fb^{-1}, 21.2 fb^{-1}, respectively. Dashed line represents the cut (see text).

$\not\!\!E_T$ cut. This increases the acceptance for $t\bar{t}$ decays by about 15%.

Missing transverse energy ($\not\!\!E_T$). $Z \to \tau^+(\to e^+\nu\nu)\tau^-(\to e^-\nu\nu)$ decays and Drell-Yan processes produce e^+e^- pairs outside the Z mass region. Since they do not have high $\not\!\!E_T$ they can be heavily suppressed by requiring $\not\!\!E_T > 25$ GeV. Figure 14(a) illustrates the effect of the M_{ee} and the $\not\!\!E_T$ cuts on $t\bar{t}$ Monte Carlo events after the dielectron requirement. Figures 14(b)–14(d) show the effect on $Z \to e^+e^-$, $Z \to \tau^+\tau^-$, and $W^+W^- \to e^+\nu e^-\nu$, respectively.

Jet multiplicity and transverse energy. After the preceding cuts, $W^+W^- \to e^+\nu e^-\nu$ decays are the dominant background. The W pairs are typically produced with few or no associated jets, whereas $t\bar{t}$ decays are expected to have jets from the fragmentation of the two b quarks. To suppress the W^+W^- background we cut on the multiplicity and E_T of the reconstructed jets. For analysis I we require at least 1 jet with $E_T > 15$ GeV and for analysis II we require at least 2 jets with $E_T > 15$ GeV. We select jets in the fiducial region $|\eta| < 2.5$.

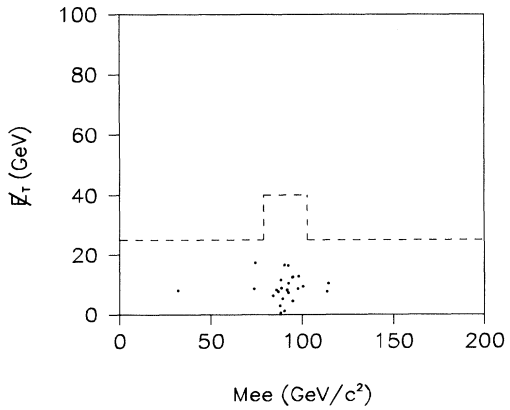

FIG. 15. $\not\!\!E_T$ vs M_{ee} for D0 data. The dashed line is the cut (see text).

TABLE VI. Analysis cuts for $t\bar{t} \to ee + X$ channel after trigger selection and cumulative effects on data for analysis I.

Analysis I cuts	Number of events in 13.5 pb^{-1}
1 tight I, 1 loose I electron	
$E_T > 20$ GeV, $\|\eta\| < 2.5$	940
$\not\!\!E_T > 40$ GeV if $79 < M_{ee} < 103$ GeV/c^2	149
$\not\!\!E_T > 25$ GeV	4
≥ 1 jet, $E_T > 15$ GeV, $\|\eta\| < 2.5$	1

A plot of $\not\!\!E_T$ versus M_{ee} for the data sample after requiring two electrons and two jets is shown in Fig. 15.

The number of events which pass our cuts for the two analyses are summarized in Tables VI and VII. In analysis I, one event passes all selection cuts. Some kinematic properties of this event are presented in the Appendix. It is rejected in analysis II because the second jet fails the $|\eta|$ requirement.

2. *Expected $t\bar{t}$ signal*

We expect to detect

$$N_{\text{pred}} = \int \mathcal{L}dt \times \sigma_{t\bar{t}} \times B_{ee} \times \epsilon_{\text{tot}} \tag{20}$$

$t\bar{t}$ decays, where $\int \mathcal{L}dt$ is the integrated luminosity of the data sample, $\sigma_{t\bar{t}}$ is the $t\bar{t}$ production cross section, B_{ee} is the branching ratio for the ee channel, ϵ_{tot} is the efficiency for $t\bar{t}$ decays in this channel.

The integrated luminosity [9] for the data sample is

$$\int \mathcal{L}dt = 13.5 \pm 1.6 \text{ pb}^{-1}. \tag{21}$$

TABLE VII. Analysis cuts for $t\bar{t} \to ee + X$ channel after trigger selection and cumulative effects on data for analysis II.

Analysis II cuts	Number of events in 13.5 pb^{-1}
1 tight II, 1 loose II electron	
$E_T > 20$ GeV, $\|\eta\| < 2.5$	739
$\not\!\!E_T > 40$ GeV if $79 < M_{ee} < 103$ GeV/c^2	111
$\not\!\!E_T > 25$ GeV	4
≥ 2 jets, $E_T > 15$ GeV, $\|\eta\| < 2.5$	0

TABLE VIII. Efficiency $\times$ B_{ee} and predicted event yields for $t\bar{t} \to ee + X$ for analyses I and II.

	Analysis I		Analysis II	
m_t (GeV/c^2)	$\epsilon_{\rm tot} \times B_{ee}$ (%)	$N_{\rm pred}$ for 13.5 pb^{-1}	$\epsilon_{\rm tot} \times B_{ee}$ (%)	$N_{\rm pred}$ for 13.5 pb^{-1}
90	0.16 ± 0.02	4.01 ± 0.76	–	–
100	0.20 ± 0.03	2.83 ± 0.54	–	–
120	0.26 ± 0.04	1.37 ± 0.26	0.14 ± 0.03	0.76 ± 0.12
140	0.28 ± 0.04	0.63 ± 0.12	0.18 ± 0.02	0.41 ± 0.07
160	0.29 ± 0.04	0.32 ± 0.06	0.20 ± 0.03	0.22 ± 0.04
180	–	–	0.21 ± 0.03	0.12 ± 0.02
200	–	–	0.30 ± 0.04	0.09 ± 0.02

TABLE IX. Physics and fake backgrounds to the $t\bar{t} \to ee + X$ searches.

Background	Event yield for 13.5 pb^{-1}	
	Analysis I	Analysis II
$Z \to ee$	0.03 ± 0.03	0.03 ± 0.03
$Z \to \tau\tau \to ee + X$	0.09 ± 0.04	0.05 ± 0.03
$W^+W^- \to ee + X$	0.07 ± 0.01	0.01 ± 0.01
$WZ \to ee + X$	$(2.5 \pm 1.0) \times 10^{-3}$	$(1.0 \pm 1.0) \times 10^{-3}$
$\gamma^* \to \tau\tau \to ee + X$	$(4.0 \pm 1.0) \times 10^{-3}$	$(1.5 \pm 1.0) \times 10^{-3}$
$b\bar{b}$, $c\bar{c} \to ee + X$	0.02 ± 0.01	0.01 ± 0.01
Fake backgrounds	0.32 ± 0.14	0.05 ± 0.03
Total:	0.54 ± 0.23	0.15 ± 0.11

We use the central value for $\sigma_{t\bar{t}}$ given by the approximate NNLO QCD calculation [21] and the standard model branching fraction of 1.23% for B_{ee}. The efficiency $\epsilon_{\rm tot}$ is the product of the trigger efficiency $\epsilon_{\rm trig}$, the efficiency of the selection cuts $\epsilon_{\rm sel}$ and the geometric acceptance A:

$$\epsilon_{\rm tot} = \epsilon_{\rm trig} \times \epsilon_{\rm sel} \times A. \quad (22)$$

Both efficiencies are functions of the top quark mass. We have studied them using samples of Monte Carlo events generated with the ISAJET and PYTHIA event generators and with full detector and trigger simulation.

The $t\bar{t}$ decays, in which one or both W bosons decay to τ, followed by $\tau \to e\nu\nu$, contribute an additional 0.47% to the total branching ratio for $t\bar{t}$ to final states containing an e^+e^- pair:

$$t\bar{t} \to \tau\tau + X \to ee + X \quad \text{and } t\bar{t} \to \tau e + X \to ee + X \ .$$

The electron p_T and $\not\!\!E_T$ spectra for these events are softer than for $t\bar{t}$ decays in which both W bosons decay directly to $e\nu$ and the increase in event yield after the selection cuts is very small (e.g., < 0.5 events for $m_t = 80$ GeV/c^2). In calculating the predicted event yield from $t\bar{t}$ decays we include these contributions.

The values of $\epsilon_{\rm tot} \times B_{ee}$ and $N_{\rm pred}$ are tabulated in Table VIII. Systematic uncertainties in $t\bar{t}$ simulation (8%), electron identification efficiency [3% (CC), 7% (EC)], event reconstruction (10%), and trigger simulation (5%) add in quadrature to give the systematic error quoted in the table.

3. Backgrounds

To evaluate the number of events expected from physics backgrounds we have determined the detection efficiency and acceptance with Monte Carlo event samples and used Eq. (20) with the known cross sections and branching fractions in the same way as for the $t\bar{t}$ signal yields. The cross sections used for various background processes can be obtained from [41]. The contributions estimated from the individual processes are listed in Table IX.

We use the data sample collected using the same triggers as for signal selection in order to estimate the number of events expected from fake backgrounds. These backgrounds arise when either one or both of the electrons in the event arise from misidentified jets. We select events which pass the $\not\!\!E_T$ cut and have at least one cluster which passes either the loose or tight electron identification cuts described in Table III. We also require the presence of at least two additional jets in the event. We then hypothesize that every jet with $E_T > 20$ GeV in this data sample can fluctuate and be misidentified as an electron and hence causing the event to be identified as a dielectron event. Therefore, we count the total number of jets ($N_{\rm jet}$) in the CC and EC regions in these events. By multiplying $N_{\rm jet}$ with the appropriate probability that a jet fakes the electron selection cuts, [P(jet $\to$ loose e(tight e))], we obtain an estimate of the number of events expected from fake backgrounds.

The probability that a jet passes the loose or tight electron selection cuts is measured using the multijet trigger data sample. In this sample the contribution from real electrons due to heavy quark decays and direct photon events with accidental track overlap is assumed to be small. The probability that a jet fakes an electron is defined as the number of jets passing the electron selection cuts divided by the total number of jets in the sample. We find that the probabilities that a jet passes the electron II selection cuts are

$$\begin{aligned} P(\text{jet} \to \text{loose } e) &= (2.5 \pm 1.2) \times 10^{-4} \text{ for CC and} \\ &\quad (3.3 \pm 2.0) \times 10^{-4} \text{ for EC,} \\ P(\text{jet} \to \text{tight } e) &= (0.8 \pm 0.4) \times 10^{-4} \text{ for CC and} \\ &\quad (2.0 \pm 1.0) \times 10^{-4} \text{ for EC.} \end{aligned} \quad (23)$$

The estimated number of fake background events is listed in Table IX.

4. Summary of ee channel

In the search for $t\bar{t}$ decays with two electrons in the final state, we find one event surviving all cuts in analysis

I, while no events are found in analysis II which was optimized for the high mass top quark search.

For analysis II, we estimate a background of 0.16 ± 0.07 events, which is a factor of three lower than in analysis I. The expected top quark event yields for $m_t > 130$ GeV/c^2 are very similar for the two analyses. The expected $t\bar{t}$ event yields corresponding to analysis II are 0.76 ± 0.12 events, 0.41 ± 0.07 events, 0.22 ± 0.04 events, 0.12 ± 0.02 events, 0.09 ± 0.02 events for $m_t = 120$, 140, 160, 180, and 200 GeV/c^2, respectively.

B. The $e\mu$ channel

1. *Event selection*

The signature of an event candidate in the $e\mu$ channel is the presence of two isolated leptons (μ,e) with large transverse momentum, large $\not\!\!E_T$, and one or more hadronic jets.

The triggers used for this channel are MU-ELE, MU-JET-MAX, and ELE-JET-MAX (see Table II). The latter trigger increases the acceptance by approximately 15%, owing primarily to the region $|\eta| < 1.0$ where the muon level 1 trigger coverage is incomplete because of the structural supports of the calorimeter. The combined trigger efficiency is $(90 \pm 7)\%$ and is dependent on the value of m_t.

The selection cuts and their cumulative effect on the data are summarized in Tables X and XI for analyses I and II, respectively [41]. In the following we discuss the motivations for each cut. Both analyses result in one event candidate with two leptons with very large transverse momentum, three hadronic jets, and a substantial $\not\!\!E_T$. The properties of this event are given in the Appendix.

Lepton transverse momentum (p_T, E_T). For analysis I, events satisfying the triggers were required to have at least one electron with $E_T > 15$ GeV and $|\eta| < 2.5$ and one muon with $p_T > 15$ GeV/c and $|\eta| < 1.7$. For the electron selection we use the loose electron definition described in Table III and for the muon selection we use the loose muon definition described in Table IV. We further require that the muon track be isolated (isolation algorithm I, see Sec. IV B). For analysis II the muon p_T cut was lowered to 12 GeV/c to improve the $t\bar{t}$ acceptance and minimize the dependence on the muon momentum. Requiring the leptons to be isolated reduces backgrounds from semileptonic $b\bar{b}$ and $c\bar{c}$ decays to a negligible level.

Missing transverse energy ($\not\!\!E_T$). To suppress background contributions from $b\bar{b}$ decays, QCD multijet fake background, and from $Z \to \tau(\to e\nu\nu)\tau(\to \mu\nu\nu)$ we require $\not\!\!E_T > 20$ GeV in analysis I and $\not\!\!E_T > 10$ GeV in analysis II. Lowering of the $\not\!\!E_T$ cut was necessary to gain acceptance for $t\bar{t} \to e\mu$ decays while putting little emphasis on the muon momentum measurement.

Transverse energy imbalance in calorimeter ($\not\!\!E_T^{\rm cal}$). To suppress backgrounds from the process $W(\to \mu\nu)$ +jets, where a photon radiated from the muon or a jet is misidentified as an electron due to an accidental track

TABLE X. Analysis cuts for the $t\bar{t} \to e\mu + X$ channel and cumulative effects on data for analysis I.

Analysis I cuts	No. of events in 13.5 pb^{-1}
1 loose isolated μ, $p_T > 15$ GeV/c, $\|\eta\| < 1.7$	
1 loose I electron, $E_T > 15$ GeV, $\|\eta\| < 2.5$	27
$\not\!\!E_T > 20$ GeV	15
$\not\!\!E_T^{\rm cal} > 20$ GeV	8
$\Delta\mathcal{R}^{e\mu} > 0.25$	5
≥ 1 jet, $E_T > 15$ GeV, $\|\eta\| < 2.5$	1

TABLE XI. Analysis cuts for the $t\bar{t} \to e\mu + X$ channel and cumulative effects on data for analysis II.

Analysis II cuts	No. of events in 13.5 pb^{-1}
1 loose isolated μ, $p_T > 12$ GeV/c, $\|\eta\| < 1.7$	
1 Loose II electron, $E_T > 15$ GeV, $\|\eta\| < 2.5$	12
$\not\!\!E_T > 10$ GeV	8
$\not\!\!E_T^{\rm cal} > 20$ GeV	8
$\Delta\mathcal{R}^{e\mu} > 0.25$	7
≥ 2 jets, $E_T > 15$ GeV, $\|\eta\| < 2.5$	1

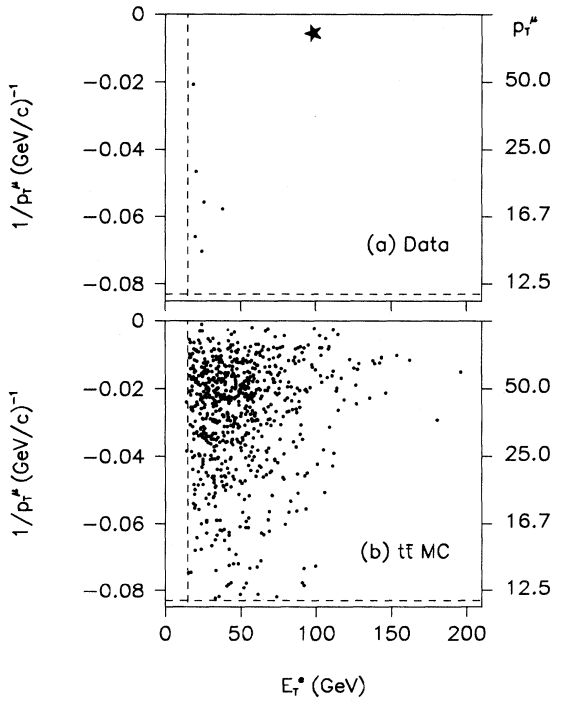

FIG. 16. $1/p_T^\mu$ vs E_T^e for (a) D0 data and (b) $t\bar{t} \to e\mu$ Monte Carlo events ($m_t = 170$ GeV/c^2, $\int \mathcal{L}dt = 21$ fb^{-1}). The dashed lines represent the selection cuts on $1/p_T^\mu$ and E_T^e.

overlap, we require $\not\!\!E_T^{\rm cal} > 20$ GeV. $\not\!\!E_T^{\rm cal}$ is a measure of the transverse momentum of the W in this process. Since W bosons are typically produced with small transverse momentum, this cut substantially decreases this background while having little effect on the acceptance for $t\bar{t}$ decays.

Muon-electron separation ($\Delta R^{e\mu}$). An energetic photon radiated by a muon from $W \to \mu\nu$ decays may be misidentified as an electron. These events are characterized by small $e\mu$ invariant mass (typically $M_{e\mu} < 2$ GeV/c^2) and small $e\mu$ separation ($\Delta\mathcal{R}^{e\mu} < 0.2$). Since this is an extremely unlikely topology for a $t\bar{t}$ decay we require $\Delta R^{e\mu} > 0.25$.

In Fig. 16(a), we plot the inverse p_T of the muon versus the E_T of the electron for the events remaining at this stage in our analysis. The corresponding plot for $t\bar{t} \to e\mu$ Monte Carlo events is shown in Fig. 16(b). The event denoted by a star in Fig. 16(a) survives all selection cuts.

Jet multiplicity and transverse energy. As in the ee channel, the remaining background is dominated by diboson decays and Z bosons with large transverse momentum which decay to $e\mu$ final states $Z \to \tau\tau \to (e\nu\nu)(\mu\nu\nu)$. To suppress these we require the presence of at least one jet with $E_T > 15$ GeV (analysis I) and at least two jets with $E_T > 15$ GeV for analysis II. We count all jets within $|\eta| < 2.5$.

2. Expected $t\bar{t}$ signal

The predicted number of $t\bar{t} \to e\mu + X$ events passing the selection cuts, $N_{\rm pred}$, has been evaluated using Eq. (20) in the same way as for the ee channel. The only differences are in the value of the branching fraction, $B_{e\mu} = 2.47\%$, and the efficiencies. The efficiency term in Eq. (20) has been evaluated separately for the two analyses using Monte Carlo programs, generated with the ISAJET and PYTHIA event generators in combination with a full simulation of the detector and trigger systems.

As in the ee channel, $t\bar{t}$ decays which result in $e\mu$ final states via a $W \to \tau\nu \to e\nu\nu$ or $W \to \tau\nu \to \mu\nu\nu$ decay contribute to the effective branching ratio. The contribution is 0.95% of the $e\mu$ branching fraction. In computing the predicted event yield from $t\bar{t}$ decays we include these contributions.

The resulting values of $\epsilon_{\rm tot} \times B_{e\mu}$ and $N_{\rm pred}$ are listed in Table XII. For $N_{\rm pred}$ we have used the central value of $\sigma_{t\bar{t}}$ from Ref. [21]. The errors are dominated by the 15% systematic error which is the sum in quadrature of the following contributions: event simulation (8%), modeling of the detector and event reconstruction (10%), trigger response (5%), and uncertainties in electron and muon identification [4% (e), 5% (μ)].

3. Backgrounds

The treatment of the experimental background in the $e\mu$ channel is analogous to that in the ee channel. Physics backgrounds have been estimated using Monte Carlo simulations. The processes considered and their estimated contributions to the background are listed in Table XIII.

To estimate the background contribution arising from particle misidentification we have considered the cases in which the electron is the result of misidentification and those in which the muon is from a π/K decay, cosmic ray, or punchthrough.

The probability for jets faking an electron is given in the section on the ee channel. Hadronic one-prong or three-prong τ decays also give rise to narrow jets. We studied the probability for hadronic τ decays being misidentified as electrons using a sample of $Z \to \tau\tau$ Monte Carlo events, generated with the ISAJET event generator and a full detector simulation using DØGEANT. The fake probability for the loose electron identification cuts is 0.010 ± 0.003. Finally, electrons can be faked by bremsstrahlung from muons. The photon energy spectrum for these events peaks towards very small values of E_T^γ and only the events from the hard tail of the spectrum satisfy the electron E_T cut of 15 GeV. These are further suppressed by the $\Delta\mathcal{R}^{e\mu}$ cut. We calculated the probability for a photon to pass all the electron cuts using the Monte Carlo method of Baur and Zeppenfeld [42] to be $(2.0 \pm 0.5) \times 10^{-3}$ per muon.

Muons can be faked by energetic hadrons which punch through the calorimeter. Because of the large number of interaction lengths of material provided by the DØ calorimeters and muon toroids, this background is negligible. Studies using a detailed Monte Carlo shower simulation [43] and large p_T muon data show no evidence for punchthrough background which satisfies the muon identification criteria used in the top quark search. We estimate the background from this source to be $< 10^{-4}$

TABLE XII. Efficiency $\times$ $B_{e\mu}$ and predicted event yields for $t\bar{t} \to e\mu + X$ in analyses I and II.

m_t (GeV/c^2)	Analysis I		Analysis II	
	$\epsilon_{\rm tot} \times B_{e\mu}$ (%)	$N_{\rm pred}$ for 13.5 pb^{-1}	$\epsilon_{\rm tot} \times B_{e\mu}$ (%)	$N_{\rm pred}$ for 13.5 pb^{-1}
90	0.39 ± 0.10	9.40 ± 2.57	–	–
100	0.46 ± 0.11	6.34 ± 1.76	–	–
120	0.49 ± 0.12	2.56 ± 0.71	0.27 ± 0.04	1.4 ± 0.30
140	0.54 ± 0.13	1.23 ± 0.33	0.31 ± 0.04	0.72 ± 0.14
160	0.56 ± 0.14	0.62 ± 0.17	0.36 ± 0.05	0.40 ± 0.08
180	–	–	0.39 ± 0.05	0.23 ± 0.04
200	–	–	0.40 ± 0.05	0.12 ± 0.02

TABLE XIII. Physics backgrounds to the two $t\bar{t} \to e\mu + X$ searches.

Background	Event yield for 13.5 pb^{-1}	
	Analysis I	Analysis II
$Z \to \tau\tau \to e\mu + X$	0.32 ± 0.07	0.13 ± 0.03
$W^+W^- \to e\mu + X$	0.19 ± 0.04	$(1.8 \pm 0.4) \times 10^{-2}$
$WZ \to e\mu + X$	$(2.4 \pm 0.5) \times 10^{-2}$	$(6.2 \pm 1.2) \times 10^{-3}$
$\gamma^* \to \tau\tau \to e\mu + X$	$(5.8 \pm 1.0) \times 10^{-3}$	$(4.3 \pm 0.9) \times 10^{-3}$
$b\bar{b}$, $c\bar{c} \to e\mu + X$	$(0.0 \pm 2.7) \times 10^{-2}$	$(0.0 \pm 2.7) \times 10^{-2}$
W + jets $\to e\mu + X$	$(0.0 \pm 1.9) \times 10^{-2}$	$(0.0 \pm 1.5) \times 10^{-2}$
Total:	0.54 ± 0.16	0.16 ± 0.08

TABLE XIV. Misidentification backgrounds to the two $t\bar{t} \to e\mu + X$ searches. $X(e)$ and $Y(\mu)$ represent misidentified electrons and muons, respectively.

Background	Event yield for 13.5 pb^{-1}	
	Analysis I	Analysis II
W + jets $\to \mu$ + jets + $X(e)$	0.36 ± 0.22	0.05 ± 0.04
W + jets $\to \mu$ +(brem)+jets	$(2.1 \pm 0.4) \times 10^{-2}$	$(6.0 \pm 1.3) \times 10^{-3}$
W + jets $\to e$ + jets + $Y(\mu)$	$(4.1 \pm 5.2) \times 10^{-3}$	$(1.0 \pm 1.4) \times 10^{-3}$
Z + jets $\to \tau\tau \to \mu$ + jets + $X(e)$	0.19 ± 0.04	0.05 ± 0.02
Z + jets $\to \mu\mu$ + jets + $X(e)$	$(1.3 \pm 0.4) \times 10^{-2}$	$(1.6 \pm 0.9) \times 10^{-3}$
$b\bar{b}$, $c\bar{c} \to \mu + X(e)$+jets	$(1.2 \pm 0.7) \times 10^{-3}$	$(7.9 \pm 5.0) \times 10^{-4}$
Total:	0.59 ± 0.27	0.11 ± 0.06

events. Trigger and selection criteria suppress the cosmic ray background so that it is negligible for muons with $p_T > 15$ GeV/c. We also consider muons from π/K decays under this category of backgrounds since they have a long decay length ($c\tau \approx 4 - 8$ m). Detailed calculations of the decay background result in a value of $(1.2 \pm 0.3) \times 10^{-6}$ for the probability per jet of detecting an isolated muon with $p_T > 12$ GeV/c originating from π/K decays [44].

The channels considered as possible sources of background are listed in Table XIV. We adopt the notation $X(e)$ and $Y(\mu)$ to denote a misidentified electron or muon, respectively.

Combining the results from the physics and misidentification backgrounds (Tables XIII and XIV) we calculate a total background of 1.13 ± 0.44 events for analysis I and 0.27 ± 0.14 events for analysis II.

4. Summary of $e\mu$ channel

In the top quark search with one electron and one isolated muon in the final state, we find one event surviving all cuts in analyses I and II. All the kinematical quantities of this event are far from the cut boundaries. The expected top quark yields for this channel vary with the top quark mass and for the cuts used for analysis II they are 1.4 ± 0.3 events, 0.72 ± 0.14 events, 0.40 ± 0.08 events, 0.23 ± 0.04 events, 0.12 ± 0.02 events for $m_t =$ 120, 140, 160, 180, and 200 GeV/c^2, respectively.

Note that the background estimates for analysis II are more than a factor of 4 smaller than those obtained in analysis I while the acceptance for the $t\bar{t}$ signal for $m_t >$ 130 GeV/c^2 is similar for the two analyses.

C. The $\mu\mu$ channel

The search for $t\bar{t}$ production in the $\mu\mu$ channel was performed on a subsample of the data. The integrated luminosity used in this analysis is

$$\int \mathcal{L}dt = 9.8 \pm 1.2 \text{ pb}^{-1}. \quad (24)$$

1. Event selection

The signature of an event candidate in the $\mu\mu$ channel is the presence of two isolated muons with large transverse momentum and one or more hadronic jets.

The trigger used for this analysis is MU-JET-MAX (see Table II) which requires a muon with $p_T > 14$ GeV/c and $|\eta| < 1.7$ and a jet with $E_T > 15$ GeV. The trigger efficiency varies between 85% and 87% for 100 GeV/c^2 < $m_t < 180$ GeV/c^2.

The principal background is the decay of Z bosons into a muon pair. Since the dimuon invariant mass distribution for $Z \to \mu\mu$ decays has a full width at half maximum of about 30 GeV/c^2, a cut on this quantity is ineffective. The analysis instead exploits the topological differences between $Z \to \mu\mu$ and $t\bar{t} \to \mu\mu + X$ decays. In Table XV we list the selection cuts and their cumulative effect on the data [45]. No events pass all the selection cuts.

Transverse momentum (p_T). Events satisfying the MU-JET-MAX trigger were required to have two muons with $p_T > 15$ GeV/c. The muons were required to be within $|\eta| < 1.1$ due to trigger losses at level 1 for muon chambers covering $|\eta| > 1.1$. We require that both muons satisfy all the tight muon identification cuts described in Table IV except for the integrated magnetic field and floating T_0 requirements. The p_T cut reduces backgrounds from semileptonic decays of b and c quarks.

Dimuon invariant mass ($M_{\mu\mu}$). To exclude $\psi \to \mu\mu$

TABLE XV. Comparison of the cumulative effect of the $t\bar{t} \to \mu\mu + X$ analysis cuts after trigger selection.

Analysis cuts	Number of events in 9.8 pb^{-1}
2 muons, $p_T > 15$ GeV/c, $\|\eta\| < 1.1$	
1 jet, $E_T > 15$ GeV, $\|\eta\| < 2.5$	39
$M_{\mu\mu} > 10$ GeV/c^2	28
$p_T^{\text{rel}} > 5$ GeV/c	13
$\Delta\phi(\vec{p}_T^{\mu_1}, \vec{p}_T^{\mu_2}) < 165°$ if $\|\eta^{\mu 1} + \eta^{\mu 2}\| < 0.3$	13
$\Delta\phi(\not\!\!E_T, \vec{p}_T^{\mu_1}) < 165°(175°)$	10
$\Delta\phi(\not\!\!E_T^{\text{cal}}, \vec{p}_T^{\mu\mu}) > 30°$	5
$\not\!\!E_T > 40$ GeV if $\Delta\phi(\vec{p}_T^{\mu_1}, \vec{p}_T^{\mu_2}) > 140°$	2
2 jets, $E_T > 15$ GeV, $\|\eta\| < 2.5$	0

decays we require $M_{\mu\mu} > 10$ GeV/c^2.

Muon isolation. For the $\mu\mu$ channel we define muon isolation in terms of $p_T^{\rm rel}$ (isolation algorithm II) and require that both muons have $p_T^{\rm rel} > 5$ GeV/c to reject muons from semileptonic decays of b and c quarks.

Cosmic ray rejection. We reject cosmic rays by excluding events in which the two muons are collinear. Events are rejected if $|\eta^{\mu_1} + \eta^{\mu_2}| < 0.3$ and $\Delta\phi^{\mu\mu} > 165°$.

Missing energy verification. If $\not\!\!E_T$ is dominated by the mismeasurement of the momentum of one muon it will point in the direction opposite to that of the muon. To reject such events we require for the leading muon $\Delta\phi(\not\!\!E_T, p_T^{\mu_1}) < 165°$ for two-layer muon tracks and $\Delta\phi(\not\!\!E_T, p_T^{\mu_1}) < 175°$ for three-layer muon tracks.

For $Z \to \mu\mu$ decays, $\not\!\!E_T^{\rm cal}$ gives an independent measurement of the transverse momentum of the dimuon system ($p_T^{\mu\mu}$). These two vectors tend to align [Fig. 17(a)]. In $t\bar{t} \to \mu\mu + X$ decays the two vectors are decorrelated by the two neutrinos from the W decays [Fig. 17(b)]. To reject $Z \to \mu\mu$ decays, we require $\Delta\phi(\not\!\!E_T^{\rm cal}, p_T^{\mu\mu}) > 30°$.

In $Z \to \mu^+\mu^-$, $Z \to \tau^+\tau^- \to \mu^+\mu^- + X$, and $b\bar{b}, c\bar{c} \to \mu\mu + X$ decays, the muons are predominantly produced back to back in ϕ with little or no $\not\!\!E_T$ [Fig. 18(a)]. Figure 18(b) shows that $t\bar{t}$ decays are uniformly distributed in $\Delta\phi^{\mu\mu}$. We require $\not\!\!E_T > 40$ GeV if $\Delta\phi^{\mu\mu} > 140°$ (indicated by the box in Fig. 18).

Jet multiplicity and transverse energy. As for the other dilepton channels (in analysis II), we require at least two reconstructed jets with $E_T > 15$ GeV and $|\eta| < 2.5$. For this analysis we use jets reconstructed with a cone size of $R = 0.7$. This cut further reduces the background from Z decays while having little effect on the acceptance for high mass $t\bar{t}$ events.

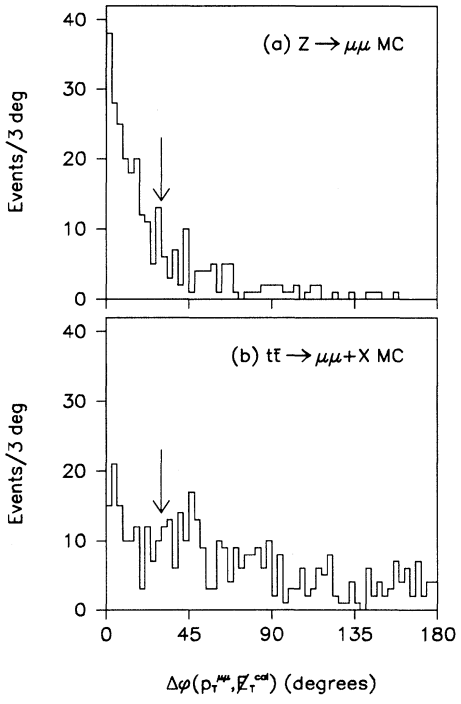

FIG. 17. Azimuthal opening angle $\Delta\phi$ between the dimuon p_T and the $\not\!\!E_T^{\rm cal}$ vectors for (a) $Z \to \mu\mu$ Monte Carlo events ($\int \mathcal{L}dt = 110$ pb^{-1}) and (b) $t\bar{t} \to \mu\mu + X$ MC sample ($m_t = 160$ GeV/c^2, $\int \mathcal{L}dt = 20.8$ fb^{-1}). The arrow describes the selection cut (see text).

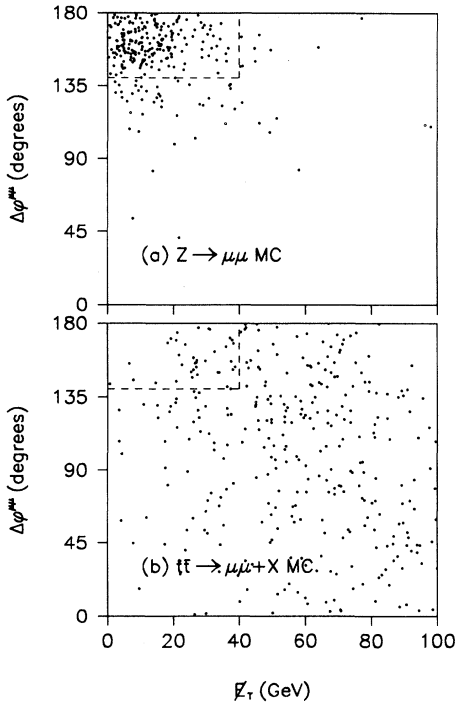

FIG. 18. Correlation of $\Delta\phi^{\mu\mu}$ and $\not\!\!E_T$ for (a) $Z \to \mu\mu$ ($\int \mathcal{L}dt = 110$ pb^{-1}) and (b) $t\bar{t} \to \mu\mu + X$ ($m_t = 160$ GeV/c^2, $\int \mathcal{L}dt = 20.8$ fb^{-1}) Monte Carlo samples. The box represents the selection cuts (see text).

2. *Expected $t\bar{t}$ signal*

The number of $t\bar{t} \to \mu\mu + X$ events passing the selection cuts $N_{\rm pred}$ has been calculated using Eq. (20) in the same way as for the ee channel. Table XVI lists efficiency × branching fraction and expected signal yields, including contributions to $\mu\mu$ final states from $W \to \tau\nu \to \mu\nu\nu\nu$ decays. The contributions to the un-

TABLE XVI. Efficiency × branching fraction ($B_{\mu\mu}$) and predicted event yields for $t\bar{t} \to \mu\mu + X$.

m_t (GeV/c^2)	$\epsilon_{\rm tot} \times B_{\mu\mu}$ (%)	$N_{\rm pred}$
120	0.13 ± 0.02	0.50 ± 0.08
140	0.15 ± 0.02	0.25 ± 0.04
160	0.15 ± 0.02	0.12 ± 0.02
180	0.14 ± 0.02	0.06 ± 0.01
200	0.14 ± 0.02	0.03 ± 0.01

TABLE XVII. Backgrounds to the $t\bar{t} \to \mu\mu + X$ search and associated event yields for 9.8 pb^{-1}.

Background	Event yield
$Z \to \mu\mu$	0.28 ± 0.06
$Z \to \tau\tau \to \mu\mu + X$	$(0.0 \pm 1.8) \times 10^{-2}$
$Z \to b\bar{b}, c\bar{c} \to \mu\mu + X$	$(3.3 \pm 0.7) \times 10^{-3}$
$\gamma^* \to \mu\mu$, $\gamma^* \to \tau\tau \to \mu\mu + X$	$(7.0 \pm 1.5) \times 10^{-3}$
$W^+W^- \to \mu\mu + X$	$(7.0 \pm 1.0) \times 10^{-3}$
$ZW^{\pm} \to \mu\mu + X$	$(1.0 \pm 0.1) \times 10^{-2}$
$ZZ \to \mu\mu + X$	$(5.3 \pm 1.1) \times 10^{-3}$
$W +$ jets $\to \mu\mu + X$ and $b\bar{b}, c\bar{c} \to \mu\mu + X$	$(2.0 \pm 0.1) \times 10^{-2}$
Total:	0.33 ± 0.06

certainty are from event simulation (8%), event reconstruction (10%), trigger simulation (5%), and muon identification (8%).

3. Backgrounds

In the case of the $\mu\mu$ channel there is only one significant background, $Z \to \mu\mu$, after cuts. However, for completeness we have also studied the small contributions from other physics processes. The results are summarized in Table XVII. As with the $e\mu$ channel we find that both the punchthrough and cosmic ray backgrounds are negligible.

4. Summary of $\mu\mu$ channel

The search for $t\bar{t}$ decays with two muons in the final state does not yield any signal events. In this channel, the major source of background is $Z \to \mu\mu$ decays, giving a total of 0.36 ± 0.06 events as the estimated background. We expect to observe 0.50 ± 0.08 events, 0.25 ± 0.04 events, 0.12 ± 0.02 events, 0.06 ± 0.01 events, 0.03 ± 0.01 events for $m_t = 120$, 140, 160, 180, and 200 GeV/c^2, respectively.

VII. ANALYSIS OF LEPTON + JETS EVENTS

A. Analysis methods

The search for top in channels with a single isolated lepton has to contend with a large background from single W production. In $t\bar{t} \to (\mu \text{ or } e) +$ jets events the lepton comes from $W \to (\mu\nu \text{ or } e\nu)$ while the other W decays hadronically. The leptons from W bosons are expected to be well isolated and the presence of a ν should be detected by significant missing transverse energy ($\not\!\!E_T$) in the event. The $t\bar{t}$ events characteristically have additional jets: two b jets, two jets from a W decaying hadronically plus any other jets coming from initial or final state radiation. Typically one would expect at least four jets but the number can be fewer if jets merge or fall below the jet E_T threshold. Even after selecting four jets the number of events from $W +$ jets is larger than for $t\bar{t}$. For example, the expected $W +$ jets cross section times branching fraction for events with an electron and at least four jets ($E_T > 10$ GeV) is 15 pb while the contribution to that channel from $t\bar{t}$ events with a mass of 140 GeV/c^2 is 2.5 pb. Therefore additional requirements are needed to suppress the $W +$ jets background relative to the $t\bar{t}$ signal. One strategy is to require the jets to be more centrally produced and with higher E_T. The effectiveness of that requirement depends on the top mass. Another method is to try to separate events by their shape characteristics. A very effective handle is to tag the b jets, and this will be discussed in Sec. VIII. The analyses in this section will concentrate on nontagged events and exclude those with a muon tag.

The chief source of background to our signal consists of QCD multijet events with or without a real W (the latter happens when a jet is misidentified as an electron and measurement fluctuations result in substantial $\not\!\!E_T$). In either case, most of the jets are produced by gluon radiation or by gluon splitting. On average, the jets in such events tend to have smaller p_T relative to each other than in the $t\bar{t}$ events where most are produced by cascade decays of high mass resonance states. A useful quantity that exploits the differences is aplanarity ($\mathcal{A}$) [46], used extensively in e^+e^- experiments. For each event we define the normalized momentum tensor M_{ab}:

$$M_{ab} = \sum_i p_{ia} p_{ib} \Big/ \sum_i p_i^2 \ , \tag{25}$$

where $\vec{p_i}$ is the three-momentum of the ith object in the laboratory frame and a, b run over x, y, and z. The objects may be jets, leptons, or the W. M_{ab} is a symmetric matrix which can be diagonalized. We compute the eigenvalues Q_j and order them:

$$Q_1 \le Q_2 \le Q_3 \ . \tag{26}$$

The following relations hold:

$$Q_1 + Q_2 + Q_3 = 1 \ , \tag{27}$$

$$Q_1 \ge 0 \ . \tag{28}$$

These eigenvalues can be subsequently used to quantify the shape of the event: for roughly spherical events, $Q_1 \approx Q_2 \approx Q_3$; for planar events, $Q_1 \ll Q_2$; for linear events, $Q_2 \ll Q_3$.

The quantity $\mathcal{A}$ is defined as

$$\mathcal{A} = \frac{3}{2} Q_1 \tag{29}$$

normalized to lie in the range $0 \le \mathcal{A} \le 0.5$. Clearly large $\mathcal{A}$ values characterize spherical events. $\mathcal{A}$ is independent of the overall energy scale of the event but its distribution for signal is weakly dependent on the top mass (m_t) and p_T. The shape of a $t\bar{t}$ event is expected to be most spherical when the momenta of the final state partons are close

in absolute value and opening angles are not small. This occurs when the t and $\bar{t}$ have relatively low p_T and m_t is roughly in the range $1.5m_W < m_t < 2.0m_W$, which is the region of interest. Figure 19 compares the aplanarity for W + 4 or more jets events generated with the VECBOS Monte Carlo program to that of $t\bar{t}$ events generated with ISAJET.

As Fig. 20 illustrates, we expect higher E_T for jets from $t\bar{t}$ than from background events. A measure of transverse hadronic jet activity is the scalar sum of jets E_T (H_T):

$$H_T \equiv \sum_{\text{jets}}^{|\eta|<2} E_T^{\text{jet}} , \tag{30}$$

where the choice of jets with $|\eta| < 2.0$ is motivated by the expectation of more central jets from top events than for background. This quantity is obviously strongly correlated with the top mass and becomes more effective the heavier the top. For a given top mass H_T is practically uncorrelated with $\mathcal{A}$ for $t\bar{t}$ events in the mass range 140–180 GeV/c^2 while showing a tendency to decrease as $\mathcal{A}$ increases for background events (see Sec. VII D). Both H_T and $\mathcal{A}$ are calculated using jets with $E_T > 15$ GeV.

Two somewhat different analyses are described in Secs. VII B and VII C. One (analysis I) was optimized for setting a top mass limit; the data are selected in a way that keeps the acceptance high for relatively low top masses while getting reasonable background rejection. The results of this analysis were published soon after the end of the 1992–1993 data taking run [8] and were based on data collected with Express line triggers. The analysis will be shown in some more detail in this paper but remains unchanged. The other (analysis II) is optimized for good signal-background at higher masses. The intent is not to set a limit but rather search for a top signal in the mass range 140–200 GeV/c^2; these results were summarized in [47].

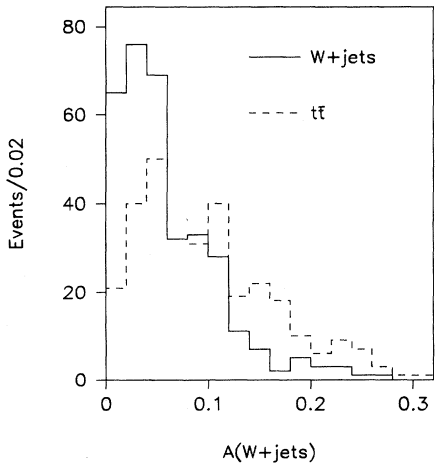

FIG. 19. Aplanarity (using jets and W) for e + 4 or more jets events, solid line background predicted by VECBOS, dashed line for $t\bar{t}$ (top quark mass 140 GeV/c^2) predicted by ISAJET, both normalized to 500 pb^{-1}.

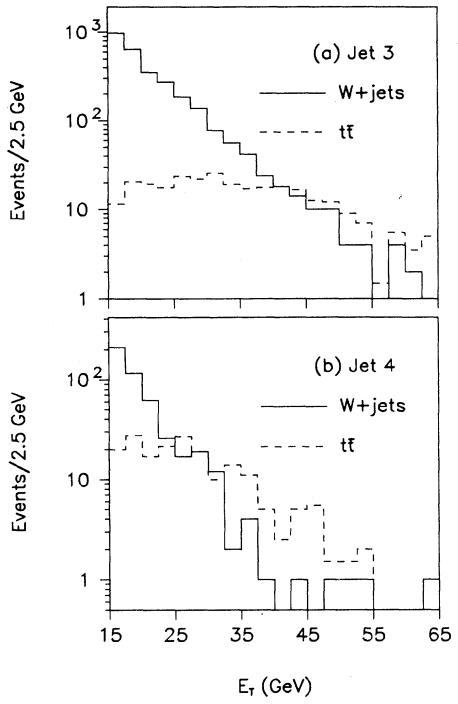

FIG. 20. E_T distributions of the third and fourth jets from $W+ \geq 3$ jets Monte Carlo (solid) and $t\bar{t}$ (dashed) events with top mass 160 GeV/c^2, normalized to 500 pb^{-1}.

Both analyses require at least four jets with $E_T > 15$ GeV, but analysis I makes no additional requirements on the jets and uses only the $\mathcal{A}$ variable to reduce the background. Analysis II makes use of both $\mathcal{A}$ and H_T and limits the jets to $|\eta| < 2.0$. Estimating the background is critical for analysis II so Sec. VII D describes in some detail two different background estimates which rely primarily on data.

B. Electron + jets events

The selection criteria for e + jets events are a tight electron as defined in Sec. IV A with $E_T > 20$ GeV, $\not\!\!E_T^{\text{cal}} > 15$ GeV, and at least one jet with $E_T > 15$ GeV. The electron requirements were somewhat looser in analysis I (tight I) than in analysis II (tight II). For tight I there was no dE/dx cut and the electrons were required to have $|\eta| < 2.5$. For analysis II a dE/dx cut was imposed and the electrons were required to have $|\eta| < 2.0$. More details on the event selection can be found in [48].

Figure 21 shows the $\not\!\!E_T^{\text{cal}}$ distributions for events with electromagnetic showers that satisfy the requirements for a tight II electron and for those that fail (fakes). There is still a noticeable low $\not\!\!E_T$ background remaining in the electron sample which becomes small when the $\not\!\!E_T^{\text{cal}}$ cut

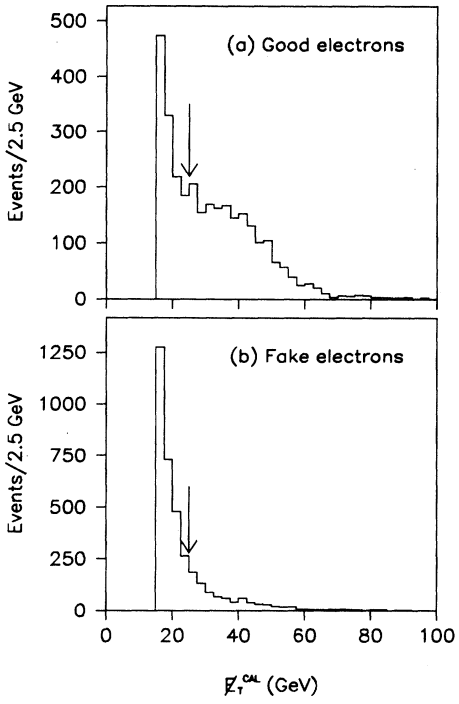

FIG. 21. $\not\!\!E_T^{cal}$ distribution for (a) good electrons, (b) fake electrons.

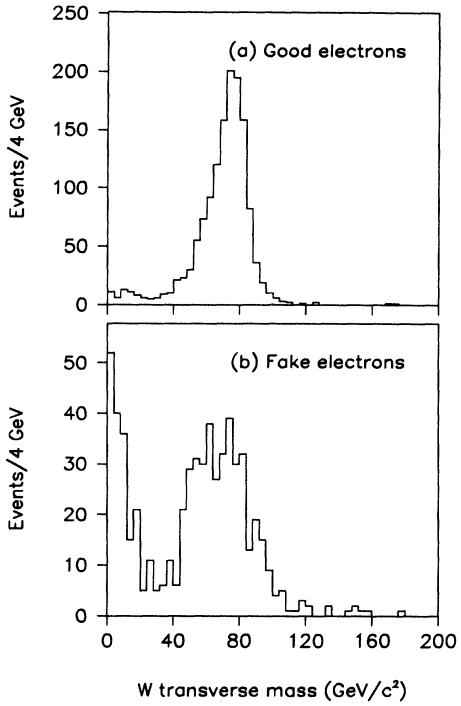

FIG. 22. W transverse mass distribution for (a) good electrons, (b) fake electrons with $\not\!\!E_T^{cal} > 25$ GeV.

is raised to 25 GeV. We will refer to the sample of fake events with $\not\!\!E_T^{cal} < 25$ GeV as the QCD multijet sample. Because of the looser requirements on the electron for analysis I the $\not\!\!E_T^{cal}$ cut in that analysis was raised to 30 GeV.

Analysis I uses Express line triggers only (ELE-MAX, ELE-JET-MAX, see Table II in Sec. III); this lowers the efficiency for low jet multiplicities by about 10% but has negligible impact for events with four or more jets. The W transverse mass distributions (Fig. 22), after these cuts for fakes and good electrons, illustrates the cleanliness of the sample with a tight II electron selection. The geometric acceptance × trigger efficiency for electrons from $t\bar{t}$ events with top mass 140 GeV/c^2 is 60%. After cuts to reduce the fake electron background the efficiency is 48%.

The number of events observed as a function of the number of jets and the expected background from fakes is given in Table XVIII. Each jet is required to have $E_T >$ 15 GeV with no η cut for analysis I (effectively $|\eta| < 3.2$ from detector acceptance). As the signal-to-background ratio is improved for high mass top by limiting the jets η range, for analysis II the jets are limited to $|\eta| < 2.0$. In addition, events with any μ with $p_T^{\mu} > 4.0$ GeV are removed to avoid any overlap with the events selected by the analysis in Sec. VIII. This reduces the acceptance by 25% for top masses higher than 140 GeV/c^2.

To reduce the background in the sample of events with four or more jets further cuts are made using the shape variables $\mathcal{A}$ and H_T described in Sec. VII A. In analysis I only $\mathcal{A}$ is used as H_T is not a very effective variable for masses below 120 GeV/c^2. For the μ + jets channel, discussed in detail in Sec. VII C, we use $\mathcal{A}_{\text{jets}}$ calculated only from jets while for the e + jets channel we included the reconstructed W since the electron is precisely measured. The W is reconstructed by assuming that the $\not\!\!E_T$

TABLE XVIII. The number of e + jets events as a function of jet multiplicity.

	Analysis I		Analysis II	
Number of jets	e + jets	Non-W background	e + jets	Non-W background
≥ 1	1531	150 ± 10	1374	94 ± 6
≥ 2	319	38 ± 5	241	26 ± 3
≥ 3	66	8.5 ± 1.2	37	5.7 ± 0.9
≥ 4	11	1.5 ± 0.4	8	1.1 ± 0.3
$\mathcal{A}_{W+\text{jets}} > 0.08$	1	0.3 ± 0.2		
$\mathcal{A}_{\text{jets}} > 0.05$, $H_T > 140$ GeV			2	0.2 ± 0.1

TABLE XIX. Efficiency × branching fraction and predicted event yields for $t\bar{t} \to e +$ jets in analyses I and II.

m_t (GeV/c^2)	Analysis I		Analysis II	
	$\epsilon_{\mathrm{tot}} \times B_{e+\mathrm{jets}}$ (%)	N_{pred} for 13.5 pb^{-1}	$\epsilon_{\mathrm{tot}} \times B_{e+\mathrm{jets}}$ (%)	N_{pred} for 13.5 pb^{-1}
90	0.28 ± 0.08	6.8 ± 2.1	–	–
100	0.44 ± 0.12	6.0 ± 1.8	–	–
120	1.13 ± 0.22	5.9 ± 1.3	0.85 ± 0.21	4.4 ± 1.3
140	1.45 ± 0.20	3.3 ± 0.6	1.1 ± 0.3	2.5 ± 0.6
160	1.69 ± 0.20	1.9 ± 0.3	1.5 ± 0.3	1.7 ± 0.4
180	–	–	1.6 ± 0.3	0.9 ± 0.2
200	–	–	1.8 ± 0.4	0.5 ± 0.1

is all due to the ν coming from the W decay. This gives two solutions for the longitudinal momentum of the W; the smaller of the two is chosen as the correct one.

In Fig. 23 we show scatter plots of $\not\!\!E_T^{\mathrm{cal}}$ versus $\mathcal{A}_{W+\mathrm{jets}}$ for QCD multijet events, Monte Carlo $W+ \geq 4$ jets, Monte Carlo $t\bar{t}$ with top mass 120 GeV/c^2, and the data for the $e +$ jets channel. It is clear that imposing $\not\!\!E_T^{\mathrm{cal}} >$ 30 GeV removes most of the QCD multijet background without having much impact on the signal. Requiring $\mathcal{A}_{W+\mathrm{jets}} > 0.08$ reduces the total background by about a factor of 5 while keeping half of the $t\bar{t}$ events. Figure 24(a) shows the $\mathcal{A}$ distribution and the location of the cut; only one event survives. After the cut the QCD multijet background to the $e +$ jets channel is estimated to be 0.3 ± 0.2 events while the number of $W +$ jets events expected is estimated from the $W + 4$ jets VECBOS Monte Carlo program to be 1.8 ± 0.8.

In analysis II both $\mathcal{A}$ and H_T are used to reduce the background but $\mathcal{A}$ is calculated using only jets so the $e +$ jets and $\mu +$ jets samples can be combined to estimate the background. Figure 25 shows the distribution of events in

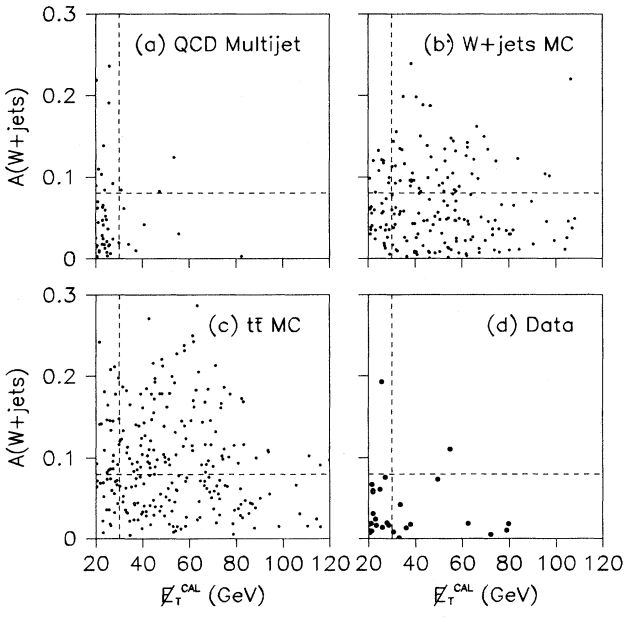

FIG. 23. $\mathcal{A}$ vs $\not\!\!E_T^{\mathrm{cal}}$ distributions for events with four or more jets: (a) QCD multijet sample, (b) $W + 4$ jets VECBOS Monte Carlo program, (c) $t\bar{t}$ Monte Carlo events, top mass 120 GeV/c^2, (d) $e +$ jets data. The lines show the cuts used to select events for analysis I. The Monte Carlo samples correspond to an integrated luminosity of 300 pb^{-1}.

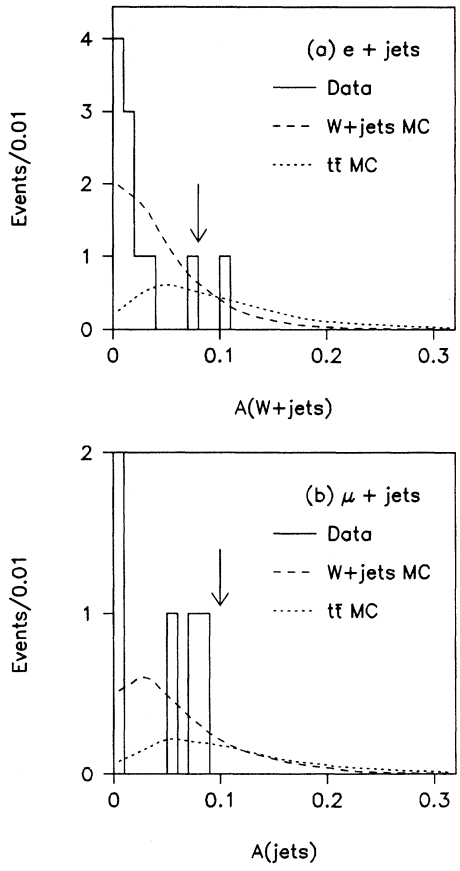

FIG. 24. Aplanarity ($\mathcal{A}$) distributions for events with four or more jets: (a) $e +$ jets sample, (b) $\mu +$ jets sample. The dashed curve is the expected distribution for $W+ \geq 4$ jets; the dotted curve for $t\bar{t}$ with top mass 140 GeV/c^2. The arrow indicates the location of the cut for analysis I.

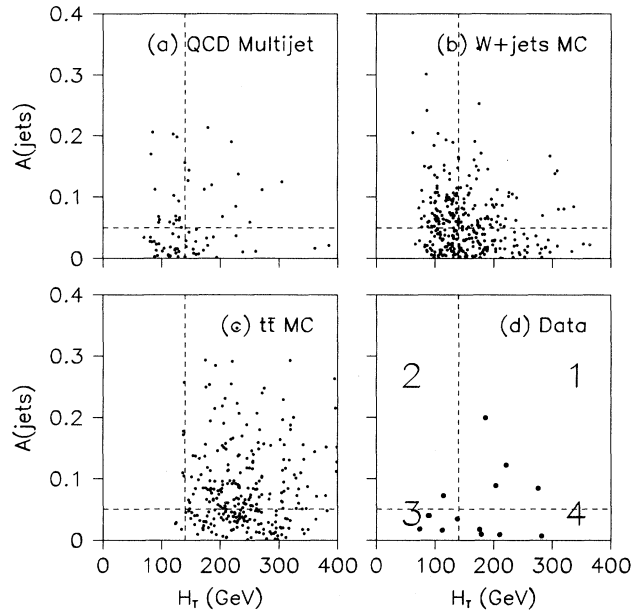

FIG. 25. $\mathcal{A}$ vs H_T distributions for events with four or more jets: (a) QCD multijet sample, (b) VECBOS Monte Carlo program, (c) $t\bar{t}$ events, top mass 180 GeV/c^2, (d) data e and μ + jets combined; the quadrants used in the fit are numbered, see Sec. VII D.

these two variables for the QCD multijet sample, VECBOS Monte Carlo program, $t\bar{t}$ Monte Carlo program with mass 180 GeV/c^2, and the data (e and μ + jets combined). If we divide the $\mathcal{A}$, H_T plane into four quadrants using axes $\mathcal{A} = 0.05$ and $H_T = 140$ GeV/c^2, we see that the QCD multijet sample and the W + jets Monte Carlo sample populate those quadrants more or less equally while 60% of the $t\bar{t}$ events are in the quadrant with $\mathcal{A} > 0.05$ and $H_T > 140$ GeV. In the data two e + jets events are left in this quadrant.

Table XIX gives the acceptance times branching ratio and number of $t\bar{t}$ events expected for analyses I and II. The errors include a 10% uncertainty in $t\bar{t}$ generation, a 10% uncertainty in reconstruction, and a 15% uncertainty due to the jet energy scale (this uncertainty varies from 20% for $m_t = 100$ GeV/c^2 to 10% for $m_t = 200$ GeV/c^2). In Sec. VII D we will describe two methods for estimating the background with minimal reliance on Monte Carlo simulation.

C. Muon + jets events

For μ+jets we require a single tight high-p_T muon with $p_T > 15$ GeV/c (see Sec. IV B), significant transverse energy imbalance in the calorimeter, $\not\!\!E_T^{\rm cal} > 20$ GeV, significant total (calorimeter plus μ) transverse energy imbalance, $\not\!\!E_T > 20$ GeV, and at least one jet with $E_T > 15$ GeV. The event selection differs only slightly between analyses I and II. For analysis I the Express line trigger MU-JET-MAX (see Sec. III) was used. This has a 10% lower efficiency than the MU-JET-HIGH trigger used in analysis II. For more details on the event selection see Ref. [49]. As in the e+jets channel, no η cut was imposed on jets for analysis I while the jets were restricted to $|\eta| < 2.0$ for analysis II. The dominant backgrounds come from Z bosons with only one detected μ and from QCD multijet processes where the μ from a decay other than W satisfies the isolation criteria; the two backgrounds are roughly comparable.

To illustrate the rejection power against QCD multijet background of requiring a tight high-p_T muon with $\not\!\!E_T > 20$ GeV, we show in Fig. 26 the difference in azimuthal angle between the muon and a recoiling jet in events with only one jet before and after the muon isolation and $\not\!\!E_T$ requirements. There still remains a small QCD multijet background estimated at less than 10%. The number of events as a function of the number of jets and the estimated backgrounds are given in Table XX. The QCD multijet background was estimated by extrapolating from the number of events observed with nonisolated muons at each multiplicity to the number expected to survive the isolation cuts (6%). The background from Z+jets was estimated from Monte Carlo events normalized to the number observed in the data when both muons are detected.

The geometric acceptance for muons having a reconstructed transverse momentum satisfying $p_T > 15$ GeV/c and $|\eta| < 1.7$ is found to be $(78 \pm 1)\%$ using $t\bar{t}$ Monte

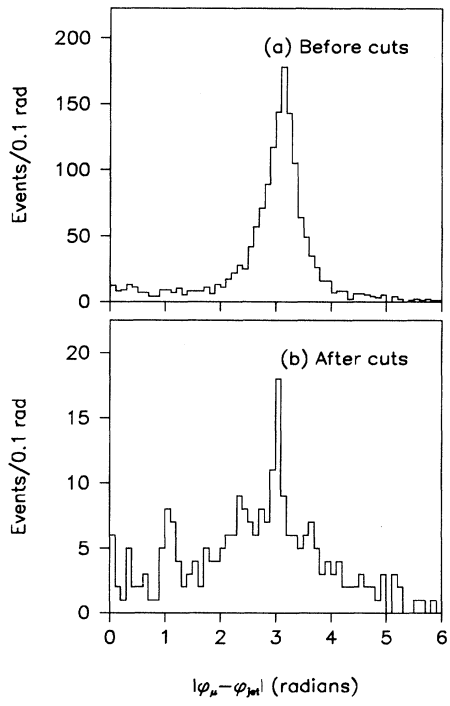

FIG. 26. Absolute value of the difference in azimuthal angle between the μ and the jet in μ + 1 jet events. (a) before isolation and $\not\!\!E_T$ cuts, (b) after cuts.

TABLE XX. The number of μ + jets events as a function of jet multiplicity.

Number of jets	Analysis I		Analysis II	
	μ + jets	Non-W background	μ + jets	Non-W background
≥ 1	299	51 ± 9	295	48 ± 8
≥ 2	88	17 ± 3	81	16 ± 3
≥ 3	20	5.3 ± 1.0	18	4.8 ± 0.8
≥ 4	5	1.5 ± 0.4	6	1.3 ± 0.3
$\mathcal{A}_{\rm jets} > 0.1$	0	0.3 ± 0.1		
$\mathcal{A}_{\rm jets} > 0.05$, $H_T > 140$ GeV			2	0.3 ± 0.1

Carlo events with $m_t = 140$ GeV/c^2. The acceptance increases slightly as the top mass changes from 140 to 180 GeV/c^2.

The acceptance for the jet portion of the trigger is found by measuring the trigger efficiency as a function of jet E_T and convoluting this with the E_T and jet multiplicity spectra in the $t\bar{t}$ Monte Carlo events. Events having a μ-only trigger and either one or two reconstructed jets were used to measure the jet trigger efficiency. The efficiency was found by counting the number of jets having a calorimeter trigger object above threshhold within $\Delta R < 1.0$ of the jet. The overall $t\bar{t}$ acceptance resulting from convoluting this efficiency with the jets in Monte Carlo events is greater than 99%.

The combined trigger acceptance is found from the product of the muon trigger acceptance and the jet trigger acceptance. The result is 53% for single μ events. Because of trigger biases the ratio of e data to μ data is not constant as a function of the number of jets.

To reduce the background in the sample of events with 4 jets further cuts are made using the shape variables $\mathcal{A}$ and H_T described in Sec. VII A. In analysis I only $\mathcal{A}$ is used. For the μ+jets channel we use $\mathcal{A}_{\rm jets}$ calculated only from jets. To have the same background rejection power as in the e + jets channel the cut was set to $\mathcal{A}_{\rm jets} > 0.1$. No events survive the cut, see Fig. 24(b). The expected background is 0.3 ± 0.1 from non-W sources and 1.1 ± 0.7 from W + jets (calculated using the VECBOS Monte Carlo program). For analysis II the same cuts are used in the μ+jets and the e+jets channel, namely $\mathcal{A}_{\rm jets} > 0.05$ and $H_T > 140$ GeV. Events with more than one muon are removed from the sample to avoid any overlap with events found in the analyses of Secs. VI C and VIII. Two μ+jets events pass all cuts. In the next section we will describe two methods for estimating the background to analysis II with minimal reliance on Monte Carlo simulation.

In Table XXI we give the acceptance and the expected number of events after all cuts for analyses I and II. The systematic errors are larger than in the e + jets channel because of an additional 20% uncertainty in the trigger efficiency.

D. Estimation of background

A problem in calculating the background coming from standard single W production is the uncertainty in calculating the higher-order terms needed. The uncertainty in the overall cross section can be in error by perhaps 10% per jet, so the W+ four or more jets cross section has a theoretical uncertainty of at least 40%. In analysis II two different methods were used to decrease that uncertainty by using the data to estimate the background. The first method exploits a noteworthy feature of the data, namely the simple exponential behavior of the number of events as a function of jet multiplicity (this behavior is predicted by Monte Carlo generation of W + jets events). Theoretical expectations [36] suggest that the ratio of number of events when the jet multiplicity increases by one should be roughly constant, i.e.,

$$\frac{W + (n-1) \text{ jets}}{W + n \text{ jets}} = \frac{W + (n-2) \text{ jets}}{W + (n-1) \text{ jets}} \equiv \alpha \ . \qquad (31)$$

TABLE XXI. Efficiency $\times$ branching ratios and predicted event yields for $t\bar{t} \to \mu$ + jets in analyses I and II.

m_t (GeV/c^2)	Analysis I		Analysis II	
	$\epsilon_{\rm tot} \times B_{\mu+\rm jets}$ (%)	$N_{\rm pred}$ for 9.8 pb^{-1}	$\epsilon_{\rm tot} \times B_{\mu+\rm jets}$ (%)	$N_{\rm pred}$ for 9.8 pb^{-1}
90	0.15 ± 0.07	2.7 ± 1.3	–	–
100	0.19 ± 0.08	1.9 ± 0.9	–	–
120	0.61 ± 0.20	2.4 ± 0.8	0.50 ± 0.22	2.4 ± 0.8
140	0.90 ± 0.27	1.6 ± 0.5	0.80 ± 0.20	1.3 ± 0.4
160	0.85 ± 0.24	0.7 ± 0.2	1.1 ± 0.3	0.9 ± 0.4
180	–	–	1.1 ± 0.3	0.5 ± 0.2
200	–	–	1.3 ± 0.4	0.3 ± 0.1

The line in Fig. 27(a) is a fit of a simple exponential to the e + jets data. There is no obvious deviation from theoretical expectations that could be attributed to $t\bar{t}$ production. In particular, one would expect a larger deviation as the jet E_T threshold is raised, as indicated by Fig. 20 which shows the expected E_T distributions of the third and fourth jets (ordered in E_T) in W + jets Monte Carlo events and 160 GeV/c^2 $t\bar{t}$ Monte Carlo events. To estimate how much $t\bar{t}$ production can be accommodated and still satisfy the scaling law, we fitted the data to a function:

$$N_i^{\rm obs} = N_W \alpha^{i-1} + f_i N_t \ , \qquad (32)$$

where $N_i^{\rm obs}$ is the number of observed events for a given multiplicity i, f_i are the fractions of $t\bar{t}$ events expected at multiplicity i, and N_W, α, N_t are the parameters obtained from the fit (number of W + 1 jet events, ratio of multiplicities, total number of top events). The μ + jets and e + jets data were added together after correcting the μ + jets bias at low jet multiplicity. The results of the fit are given in Table XXII. The total number of top events is 5.8 ± 5.7 (3.0 ± 3.0 for four or more jets) while the number of W + 4 or more jets events is 6.3 ± 1.9 and of non-W background 2.4 ± 0.4. The total estimated background in four or more jets is thus 8.7 ± 2.0 before any cuts in the $\mathcal{A}$ and H_T variables. The table includes the predictions from the VECBOS Monte Carlo program for comparison purposes only, they are not used for determining the background level.

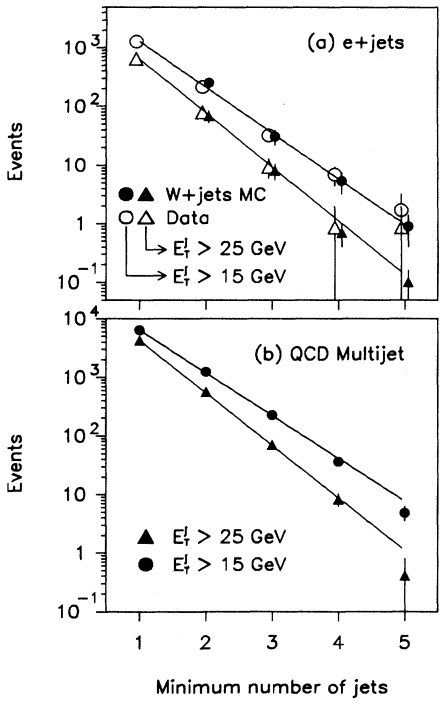

FIG. 27. Number of events as function of jet multiplicity (a) e + jets data after non-W background subtraction and VECBOS predictions (vertical error bars indicate uncertainty in prediction), (b) QCD multijet sample after correcting for increased probability for triggering with increasing multiplicity.

TABLE XXII. W + jets and $t\bar{t}$ events as a function of jet multiplicity (analysis II).

Jets	Data	Non-W background	Results from fit		VECBOS
			W + jets	$t\bar{t}$	W + jets
≥ 1	1669	142 ± 20	1495 ± 96	5.8 ± 5.7	
≥ 2	322	50.6 ± 7.0	265 ± 17	5.7 ± 5.6	293 ± 60
≥ 3	55	10.3 ± 1.5	44.5 ± 5.8	4.5 ± 4.5	41 ± 12
≥ 4	14	2.4 ± 0.4	6.3 ± 1.9	3.0 ± 3.0	8.7 ± 3.5
≥ 5	3	0.6 ± 0.3	1.0 ± 0.5	1.2 ± 1.2	1.3 ± 0.6

To check the validity of the scaling law, we also fitted the QCD multijet sample (fixing N_t to 0). In Table XXIII and Fig. 27(b) we show the jet multiplicities for that sample after correcting for the dependence of jet fake probability on the number of jets. The fake probability as a function of jet multiplicity was calculated by counting the number of jets at each multiplicity in the fiducial volume where electrons can be identified and then multiplying by the probability of a jet faking an electron. The QCD multijet data are clearly well fitted. We also fitted the predictions of the VECBOS Monte Carlo program. All the fits give similar values for α: 0.162 ± 0.009 for the data, 0.160 ± 0.013 for VECBOS Monte Carlo program, 0.187 ± 0.004 for the QCD multijet sample. The jet multiplicity distributions for the Z + jets sample are consistent with the W + jets results within errors. The fit to the VECBOS Monte Carlo program tends to underestimate the predicted number of four or more jet events by 15% while the QCD multijet fit overestimates the number of events with four or more jets by 12%. To account for these deviations, we estimate a 20% systematic error in the validity of the scaling law.

The fraction of top events expected at each multiplicity is obtained from Monte Carlo simulation. To estimate the uncertainty in this procedure we compared two different Monte Carlo programs (ISAJET and HERWIG); the differences between them were of the order of 10%. There is an additional 15% uncertainty in the top acceptance from the uncertainty in the jet energy scale. The estimated number of background events with four or more jets is 8.7 ± 2.0 before including systematic errors (from Table XXII). The fraction of background events satisfying $\mathcal{A} > 0.05$ and $H_T > 140$ is $(21 \pm 3)\%$ (see Table XXIV).

TABLE XXIII. Jet multiplicities for QCD multijet sample.

Jets	Events	Correction	Corrected	Fit
≥ 1	6340	1.00	6340 ± 80	$6416 \pm .77$
≥ 2	1797	1.40	1283 ± 30	1200 ± 28
≥ 3	403	1.78	226 ± 11	224 ± 7
≥ 4	79	2.19	36 ± 4	41.9 ± 3.3
≥ 5	13	2.70	4.8 ± 1.3	7.8 ± 0.8

TABLE XXIV. Relative fractions in the $\mathcal{A}, H_T$ plane for ≥ 4 jets samples.

	ϵ^1 $\mathcal{A} > 0.05$ $H_T > 140$	ϵ^2 $\mathcal{A} > 0.05$ $H_T < 140$	ϵ^3 $\mathcal{A} < 0.05$ $H_T < 140$	ϵ^4 $\mathcal{A} < 0.05$ $H_T > 140$
VECBOS(4 jets)	0.21 ± 0.03	0.27 ± 0.03	0.21 ± 0.03	0.31 ± 0.03
VECBOS(3 jets)	0.19 ± 0.04	0.28 ± 0.05	0.25 ± 0.05	0.28 ± 0.05
QCD multijet	0.19 ± 0.04	0.25 ± 0.05	0.28 ± 0.05	0.28 ± 0.05
$t\bar{t}$ (180 GeV/c^2)	0.60 ± 0.05	0.02 ± 0.01	0.02 ± 0.01	0.36 ± 0.04

Thus the expected background after cuts (e + jets and μ + jets channels combined) is $1.8 \pm 0.4(\text{stat}) \pm 0.6(\text{syst})$.

The second method for estimating the background relies on the distribution of the data with four or more jets in the $\mathcal{A}$ and H_T variables. Figure 25 shows the distribution of events in these two variables for the QCD multijet sample, W+4 jets VECBOS Monte Carlo events, $t\bar{t}$ Monte Carlo events with mass 180 GeV/c^2, and the data (e + jets and μ + jets combined). In Table XXIV we give the expected fractions of W + jets, QCD multijet and $t\bar{t}$ events in the four $\mathcal{A}$, H_T quadrants of Fig. 25.

To calculate the uncertainties in the W + jets estimation we generated W + jets events in two different ways. One was to use VECBOS to generate W + 3 jets events (at the parton level) and use ISAJET with those events as input to generate events with four or more jets. The other was to use VECBOS to generate W + 4 jets and then proceed as in the previous case. One can see in Sec. V that both sets generate quite similar E_T distributions for the third and fourth jets in events with ≥ 4 jets. As shown in Table XXIV, the fractions estimated with the two different Monte Carlo samples differ by less than 20% in any one quadrant. The number of $t\bar{t}$ events in a given quadrant i ($N^i_{t\bar{t}}$) is given by

$$N^i_{t\bar{t}} = \epsilon^i_{t\bar{t}} f_{t\bar{t}} N \ , \tag{33}$$

where N is the total number of observed events with four or more jets, $\epsilon^i_{t\bar{t}}$ is the fraction of $t\bar{t}$ expected in quadrant i, and $f_{t\bar{t}}$ is the fraction of N that are $t\bar{t}$ events. The number of expected background events is then

$$N^i_{\text{bkgd}} = \epsilon^i_{\text{bkgd}}(1 - f_{t\bar{t}})N \ , \tag{34}$$

where N^i_{bkgd} is the number of background events in quadrant i and ϵ^i_{bkgd} is the expected fraction. Given N and the ϵ's one can fit for $f_{t\bar{t}}$.

The results of the fit give $f_{t\bar{t}} = 0.27 \pm 0.25$ in the sample of data with four or more jets. The number of observed events are 4, 1, 4, 5 while the predicted numbers are 4.3, 3.0, 2.7, 4.1 (in the order of the quadrants listed in Table XXIV). There is a large systematic error (35%) from the choice of partitioning the $\mathcal{A}$, H_T plane. This error is estimated by moving the axes until one event falls into a different quadrant. There is an additional 20% systematic error from the uncertainty in calculating the fractions for each quadrant. The number of $t\bar{t}$ events estimated in the sample with four or more jets is thus $3.6 \pm 3.3(\text{stat}) \pm 1.5(\text{syst})$. This value is in good agreement with that obtained fitting the jet multiplicities. Note that each method relies on a different independent set of assumptions and thus has different sources of systematic errors. The background in the quadrant with $\mathcal{A} > 0.05$ and $H_T > 140$ GeV is then calculated as $2.1 \pm 0.7 \pm 0.5$, in good agreement with that calculated using the scaling law ($1.8 \pm 0.4 \pm 0.6$). It is worth emphasizing that neither method relies on the total number of $W + \geq 4$ jets events predicted from Monte Carlo simulation. They rely on the Monte Carlo simulation only to determine the efficiency of the cuts. The fact that the same rejection power is observed in the QCD multijet sample and in two different ways of generating $W + \geq 4$ jets Monte Carlo samples indicates that the assumption is reasonable. The number of observed events after all cuts is 4. This is a small, but not statistically significant, excess over background. In Sec. IX we average the results from both methods and divide the background between the e + jets and μ + jets channels according to their relative acceptance and luminosity.

E. Summary

We have performed two different analyses of the data in channels with one isolated lepton (e or μ) and four or more jets. The first analysis makes use of the event aplanarity, $\mathcal{A}$, to reduce the background to possible top production while keeping the acceptance reasonably high for top masses between 90 and 130 GeV/c^2. Only one event survives the cut for an expected background of 3.8 ± 1.4 events, showing no evidence for any top production.

The second analysis made use of an additional variable, H_T, which is effective for top masses above 140 GeV/c^2, to reduce the background. To avoid overlap with the analysis in Sec. VIII events with a tagging muon were removed from the sample. We observed four events. The background in the second analysis was estimated from data using two different methods, one extrapolating from events with low jet multiplicity, and the other from the distribution of events with four or more jets in the $\mathcal{A}$ and H_T variables. Both methods give a comparable estimate for the background. By averaging both results we estimate the number of background events to be 2.0 ± 0.8 events.

VIII. ANALYSIS OF LEPTON + JETS WITH μ TAGGING

Standard model $t\bar{t}$ events that decay according to the lepton + jets signature include among their decay products two b quarks and an average of 2.5 c quarks. Each b or c hadron can decay semileptonically into a muon with a branching fraction of about 10%. The probability of a $t\bar{t}$ event containing at least one muon from b or c hadron decay is 44%. The processes that are the main backgrounds to the top quark lepton + jets signature, namely W + jets and QCD multijet production, are much less rich than $t\bar{t}$ in heavy flavor quarks and the resulting muons. Muon tagging therefore provides an effective method of reducing the background and improving the signal-to-background ratio in the lepton + jets top quark search.

Muons arising from b and c quark decay can be readily distinguished from muons arising directly from top quark or direct vector boson decay by the fact that they have relatively low momentum (the average p_T of muons from b and c decay from a 160 GeV/c^2 top quark is 17 GeV/c) and by the fact that they are found in close proximity with jets. The D0 muon detection system is capable of detecting muons with an efficiency such that $\sim$ 20% of all $t\bar{t}$ events have an observed muon tag. The fraction of W + 3 or 4 jet events with an observed muon tag from all sources (b/c decay, π/K decay, punchthrough) is expected to be about $\sim$ 2%, or about an order of magnitude smaller than the fraction of tagged $t\bar{t}$ events.

The muon-tagged analyses described here were only performed in the high mass analysis (analysis II, see Sec. VI). For analysis II the muon-tagged and untagged (event shape) analyses were kept orthogonal by removing muon-tagged events from the event shape sample, even if they satisfied the event shape criteria. For analysis I, which did not have a separate muon-tagged analysis, muon-tagged events were not removed from the event shape analysis.

Many aspects of the muon-tagged analyses were the same as the corresponding untagged analysis. The quality requirements on all objects other than tagging muons (i.e., electrons, nontagging muons, $\not\!\!E_T$, and jets) were identical to the untagged analyses. The triggers used were also identical. Tagging muons were not required in the trigger.

A. Electron + jets + μ tag

A detailed description of this analysis can be found in Ref. [50].

1. Event selection

The event selection criteria for electron + jets + μ tag were as follows.

One electron (tight II) with

$$E_T > 20 \text{ GeV} \tag{35}$$

and

$$|\eta| < 2.0. \tag{36}$$

Missing transverse energy:

$$\not\!\!E_T^{\text{cal}} > \begin{cases} 20 \text{ GeV} & \text{if } \Delta\phi(\mu, \not\!\!E_T^{\text{cal}}) > 25^\circ , \\ 35 \text{ GeV} & \text{if } \Delta\phi(\mu, \not\!\!E_T^{\text{cal}}) < 25^\circ . \end{cases} \tag{37}$$

This cut is different from the untagged case, which was $\not\!\!E_T^{\text{cal}} > 25$ GeV independent of direction. The directional aspect of the $\not\!\!E_T^{\text{cal}}$ cut is intended to reduce the QCD multijet background (see Sec. VIII A 3). A graphical representation of the cut is shown in Fig. 28.

Three or more jets with

$$E_T > 20 \text{ GeV} \tag{38}$$

and

$$|\eta| < 2.0. \tag{39}$$

The minimum jet multiplicity is one fewer than that used in the untagged analysis, but with a higher minimum E_T (20 GeV instead of 15 GeV).

At least one tagging muon with

$$p_T > 4 \text{ GeV}/c \tag{40}$$

and

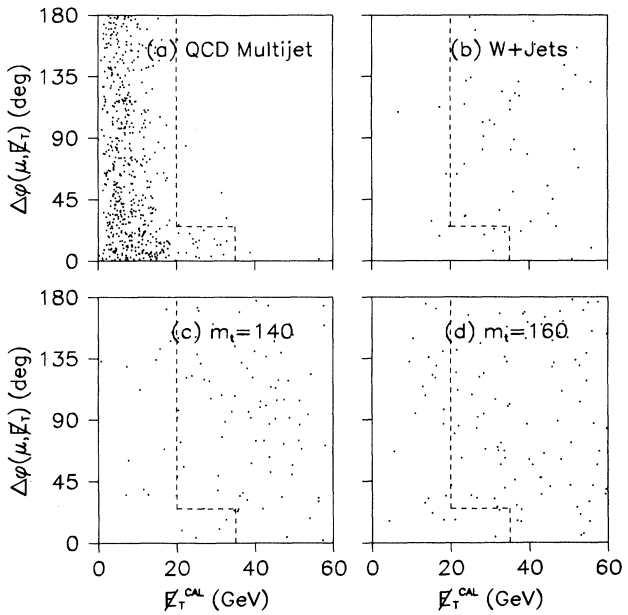

FIG. 28. Distributions of the azimuthal angle between $\not\!\!E_T^{\text{cal}}$ and the muon vs $\not\!\!E_T^{\text{cal}}$ for (a) multijet background sample; (b) W+jets sample (Monte Carlo); (c) $t\bar{t}$ Monte Carlo sample (m_t = 140 GeV/c^2); (d) $t\bar{t}$ Monte Carlo sample (m_t = 160 GeV/c^2). The cuts in these variables are as shown, and are described in the text.

TABLE XXV. Number of observed e + jets events in (13.5 ± 1.6) pb^{-1} of data as a function of the minimum number of jets, with and without a muon tag, and the expected muon-tagged backgrounds. The signal bin is three or more jets with muon tag.

Number of jets	Number of events in 13.5 pb^{-1}				
	Observed		Expected background		
	Untagged	Muon tagged	W + jets	Multijet	Total
≥ 1	1218	7	7.9 $\pm$1.3	1.3 $\pm$0.3	9.2 $\pm$1.3
≥ 2	204	4	2.1 $\pm$0.6	0.6 $\pm$0.3	2.7 $\pm$0.6
≥ 3	34	2	0.43 $\pm$ 0.14	0.12 $\pm$ 0.05	0.55 $\pm$ 0.15
≥ 4	5	1	0.08 $\pm$ 0.04	0.04 $\pm$ 0.04	0.12 $\pm$ 0.06

$$|\eta| < 1.7. \quad (41)$$

In order to keep this analysis orthogonal to the $e\mu$ analysis, tagging muons were required to be nonisolated, or to have $p_T < 12$ GeV/c. Muon quality and isolation criteria for tagging muons are described in Sec. IV B.

Table XXV shows the the number of surviving events for various jet multiplicities.

2. *Expected $t\bar{t}$ signal*

The $t\bar{t}$ efficiency of the cuts described above, including muon tagging, was calculated by simulating $t\bar{t} \rightarrow e$ + jets + μ tag events using the ISAJET Monte Carlo program with detector simulation using the DOGEANT program. The reliability of the muon tagging efficiency calculated by Monte Carlo simulation depends on the ability of ISAJET to reproduce the kinematic properties of muons from b and c quark decay, which in turn depends on the b quark fragmentation function and b and c hadron semileptonic decay form factors, as well as on muon and jet reconstruction efficiencies.

We have tested our understanding of the muon tagging efficiency by looking for tagging muons in an unbiased dijet sample of events. This sample was unbiased in the sense that no trigger or analysis event selection cuts were made that required muons, or that otherwise enhanced the heavy flavor content of the jets. Figure 29(a) shows the muon p_T and Fig. 29(b) the muon-jet separation in $\eta \times \phi$ space, R, for both data and ISAJET Monte Carlo program. The Monte Carlo calculation was done separately for muons resulting from b and c quark decay and from π and K decay. Other potential sources of tagging muons, such as cosmic rays, hadronic punchthrough, and fake hits, are estimated to be negligible and were not included in the Monte Carlo calculation. There is good agreement in shape and normalization between data and Monte Carlo simulation. The relative normalization between data and Monte Carlo simulation is significant and depends on the fraction of dijet events that contain heavy flavor quarks. Note that both b/c decay and π/K decay muons are necessary to reproduce the shape of the ob-

TABLE XXVI. Efficiency $\times$ branching fraction and predicted event yields for $t\bar{t} \rightarrow e$ + jets + μ tag (analysis II) for several top quark masses.

m_t (GeV/c^2)	$\epsilon \times B_{e+\text{jets}}$ (%)	N_{pred} in 13.5 pb^{-1}
140	0.6 $\pm$ 0.2	1.4 $\pm$ 0.5
160	0.9 $\pm$ 0.2	1.0 $\pm$ 0.3
180	1.1 $\pm$ 0.2	0.6 $\pm$ 0.1
200	1.4 $\pm$ 0.1	0.4 $\pm$ 0.1

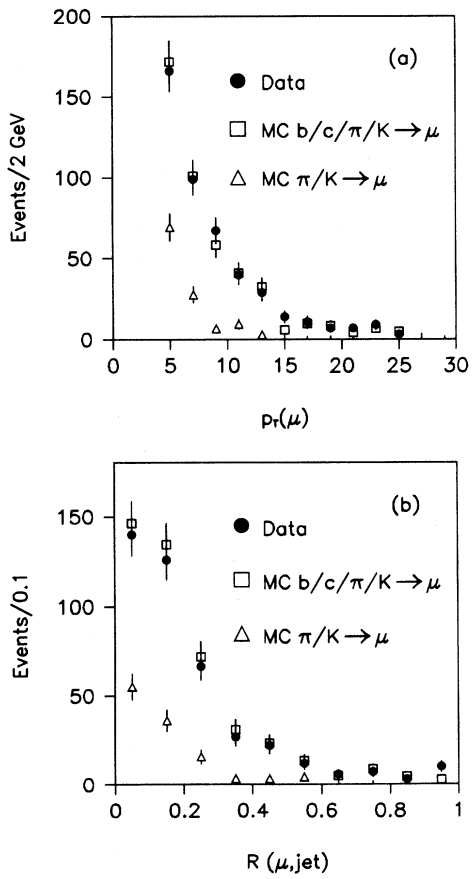

FIG. 29. Comparison of (a) muon p_T and (b) muon-jet separation R between dijet data and ISAJET Monte Carlo program.

served muon spectrum. Also note that there are more muons from heavy flavor decay than from π/K decay. This is typical of tagging muons in all non-flavor-selected jets samples, including those of the background processes.

The efficiency times branching fraction and the expected number of $t\bar{t}$ events are shown in Table XXVI for several top quark masses.

3. Backgrounds

The main backgrounds to $t\bar{t} \to e + \text{jets} + \mu$ tag are the same as in the corresponding untagged channel, namely, W + jets production and QCD multijet production where one jet fakes an electron and the $\not\!\!E_T$ is produced by detector resolution. Neither background is rich in heavy quarks and therefore both of them are highly suppressed by the requirement of a muon tag. The heavy quark content of these processes sets an upper limit on the background rejection that can be obtained from muon tagging. Figure 30 shows some typical Feynman diagrams for the production of (a) heavy quark pairs and (b) single charm quarks with W bosons. The gluon-splitting process shown in Fig. 30(a) is generic in the sense that it is basically independent of the underlying hard scattering process. The fraction of multijet events with heavy flavor quark pairs attributable to gluon splitting should increase linearly with the number of final state gluons (or jets) and should be the same for most processes. In contrast, the fraction of events containing heavy quarks attributable to direct production processes, such as the one shown in Fig. 30(b), is different for different processes, but approximately independent of the number of jets.)

(a) *W + jets background.* We have attempted to characterize the muon tagging probability of various multijet processes in terms of the following variables: process (W + jets, multijet, "fake electron" + jets, photon + jets, Z + jets, etc.), jet multiplicity, jet E_T, $\not\!\!E_T^{\text{cal}}$. We hypothesize, consistent with our observations, that the probability of tagging events with several jets is proportional to the number of jets and independent of process. This hypothesis is consistent with gluon splitting being the dominant source of heavy flavors, but is also consistent with other sources of muon tags, such as heavy flavor hadron production via fragmentation, decays of π's and K's in jets, or hadronic punchthrough.

Figure 31 shows the observed muon tagging rate as a function of the number of jets with $E_T > 15$ GeV and $|\eta| < 2.0$ for two processes, QCD five-jet and "fake electron" + jets production, and a Monte Carlo calculation of the W + jets process. What we call fake electrons are highly electromagnetic calorimeter clusters (i.e., jets) that satisfy electron or photon triggers, but from which good electrons or photons are excluded. The Monte Carlo calculation was based on the VECBOS program for the hard scattering subprocess, with higher-order QCD radiative corrections (including the gluon splitting process) and fragmentation added by the ISAJET program and detector simulation (including π/K decay) added by the DOGEANT program. The results of this study are consistent with the hypothesis of process-independent tagging rate proportional to the number of jets. In the Monte Carlo calculation, about 70% of observed tagging muons are from heavy flavor decay, and 30% are from π/K decay.

The jet E_T dependence of the tagging probability is shown in Fig. 32 for fake electron + jets events. The tagging probability of jets increases with the jet E_T. We can use the E_T-dependent jet tagging probability to predict any kinematic distribution for muon-tagged processes from the corresponding untagged process. Two cross checks of this method are shown in Figs. 33 and 34. Figure 33 shows the predicted and observed E_T spectrum of muon-tagged jets in dijet events. Figure 34 shows the predicted and observed jet multiplicity distribution in (a)

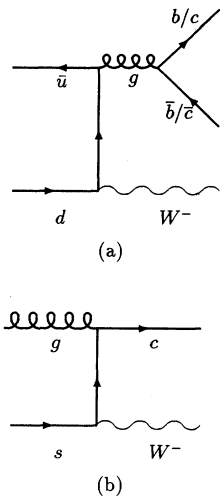

FIG. 30. Typical Feynman diagrams contributing to heavy flavor production with W bosons: (a) gluon splitting to $b\bar{b}$ / $c\bar{c}$ pairs and (b) single charm production.

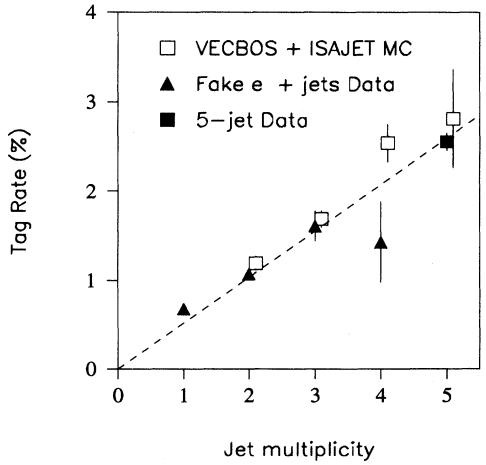

FIG. 31. Fraction of events containing muons as a function of jet multiplicity.

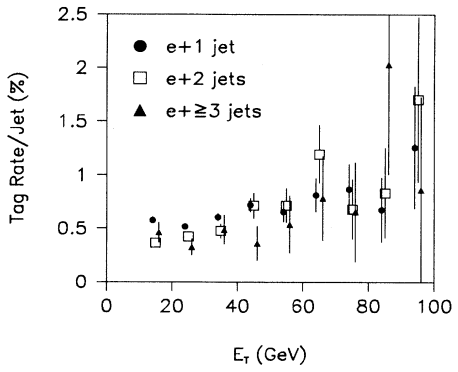

FIG. 32. Muon-tagging fraction as a function of jet E_T in fake electron + jets events.

photon + jets events and (b) QCD multijet events.

We present two final checks of our understanding of the muon-tagging rate in W and Z + jets events. Figure 35 shows the predicted and observed number of W + 1 jet + μ tag events as a function of the minimum E_T of the jet. There is good agreement. Table XXVII shows the predicted and observed number of Z + jets + μ tag events for one, two, and three or more jets. We predict that we should see 1.41 ± 0.10 events and we do not see any.

(b) *Multijet background.* Figure 36 shows the QCD multijet background for untagged W + jets events for one, two, and three jets. This background occurs when one jet in a multijet event is misidentified as an electron, and simultaneously the $\not\!\!E_T^{\rm cal}$ fluctuates to a large value. This background is modeled by normalizing the fake electron + jets spectrum, which does not contain any real W bosons, to the electron + jets spectrum for $\not\!\!E_T^{\rm cal} < 15$ GeV.

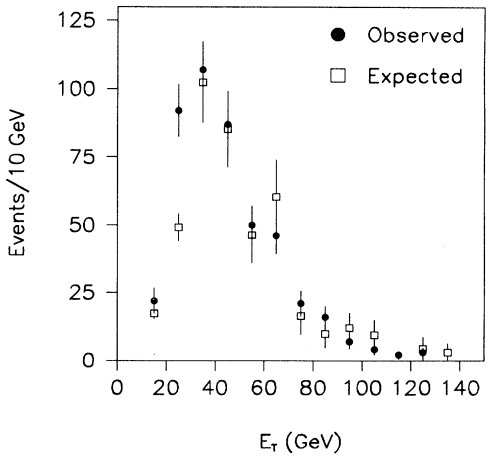

FIG. 33. Predicted and observed E_T spectrum of tagged jets in QCD dijet events.

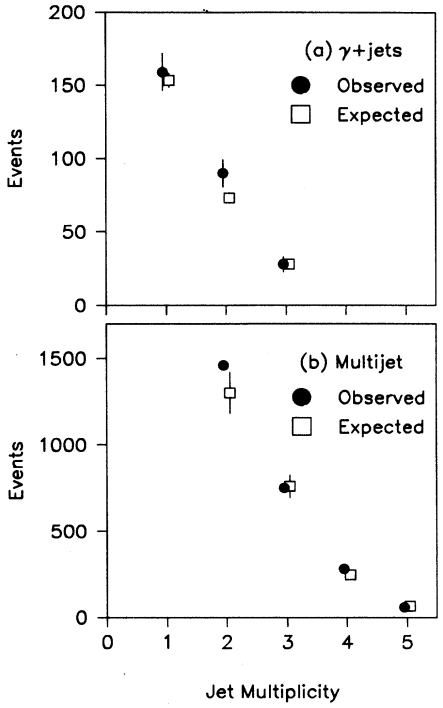

FIG. 34. Jet multiplicity distribution of muon-tagged events for (a) photon + jet events and (b) QCD multijet events compared to the distribution predicted from untagged events.

Muon-tagged events have a worse $\not\!\!E_T^{\rm cal}$ resolution than untagged events (see Fig. 37). Figure 38 shows how the muon-tagging rate increases from its usual value when a $\not\!\!E_T^{\rm cal}$ cut is applied to fake electron + jets events. Since the extra $\not\!\!E_T^{\rm cal}$ is correlated with the muon or its associated muon-neutrino, it is predominantly parallel to

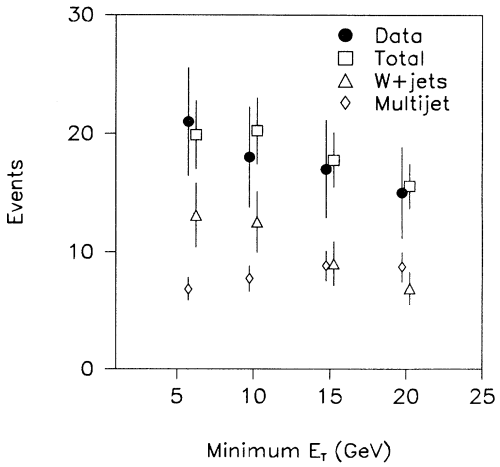

FIG. 35. Comparison of background predictions and data for electron + 1 jet + muon-tag events with $\not\!\!E_T > 20$ GeV as a function of the minimum jet E_T.

TABLE XXVII. Expected and observed muon-tagged Z + jets events.

Data type	Untagged	Muon tagged	
		Expected	Observed
$Z+1$ jet	171	0.97±0.08	0
$Z+2$ jets	36	0.35±0.05	0
$Z+\geq 3$ jets	6	0.09±0.03	0

the muon ϕ direction. This can be seen in Fig. 28, which shows the correlation of $\not\!\!E_T^{\rm cal}$ with the ϕ separation of the $\not\!\!E_T^{\rm cal}$ and the muon $[\Delta\phi(\mu, \not\!\!E_T^{\rm cal})]$ for the two main background processes and for the top quark signal. Figure 28(a) provides the justification for the angle-correlated $\not\!\!E_T^{\rm cal}$ cut [Eq. (37)] as a way to reduce the QCD multijet background.

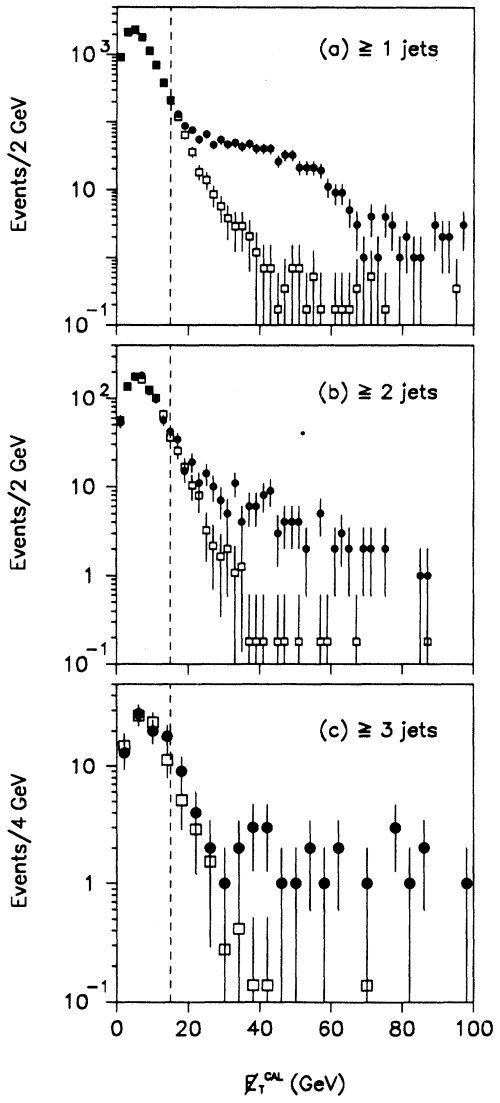

FIG. 36. $\not\!\!E_T^{\rm cal}$ distribution of electron + jet events (solid circles) and fake electron + jet events (open squares) for (a) one or more jets, (b) two or more jets, and (c) three or more jets. The fake electrons are normalized to the good electrons for $\not\!\!E_T^{\rm cal} < 15$ GeV.

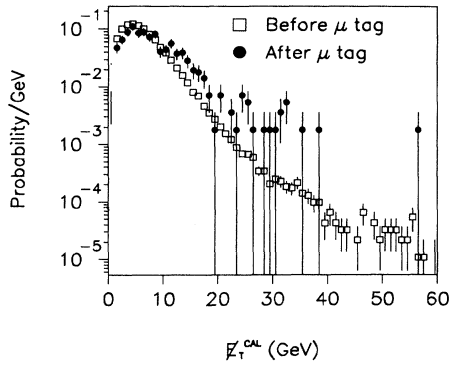

FIG. 37. The $\not\!\!E_T^{\rm cal}$ distribution of the fake electron + ≥ 1 jet events with and without a μ tag. Both curves are normalized to unit area.

The expected W + jets and multijet backgrounds to e + jets + μ tag are shown in Table XXV as a function of the number of jets.

B. Muon + jets + μ tag

1. Event selection

The event selection criteria for muon + jets + μ tag were as follows.

One high-p_T isolated muon (tight) with

$$p_T > 15 \text{ GeV}/c \tag{42}$$

and

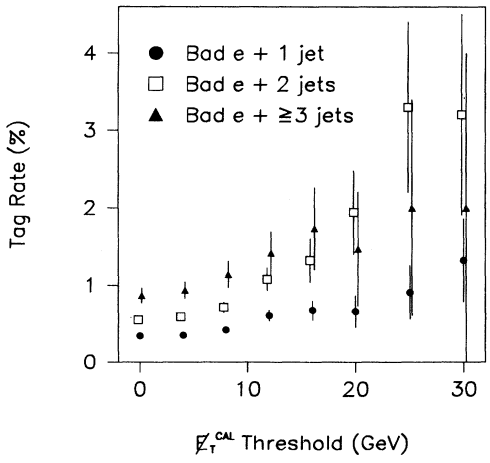

FIG. 38. Muon-tagging rate as a function of the minimum $\not\!\!E_T^{\rm cal}$ cut and jet multiplicity for fake electron + jets events.

$$|\eta| < 1.7. \quad (43)$$

Missing transverse energy:

$$\not\!\!E_T^{\rm cal} > 20 \text{ GeV}, \quad (44)$$

$$\not\!\!E_T > 20 \text{ GeV}. \quad (45)$$

For the highest p_T muon:

$$\Delta\phi(\not\!\!E_T, \mu) < 170° \quad (46)$$

and

$$|\Delta\phi(\not\!\!E_T, \mu) - 90°| / 90° < \not\!\!E_T/(45 \text{ GeV}). \quad (47)$$

The first two of the above cuts [Eqs. (44) and (45)] are the same as in the untagged analysis. The last two [Eqs. (46) and (47)] are directional cuts specific to the muon-tagged analysis. Taken together, Eqs. (45)–(47) describe a graphical cut in the $\not\!\!E_T$-$\Delta\phi(\not\!\!E_T, \mu)$ plane (see Figs. 39 and 40). The directional cuts reduce the QCD multijet background.

Three or more jets with

$$E_T > 20 \text{ GeV} \quad (48)$$

and

$$|\eta| < 2.0. \quad (49)$$

This is one fewer jet than was required in the untagged mode, but with a higher minimum E_T (20 GeV instead of 15 GeV). This is the same jet-counting requirement as the e + jets + μ-tag analysis.

At least one tagging muon with

$$p_T > 4 \text{ GeV}/c \quad (50)$$

and

$$|\eta| < 1.7. \quad (51)$$

The tagging muon was required to be nonisolated or to have $p_T < 15$ GeV/c.

Inconsistent with $Z(\rightarrow \mu\mu)$ + jets hypothesis with $P(\chi^2) < 0.01$ (see Sec. VIII B 3).

Table XXVIII shows the the number of surviving events for various jet multiplicities.

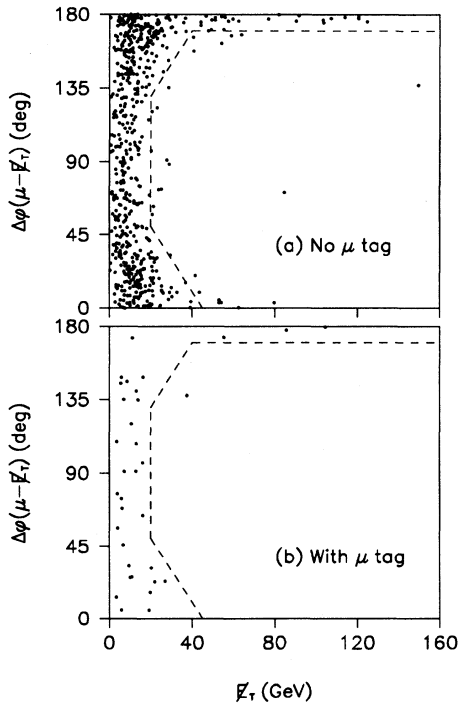

FIG. 39. The correlation of the angle $\Delta\phi$ between the total $\not\!\!E_T$ and the highest p_T muon with the total $\not\!\!E_T$ for multijet events having a nonisolated high-p_T muon (a) without and (b) with an additional tagging muon.

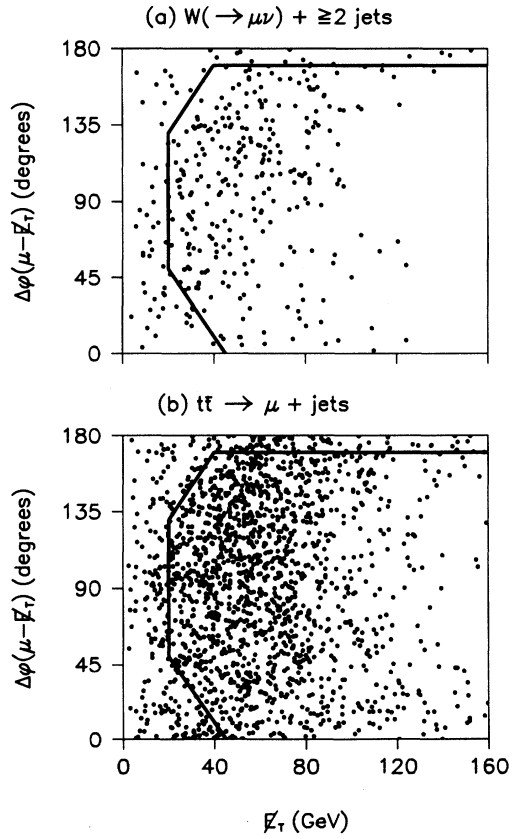

FIG. 40. The correlation of the angle $\Delta\phi$ between the total $\not\!\!E_T$ and the highest p_T muon with the total $\not\!\!E_T$ for simulated W + jets and $t\bar{t}$ events ($m_t = 160$ GeV/c^2). The luminosities of the two samples are 80 pb^{-1} and 3240 pb^{-1}, respectively.

TABLE XXVIII. Number of observed μ + jets + μ-tag events in 9.8 ± 1.2 pb^{-1} of data as a function of the minimum number of jets, and the expected background. The signal bin is three or more jets.

Number of jets	Number of events in 9.8 pb^{-1}				
	Observed	Expected background			
		W + jets	Z + jets	Multijet	Total
≥ 1	5	1.7 ± 0.1	0.5 ± 0.4	0.7 ± 0.1	2.9 ± 0.5
≥ 2	3	0.6 ± 0.1	0.2 ± 0.2	0.3 ± 0.1	1.1 ± 0.3
≥ 3	2	0.2 ± 0.1	0.1 ± 0.1	0.1 ± 0.1	0.4 ± 0.1
≥ 4	1	0.1 ± 0.1	0.02 ± 0.02	< 0.02	0.1 ± 0.1

2. *Expected $t\bar{t}$ signal*

The $t\bar{t}$ efficiency of the above cuts was calculated by simulating $t\bar{t} \rightarrow \mu$ + jets + μ tag using the ISAJET Monte Carlo program with detector simulation using the DOGEANT program. The efficiency times branching fraction and the expected number of $t\bar{t}$ events are shown in Table XXIX.

3. *Backgrounds*

The main backgrounds to $t\bar{t} \rightarrow \mu$ + jets + μ tag are (a) W + jets, (b) $Z(\rightarrow \mu\mu)$ + jets, and (c) QCD multijet production.

(a) *W + jets background.* As was the case with e + jets + μ tag, the largest background is from W + jets production. The W + jets background was calculated by multiplying the measured rate of untagged W + jets by the measured jet-tagging rates (Fig. 32), exactly as was done for e + jets + μ tag. An upward correction to the trigger efficiency was made to account for the fact that the tagging muon may satisfy the muon trigger. Because of the muon-trigger p_T threshold (nominally 8 GeV/c), tagging muons have a lower trigger efficiency than high-p_T muons. Nevertheless, the presence of the tagging muon increased the muon-trigger efficiency from 53% to 70%, or a relative increase of 32%. The tagging muon trigger efficiency was measured using non-muon-trigger jet data. The predicted background, based on seven W + 3 jet events is 0.20 ± 0.08 events.

(b) *Z + jets background.* In the process $Z(\rightarrow \mu\mu)$+jets where both muons are detected, there is approximately a 30% chance that one of the two muons will satisfy the criteria for tagging muons. If only the high-p_T muon, $\not\!\!E_T$, jet and tagging muon cuts are applied, the predicted background from $Z(\rightarrow \mu\mu)$+jets is relatively high (0.23 ± 0.07 events). Additional rejection was obtained from the last cut listed in Sec. VIII B 1, which was to require that the event as a whole was inconsistent with the $Z(\rightarrow \mu\mu)$ + jets hypothesis. This cut was based on a constrained chi square fit of the entire event to the $Z(\rightarrow \mu\mu)$ + jets hypothesis using known detector resolutions. The constraints were overall p_T balance between the two muons and the rest of the event (as determined by $\not\!\!E_T^{\rm cal}$) and $m_{\mu\mu} = m_Z$. We required the chi square probability $P(\chi^2)$ to be less than 0.01. Figure 41 shows the $P(\chi^2)$ distribution for (a) simulated $t\bar{t} \rightarrow \mu$+jets+μ tag events and (b) simulated $Z(\rightarrow \mu\mu)$+ ≥ 3 jet events.

TABLE XXIX. Efficiency $\times$ branching fraction and predicted event yields for $t\bar{t} \rightarrow \mu$ + jets + μ tag (analysis II) for several top quark masses.

m_t (GeV/c^2)	$\epsilon \times B_{\mu+\rm jets}$ (%)	$N_{\rm pred}$ in 9.8 pb^{-1}
140	0.4 ± 0.1	0.7 ± 0.2
160	0.5 ± 0.1	0.4 ± 0.1
180	0.7 ± 0.1	0.3 ± 0.1
200	0.8 ± 0.2	0.2 ± 0.1

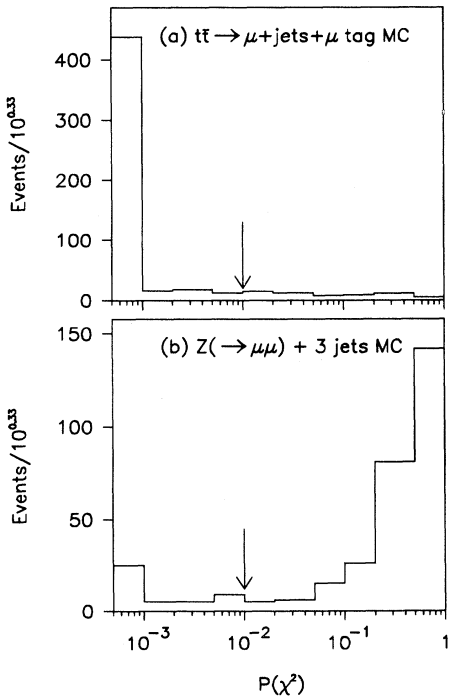

FIG. 41. The χ^2 probability distribution for (a) simulated $t\bar{t} \rightarrow \mu$+jets + μ-tag events (m_t = 160 GeV/c^2) and (b) simulated $Z(\rightarrow \mu\mu)$ + 3 jet events.

Figure 42 shows the $P(\chi^2)$ distributions for simulated $Z \to \mu\mu$ events and $Z \to \mu\mu$ events observed in data. Ideally the $P(\chi^2)$ distribution should be flat for $Z \to \mu\mu$ events and strongly peaked near $P(\chi^2) = 0$ for top quark events. In fact, $Z \to \mu\mu$ events also have a peak near $P(\chi^2) = 0$ due to non-Gaussian tails in the resolution function and backgrounds. The rejection factor of the cut $P(\chi^2) < 0.01$ measured from data [Fig. 42(b)] is 2.8 ± 0.8 (statistical errors). The different rejection in data and Monte Carlo data is used as a measure of the systematic error of the $P(\chi^2)$ cut, giving a background from $Z(\to \mu\mu)$ + jets of 0.08 ± 0.03(stat) $\pm$ 0.05(syst) events.

(c) *Multijet background.* The QCD multijet background to μ + jets + μ tag occurs when multijet events are produced that contain two muons from the sources that normally give rise to tagging muons (i.e., b/c decay and π/K decay). Because of fluctuations, such as an accompanying jet having very low energy, one of the two muons satisfies the criteria for a high-p_T isolated muon. The fact that one muon passes a relatively high-p_T cut of 15 GeV/c ensures that this background is in fact mostly $b\bar{b}$ + jets [see Fig. 29(a)]. This process has been studied using a control sample of events that satisfy all event selection cuts, except that the high-p_T muon fails the isolation cut. The $\not\!\!E_T$ resolution of these events is strongly correlated with the direction of the muons, and especially with the high-p_T muon. Figure 39 shows scatter plots of the ϕ separation between $\not\!\!E_T$ and the high-p_T muon [$\Delta\phi(\mu, \not\!\!E_T)$] versus $\not\!\!E_T$ for multijet events containing a high-p_T nonisolated muon, with and without an additional tagging muon. The contour generated by the three $\not\!\!E_T$ cuts [Eqs. (45)–(47)] is also shown. This figure is the justification of this set of cuts. Figure 40 shows the same distribution for simulated W + jets + μ tag and $t\bar{t} \to \mu$ + jets + μ tag. The expected multijet background to the μ + jets + μ tag top quark signal was calculated from the number of untagged, nonisolated μ + 3 jet events satisfying all other relevant cuts. The observed rate for these events was multiplied by the measured muon isolation probability for muons in μ + jets events of $(6.5 \pm 0.4)\%$ and the calculated tagging probability for the second b quark of $(5.1 \pm 0.7)\%$. As with the W + jets + μ tag background, there is also an upward correction of the trigger efficiency by 32% from the presence of a second muon.

TABLE XXX. Test of μ + jets + μ-tag QCD multijet background calculation as a function of inclusive jet multiplicity using low-$\not\!\!E_T$ μ + jets + μ-tag events. The columns for the W and Z backgrounds are taken from Monte Carlo predictions. The column for the multijet background was calculated from data by the method described in the text.

Number of jets	Background events				Data
	W + jets	Z + jets	Multijet	Total	events
≥ 1	1.6 ± 0.3	6 ± 2	34 ± 7	42 ± 8	44
≥ 2	1.1 ± 0.4	1.6 ± 0.3	6.3 ± 1.0	9 ± 1	15
≥ 3	0.2 ± 0.1	0.4 ± 0.2	0.8 ± 0.2	1.4 ± 0.3	5

The methodology for calculating the QCD multijet background was tested using events that passed all μ + jets + μ tag selection criteria except for the $\not\!\!E_T$ cuts. There is good agreement between the low-$\not\!\!E_T$ μ + jets + μ tag data and the expected background (see Table XXX).

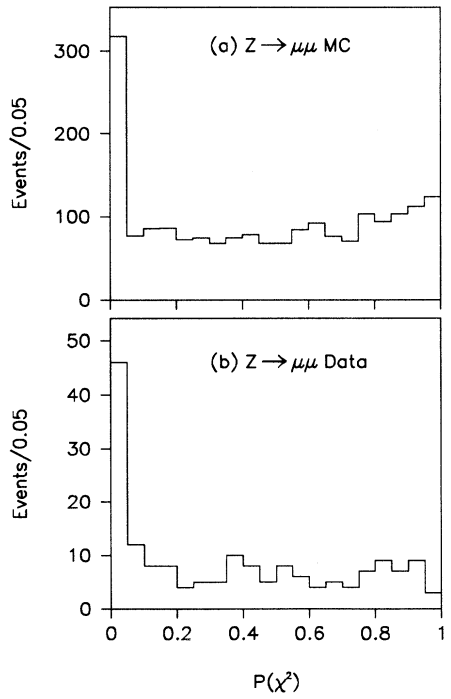

FIG. 42. The χ^2 probability distributions for (a) simulated $Z \to \mu\mu$ events and (b) data $Z \to \mu\mu$ events.

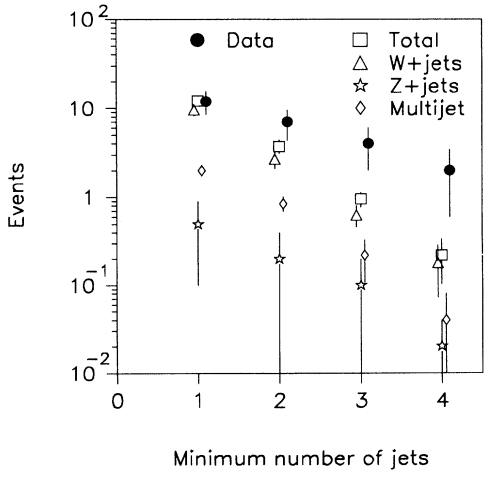

FIG. 43. Observed lepton + jets + μ tag events (solid circles) and expected backgrounds (open points) as a function of the minimum number of jets.

The expected background from all sources and the number of events observed in the data are shown in Table XXVIII.

C. Summary

As part of the high mass top quark analysis (analysis II), we have searched for events with one high p_T isolated lepton (e or μ), $\not\!\!E_T$, three or more jets, and a tagging muon. Figure 43 shows the number of events for e and μ combined, and the expected backgrounds. The final sample contains four events with an expected background of 1.0 ± 0.2 events. Of the four events, two would have satisfied the untagged single-lepton event selection described in Sec. VII (analysis II) in the absence of a tagging muon.

IX. CROSS SECTIONS AND MASS LIMITS

The results from analysis I [8], based on four channels, are summarized in Table XXXI. The expected number of events, $\langle N \rangle$, is calculated using the theoretical top cross section multiplied by the efficiency, branching fraction, and luminosity for each channel. Also included is the number of observed events and expected background for each channel. Adding all four channels together, there are three observed events with an expected background of 5.4 ± 1.4 events. We set an upper limit on the top cross section without subtracting the expected background from the number of observed events. The 95% confidence level (C.L.) upper limit on the cross section is obtained by convoluting a Poisson probability for the number of observed events, with Gaussian distributions for the uncertainties in luminosity and efficiency as a function of the top mass (m_t). Figure 44 shows the resulting 95% C.L. upper limit curve for the $t\bar{t}$ cross section as a function of m_t. The intersection of this curve with the predicted $t\bar{t}$ cross section lower bound [21] yields a lower limit on m_t of 128 GeV/c^2. This is slightly lower than the limit of 131 GeV/c^2 published earlier as a result of a recalibration of the integrated luminosity [9].

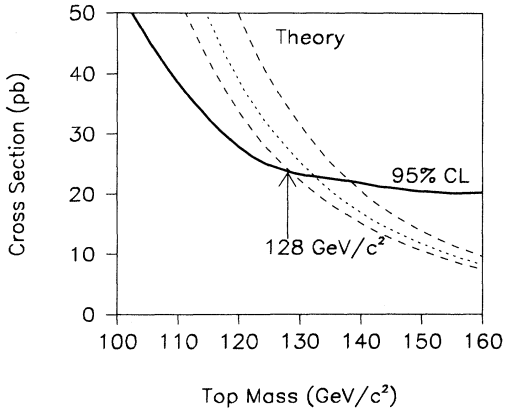

FIG. 44. 95% confidence level on $\sigma_{t\bar{t}}$ as function of top mass from low mass analysis. Also shown are central (dotted line), high, and low (dashed lines) theoretical cross section curves [21].

Table XXXII summarizes the results of analysis II for all seven channels used. The channel $\mu\mu$+jets is included in the high mass analysis and the e + jets and μ + jets channels with and without μ tag are now treated as separate channels. In analysis I the signal-to-background ratio was one to one when the top mass is 150 GeV/c^2

TABLE XXXI. Efficiency × branching fraction ($\varepsilon \times B$), expected number of events ($\langle N \rangle$) for signal [21] (errors do not include the $\sigma_{t\bar{t}}$ theoretical uncertainty) and background sources for the observed integrated luminosity ($\int \mathcal{L}dt$), and number of events observed in the data, for analysis I.

m_t (GeV/c^2)		$e\mu$	ee	e + jets	μ + jets	All
	$\varepsilon \times B$(%)	0.39 ± 0.10	0.16 ± 0.02	0.28 ± 0.08	0.15 ± 0.07	
90	$\langle N \rangle$	9.4 ± 2.6	4.0 ± 0.8	6.8 ± 2.1	2.7 ± 1.3	22.9 ± 3.6
	$\varepsilon \times B$(%)	0.46 ± 0.11	0.20 ± 0.03	0.44 ± 0.12	0.19 ± 0.08	
100	$\langle N \rangle$	6.3 ± 1.7	2.8 ± 0.5	6.0 ± 1.8	1.9 ± 0.9	17.0 ± 2.7
	$\varepsilon \times B$(%)	0.49 ± 0.12	0.26 ± 0.04	1.13 ± 0.22	0.61 ± 0.20	
120	$\langle N \rangle$	2.6 ± 0.7	1.4 ± 0.3	5.9 ± 1.3	2.4 ± 0.8	12.3 ± 1.7
	$\varepsilon \times B$(%)	0.54 ± 0.13	0.28 ± 0.04	1.45 ± 0.19	0.90 ± 0.27	
140	$\langle N \rangle$	1.2 ± 0.3	0.6 ± 0.1	3.3 ± 0.6	1.6 ± 0.5	6.7 ± 0.8
	$\varepsilon \times B$(%)	0.56 ± 0.14	0.29 ± 0.04	1.69 ± 0.18	0.85 ± 0.24	
160	$\langle N \rangle$	0.6 ± 0.2	0.3 ± 0.1	1.9 ± 0.3	0.7 ± 0.2	3.5 ± 0.4
Physics background		0.5 ± 0.2	0.2 ± 0.1	2.1 ± 1.1	1.1 ± 0.7	3.9 ± 1.3
Fake background		0.6 ± 0.3	0.3 ± 0.1	0.3 ± 0.3	0.3 ± 0.1	1.5 ± 0.4
Total background		1.1 ± 0.4	0.5 ± 0.2	2.4 ± 1.3	1.4 ± 0.9	5.4 ± 1.4
$\int \mathcal{L}dt$ (pb^{-1})		13.5 ± 1.6	13.5 ± 1.6	13.5 ± 1.6	9.8 ± 1.2	
Data		1	1	1	0	3

TABLE XXXII. Efficiency × branching fraction ($\varepsilon \times B$) and the expected number of events ($\langle N \rangle$) in the seven channels, based on the central theoretical $t\bar{t}$ production cross section of Ref. [21], for four top masses. Also given is the expected background, integrated luminosity, and the number of observed events in each channel for analysis II.

m_t (GeV/c^2)		$e\mu$ + jets	ee + jets	$\mu\mu$ + jets	e + jets	μ + jets	e + jets/μ	μ + jets/μ	All
	$\varepsilon \times B$(%)	0.31 ± 0.04	0.18 ± 0.02	0.15 ± 0.02	1.1 ± 0.3	0.8 ± 0.2	0.6 ± 0.2	0.4 ± 0.1	
140	$\langle N \rangle$	0.72 ± 0.12	0.41 ± 0.07	0.25 ± 0.04	2.5 ± 0.7	1.3 ± 0.4	1.4 ± 0.5	0.7 ± 0.2	7.2 ± 1.3
	$\varepsilon \times B$(%)	0.36 ± 0.05	0.20 ± 0.03	0.15 ± 0.02	1.5 ± 0.3	1.1 ± 0.3	0.9 ± 0.2	0.5 ± 0.1	
160	$\langle N \rangle$	0.40 ± 0.08	0.22 ± 0.04	0.12 ± 0.02	1.7 ± 0.5	0.9 ± 0.3	1.0 ± 0.3	0.4 ± 0.1	4.7 ± 0.8
	$\varepsilon \times B$(%)	0.39 ± 0.05	0.21 ± 0.03	0.14 ± 0.02	1.6 ± 0.3	1.1 ± 0.3	1.1 ± 0.2	0.7 ± 0.1	
180	$\langle N \rangle$	0.23 ± 0.04	0.12 ± 0.02	0.06 ± 0.01	0.9 ± 0.3	0.5 ± 0.1	0.6 ± 0.1	0.3 ± 0.1	2.7 ± 0.4
	$\varepsilon \times B$(%)	0.40 ± 0.05	0.30 ± 0.04	0.14 ± 0.02	1.8 ± 0.4	1.3 ± 0.3	1.4 ± 0.1	0.8 ± 0.2	
200	$\langle N \rangle$	0.12 ± 0.02	0.09 ± 0.02	0.03 ± 0.01	0.5 ± 0.1	0.3 ± 0.1	0.4 ± 0.1	0.2 ± 0.1	1.7 ± 0.3
Background		0.27 ± 0.14	0.15 ± 0.11	0.33 ± 0.06	1.3 ± 0.7	0.7 ± 0.5	0.6 ± 0.2	0.4 ± 0.1	3.8 ± 0.9
$\int \mathcal{L}dt$ (pb^{-1})		13.5 ± 1.6	13.5 ± 1.6	9.8 ± 1.2	13.5 ± 1.6	9.8 ± 1.2	13.5 ± 1.6	9.8 ± 1.2	
Data		1	0	0	2	2	2	2	9

while for analysis II that ratio is one to one, with comparable acceptance, for a top mass of 170 GeV/c^2.

Adding all channels together, there are nine observed events with an expected background of 3.8±0.9 events. In the absence of top quarks, we calculate the probability of an upward fluctuation of the background to nine or more events to be 2.7%.

The $t\bar{t}$ cross section for top quark masses of 140, 160, 180, and 200 GeV/c^2 uses the results given in Table XXXII. Assuming that the observed excess is due to $t\bar{t}$ production, we calculated the top cross section according to the equation $\sigma_{t\bar{t}} = \sum_{i=1}^{7} (N_i - \mathcal{B}_i)/\sum_{i=1}^{7} \varepsilon_i B_i L_i$, where N_i is the number of observed events for decay channel i, $\mathcal{B}_i$ is the expected background, ε_i is the detection efficiency for a particular mass top, B_i is the branching fraction and L_i is the integrated luminosity. The results are given in Table XXXIII and plotted in Fig. 45.

X. CONCLUSIONS

We have searched for production of $t\bar{t}$ pairs in $p\bar{p}$ collisions at $\sqrt{s}$ = 1.8 TeV assuming the standard model prediction that for top quark masses above the W mass top quarks decay 100% of the time to a W and a b quark. The data were analyzed in two different ways. One way aimed at setting a minimum mass for the top quark, and the second at searching for a possible signal from top quarks with masses in the region m_t =140–200 GeV/c^2.

The first analysis used four different channels. Two channels required at least two isolated high p_T leptons ($e\mu$ or ee) indicating leptonic decays for both W bosons, and at least one additional jet. The other two channels required at least one isolated lepton (e or μ) indicating one W decaying leptonically, and at least four jets, indicating a W decaying hadronically and two additional jets. A total of three events was found and the expected background (predicted from Monte Carlo data) was 5.4 ± 1.4. Assuming all the observed events to be from $t\bar{t}$ production we set a lower limit on the top mass of 128 GeV/c^2, slightly lower than previously published [8] as a result of a recalibration of the integrated luminosity [9].

A second analysis of these data optimized the event selection for high top masses by lowering the background

TABLE XXXIII. $t\bar{t}$ theoretical [21] and measured cross section for top quark masses of 140, 160, 180, and 200 GeV/c^2 assuming the observed excess is due to $t\bar{t}$ production.

m_t (GeV/c^2)	Theoretical $\sigma_{t\bar{t}}$ (pb)	Measured $\sigma_{t\bar{t}}$ (pb)
140	16.9	11.5 ± 7.1
160	8.16	9.2 ± 5.7
180	4.21	8.2 ± 5.1
200	2.26	7.4 ± 4.6

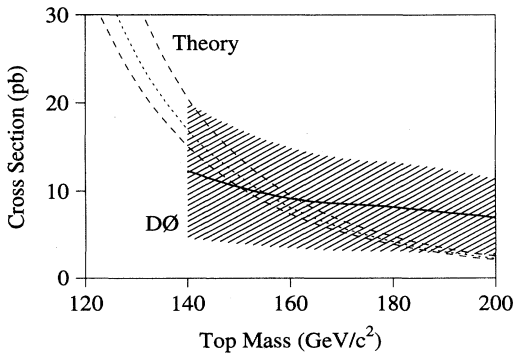

FIG. 45. Measured $t\bar{t}$ production cross section (solid line, shaded band = one standard deviation error) as a function of top mass hypothesis. Also shown are central (dotted line), high and low (dashed lines) theoretical cross section curves [21].

TABLE XXXIV. Parameters of $t\bar{t} \to ee + X$ candidate.

Run 55642, event 2662 (analysis I)		
Particle	E_T (GeV)	η
Electron 1	36.0 ± 1.0	-0.14
Electron 2	28.9 ± 0.8	0.50
Jet1	69.5 ± 12.1	-0.85
Jet2	17.7 ± 3.1	-2.52
$\not\!\!E_T$	44.6 ± 12.2	

TABLE XXXV. Parameters of $t\bar{t} \to e\mu + X$ candidate.

Run 58796, event 7338 (analyses I, II)		
Particle	E_T (GeV)	η
Muon	194.6 > 40.2 at 95% C.L.	0.33
Electron	98.8 ± 1.6	0.40
Jet1	26.1 ± 4.1	-0.70
Jet2	23.0 ± 2.4	1.10
Jet3	7.9 ± 1.2	1.20
$\not\!\!E_T^{\rm cal}$	120.0 ± 2.4	
$\not\!\!E_T$	100.7 > 53.5 at 95% C.L.	

TABLE XXXVI. Parameters of $t\bar{t} \to e +$ jets candidates.

Run 62431, event 788 (analysis II)		
Particle	E_T (GeV)	η
Electron	51.8 ± 1.8	0.98
Jet1	79.3 ± 15.4	-1.57
Jet2	74.5 ± 15.5	0.02
Jet3	33.4 ± 6.7	-1.81
Jet4	18.0 ± 4.4	-0.97
$\not\!\!E_T$	25.4 ± 5.9	
H_T	205.0	
$\mathcal{A}$		0.09

Run 63066, event 13373 (analyses I, II)		
Particle	E_T (GeV)	η
Electron	51.3 ± 1.9	0.18
Jet1	79.5 ± 16.4	-0.04
Jet2	55.0 ± 10.9	-1.54
Jet3	31.6 ± 6.8	-1.16
Jet4	29.6 ± 7.0	0.17
Jet5	28.2 ± 6.3	0.99
$\not\!\!E_T$	53.2 ± 4.9	
H_T	224.0	
$\mathcal{A}$		0.124

TABLE XXXVII. Parameters of $t\bar{t} \to \mu +$ jets candidates.

Run 61275, event 9188 (analysis II)		
Particle	E_T (GeV)	η
Muon	$12.9^{+2.9}_{-2.0}$	-1.35
Jet1	57.1 ± 12.2	-0.31
Jet2	38.5 ± 8.1	1.09
Jet3	29.7 ± 7.0	-0.42
Jet4	25.5 ± 6.3	0.07
Jet5	22.9 ± 5.7	0.27
$\not\!\!E_T$ ($\not\!\!E_T^{\rm cal}$)	$52.4^{+6.4}_{-6.1}$ (49.9 ± 5.8)	
H_T	173.7	
$\mathcal{A}$		0.120

Run 63740, event 14197 (analysis II)		
Particle	E_T (GeV)	η
Muon	$23.8^{+5.3}_{-3.7}$	-0.43
Jet1	103.4 ± 20.5	0.73
Jet2	68.1 ± 14.2	-0.37
Jet3	61.4 ± 12.9	0.44
Jet4	41.1 ± 8.9	0.74
$\not\!\!E_T$ ($\not\!\!E_T^{\rm cal}$)	$55.1^{+8.5}_{-7.7}$ (34.8 ± 6.7)	
H_T	274.0	
$\mathcal{A}$		0.08

while increasing the overall acceptance in the region m_t= 140–200 GeV/c^2. It included an additional final state in the dilepton channels ($\mu\mu$) and the use use of μ tagging or the H_T variable in the lepton + jets channels. A total of nine events was observed with an expected background of 3.8 ± 0.9 events. Unlike the first analysis the estimation of background was based mostly on the data itself.

TABLE XXXVIII. Parameters of $t\bar{t} \to e +$ jets + μ-tag candidates.

Run 57144, event 15138 (analysis II)		
Particle	E_T (GeV)	η
Electron	50.1 ± 1.7	-1.40
Jet1	95.7 ± 18.9	0.92
Jet2	83.1 ± 16.5	1.02
Jet3	38.4 ± 8.7	0.36
Jet4	19.2 ± 5.5	2.32
Jet5	13.1 ± 4.0	0.90
Muon	$4.8^{+0.7}_{-0.5}$	1.00
$\not\!\!E_T$ ($\not\!\!E_T^{\rm cal}$)	91.1 ± 11.0 (86.4 ± 10.0)	

Run 62199, event 13305 (analysis II)		
Particle	E_T (GeV)	η
Electron	65.3 ± 2.2	1.14
Jet1	79.3 ± 16.2	-0.49
Jet2	71.9 ± 15.0	0.76
Jet3	46.6 ± 10.2	0.41
Jet4	30.6 ± 6.6	1.23
Jet5	13.4 ± 4.0	2.67
Muon	$16.3^{+3.2}_{-2.3}$	.02
$\not\!\!E_T$ ($\not\!\!E_T^{\rm cal}$)	$26.6^{+6.4}_{-6.0}$ (23.0 ± 5.5)	

TABLE XXXIX. Parameters of $t\bar{t} \to \mu$ + jets + μ-tag candidates.

Run 58192, event 137 (analysis II)		
Particle	E_T (GeV)	η
Muon	$78.9^{+33.3}_{-18.1}$	−0.09
Jet1	134.3 ± 26.3	0.60
Jet2	40.3 ± 8.6	1.00
Jet3	36.6 ± 8.4	−0.27
Jet4	35.5 ± 7.3	−1.50
Muon	$9.2^{+1.7}_{-1.3}$	0.97
$\not\!\!E_T$ ($\not\!\!E_T^{\rm cal}$)	75.6^{+34}_{-20} (138.8 ± 6.3)	

Run 58203, event 4980 (analysis II)		
Particle	E_T (GeV)	η
Muon	$83.0^{+41.8}_{-20.8}$	0.56
Jet1	111.9 ± 22.4	0.13
Jet2	36.2 ± 8.3	0.29
Jet3	33.8 ± 7.1	1.26
Jet4	18.4 ± 4.6	−0.70
Muon	$7.4^{+1.2}_{-0.9}$	0.22
$\not\!\!E_T$ ($\not\!\!E_T^{\rm cal}$)	$38.0^{+42.2}_{-21.0}$ (109.9 ± 5.7)	

The event observed in the $e\mu$ channel is exceptional in that its kinematic characteristics (see the Appendix) rule out the possibility of it being a $Z \to \tau\tau$, the largest physics background to this channel. The estimated background for this event is $0.16 \pm .060$.

In the absence of top quarks, we calculate the probability of an upward fluctuation of the total background to nine or more events to be 2.7%. Assuming the observed excess is due to $t\bar{t}$ production we can calculate a cross section. Because the acceptance varies with the top mass the calculated cross section is a function of the top mass. For a 180 GeV/c^2 (160 GeV/c^2) top mass hypothesis, the top production cross section is 8.2 ± 5.1 pb (9.2 ± 5.7 pb). This cross section is consistent with theoretical expectations for the standard model top quark [21] and the observation of top quark production from D0 [11] and CDF [12]. The excess of events over background observed in the 1992–1993 run is not sufficient to demonstrate the existence of the top quark.

ACKNOWLEDGMENTS

We thank the Fermilab Accelerator, Computing, and Research Divisions, and the support staffs at the collaborating institutions for their contributions to the success of this work. We also acknowledge the support of the U.S. Department of Energy, the U.S. National Science Foundation, the Commissariat à L'Energie Atomique in France, the Ministry for Atomic Energy and the Ministry of Science and Technology Policy in Russia, CNPq in Brazil, the Departments of Atomic Energy and Science and Education in India, Colciencias in Colombia, CONACyT in Mexico, the Ministry of Education, Research Foundation and KOSEF in Korea, and the A.P. Sloan Foundation.

APPENDIX: TOP CANDIDATE EVENTS

We list in Tables XXXIV–XXXIX parameters for the top quark candidate events. The parameters given for muons correspond to values obtained after refitting them to an improved version of the reconstruction program [51] with significantly better muon resolution (see Sec. IV B) than in the version of the reconstruction program used for the event selection.

[1] M. L. Perl *et al.*, Phys. Lett. **70B**, 487 (1977).
[2] S. W. Herb *et al.*, Phys. Rev. Lett. **39**, 252 (1977).
[3] S. L. Glashow, Nucl. Phys. **22**, 579 (1968); S. Weinberg, Phys. Rev. Lett. **19**, 1264 (1967); A. Salam, in *Elementary Particle Theory: Relativistic Groups and Analyticity (Nobel Symposium No. 8)*, edited by N. Svartholm (Almqvist and Wiksell, Sweden, 1968), p. 367.
[4] S. L. Glashow, J. Illiopoulos, and L. Maiani, Phys. Rev. D **2**, 1285, 1970; M. Kobayashi and M. Maskawa, Prog. Theor. Phys. **49**, 652 (1973).
[5] CLEO Collaboration, P. Avery *et al.*, Phys. Rev. Lett. **53**, 1309 (1994); CLEO Collaboration, A. Bean *et al.*, Phys. Rev. D **35**, 3533 (1987); ALEPH Collaboration, D. Decamp *et al.*, Phys. Lett. B **263**, 325 (1992); DELPHI Collaboration, P. Abreu *et al.*, *ibid.* **276**, 536 (1992); L3 Collaboration, O. Adriani *et al.*, *ibid.* **292**, 454 (1992).
[6] UA1 Collaboration, G. Arnison *et al.*, Phys. Lett. **147B**, 493 (1984); C. Albajar *et al.*, Z. Phys. C **48**, 1 (1990); UA2 Collaboration, T. Akesson *et al.*, *ibid.* **46**, 179 (1990).
[7] CDF Collaboration, F. Abe *et al.*, Phys. Rev. Lett. **68**, 447 (1992); Phys. Rev. D **45**, 3921 (1992).
[8] S. Abachi *et al.*, Phys. Rev. Lett. **72**, 2138 (1994).
[9] The integrated luminosity used in the present analysis is lower by 12% from Ref. [8] due to a change in the world average $\bar{p}p$ inelastic cross section as described in Fermilab Report No. FERMILAB-TM-1911, 1994 (unpublished).
[10] CDF Collaboration, F. Abe *et al.*, Phys. Rev. Lett. **73**, 225 (1994); Phys. Rev. D **50**, 2966 (1994).
[11] D0 Collaboration, S. Abachi *et al.*, Phys. Rev. Lett. **74**, 2632 (1995).
[12] CDF Collaboration, F. Abe *et al.*, Phys. Rev. Lett. **74**, 2626 (1995).
[13] W. Bardeen, C. Hill, and M. Lindner, Phys. Rev. D **41**, 1647 (1990).
[14] M. Carena, S. Pokorski, and C. E. M. Wagner, Nucl. Phys. **B406**, 59 (1993); V. Barger, M. S. Berger, and P. Ohmann, Phys. Rev. D **47**, 1093 (1993).
[15] CDF Collaboration, Y.-K. Kim, in '94 Electroweak Interactions and Unified Theories, Proceedings the XXIXth Rencontres de Moriond, Meribel les Allves, France, 1994, edited by J. Tran Tanh Van (Editions

Frontiéres, Gif-sur-Yvette, 1994).
[16] D0 Collaboration, C.-K. Jung, in *Proceedings of the 27th International Conference on High Energy Physics*, Glasgow, Scotland, 1994, edited by P. J. Bussey and I. G. Knowles (IOP, London, 1995).
[17] The LEP Collaborations ALEPH, DELPHI, L3, OPAL, and the LEP Electroweak Working Group, CERN Report No. CERN-PPE/94-187, 1994 (unpublished).
[18] SLD Collaboration, K. Abe *et al.*, Phys. Rev. Lett. **73**, 25 (1994).
[19] CDHS Collaboration, H. Abramowicz *et al.*, Phys. Rev. Lett. **57**, 298 (1986); CDHS Collaboration, A. Blondel *et al.*, Z. Phys. C **45**, 361 (1990); CCFR Collaboration, C. G. Arroyo, *et al.*, Phys. Rev. Lett. **72**, 3452 (1994); CHARM Collaboration, J. V. Allaby *et al.*, Phys. Lett. B **177**, 446 (1986); CHARM Collaboration, J. V. Allaby *et al.*, Z. Phys. C **36**, 611 (1987).
[20] P. Nason, S. Dawson, and R. K. Ellis, Nucl. Phys. **B303**, 607 (1988).
[21] E. Laenen, J. Smith, and W. van Neerven, Phys. Lett. B **321**, 254 (1994); Nucl. Phys. **B369**, 543 (1992).
[22] C.-P. Yuan, Phys. Rev. D **41**, 42 (1990); R. K. Ellis and S. Parke, *ibid.* **46**, 3785 (1994); D. O. Carlson and C.-P. Yuan, Phys. Lett. B **306**, 386 (1993); G. Bordes and B. van Eijk, Nucl. Phys. **B435**, 23 (1995).
[23] S. L. Glashow and E. E. Jenkins, Phys. Lett. B **196**, 233 (1987).
[24] D0 Collaboration, S. Abachi *et al.*, Nucl. Instrum. Methods A **338**, 185 (1994).
[25] A. Astbury *et al.*, UA1 Technical Proposal Report No. CERN/SPSC/78-06, 1978 (unpublished); C. Cochet *et al.*, Nucl. Instrum. Methods A **243**, 45 (1986); B. Aubert *et al.*, *ibid.* **176**, 195 (1980); M. J. Corden *et al.*, *ibid.* A **238** 273 (1985); M. Calvetti *et al.*, IEEE Trans. Nucl. Sci. **NS-30**, 71 (1983).
[26] F. Abe *et al.*, Nucl. Instrum. Methods A **271**, 387 (1988).
[27] D0 Collaboration, M. Narain, in *The Fermilab Meeting Proceedings of Meeting of the Division of Particles and Fields of the American Physical Society, Batavia, Illinois, 1992*, edited by C. Albright, P. Kasper, R. Raja, and J. Yoh (World Scientific, Singapore, 1993).
[28] R. Brun *et al.*, GEANT User's Guide v3.14, CERN Program Library (unpublished).
[29] D0 Collaboration, S. Abachi *et al.*, Phys Rev. Lett. **74**, 3548 (1995).
[30] UA1 Collaboration, G. Arnison *et al.*, Phys. Lett. **123B**, 115 (1983); **132B**, 21 (1983).
[31] CDF Collaboration, F. Abe *et al.*, Phys. Rev. Lett. **69**, 2898 (1992).
[32] D0 Collaboration, J. A. Guida, in Proceedings of the 4th International Conference on Advanced Technology and Particle Physics, Como, Italy, 1994 (unpublished); Fermilab Report No. FERMILAB-CONF-95/010-E, 1995 (unpublished); D0 Collaboration, J. Kotcher, Fermilab Report No. FERMILAB-CONF-95/007-E, 1995 (unpublished).
[33] F. Paige and S. Protopopescu, BNL Report No. BNL38034, 1986 (unpublished), release v6.49.
[34] G. Marchesini *et al.*, Comput. Phys. Commun. **67**, 465 (1992).
[35] A. J. Milder, Ph.D. thesis, University of Arizona, 1993.
[36] F. A. Berends, H. Kuijf, B. Tausk, and W. T. Giele, Nucl. Phys. **B357**, 32 (1991).
[37] H. U. Bengtsson and T. Sjostrand, Comput. Phys. Commun. **46**, 43 (1987).
[38] D0 Collaboration, J. Womersley, *Proceedings of the XXVI International Conference on High Energy Physics*, Dallas, Texas, 1992, edited by J. Sanford, AIP Conf. Proc. No. 272 (AIP, New York, 1993).
[39] J. Botts *et al.*, Phys. Lett. B **304**, 159 (1993).
[40] V. Balamurali, Ph.D. thesis, University of Notre Dame, Indiana, 1994 (unpublished).
[41] J. Cochran, Ph.D. thesis, State University of New York at Stony Brook, 1993 (unpublished).
[42] U. Baur and D. Zeppenfeld, Nucl. Phys. **B308**, 127 (1988); U. Baur and E. L. Berger, Phys. Rev. D **41**, 1476 (1990).
[43] V. Bhatnagar and J. B. Singh, D0 Internal Report No. 1858, 1993 (unpublished); D. Hedin, D0 Internal Report No. 1738, 1993 (unpublished).
[44] T. Huehn, Ph.D. thesis, University of California, Riverside (unpublished).
[45] R. Hall, Ph.D. thesis, University of California, Riverside, 1994 (unpublished).
[46] V. D. Barger and R. J. N. Phillips, *Collider Physics* (Addison-Wesley, Reading, MA, 1987), p. 281.
[47] S. Abachi *et al.*, Phys. Rev. Lett. **74**, 2422 (1995).
[48] D. Chakraborty, Ph.D. thesis, State University of New York at Stony Brook, 1994 (unpublished).
[49] J. Thompson, Ph.D. thesis, State University of New York at Stony Brook, 1994 (unpublished).
[50] H. Xu, Ph.D. thesis, Brown University, 1995 (unpublished).
[51] An improved algorithm which reduces the second term in the muon resolution to 0.003 was available for further analysis after the initial selection.